Momentum Near-wall Region Characterization in a Reciprocating Internal-combustion Engine

by

Mark L. Greene

A dissertation submitted in partial fulfillment
of the requirements for the degree of
Doctor of Philosophy
(Mechanical Engineering)
in the University of Michigan
2017

Doctoral Committee:

Professor Volker Sick, Chair
Professor Luis P. Bernal
Professor Andreas Dreizler, Technische Universität Darmstadt
Associate Professor Kevin Pipe
Research Scientist David L. Reuss

Acknowledgements

There are so many people who either contributed directly to the work presented in this dissertation, or furthered my academic development in my graduate career that it would be impossible to name them all individually.

First and foremost, I would like to thank my advisor Prof. Volker Sick for his continuous support, guidance, and encouragement as I struggled through unexpected and seemingly endless challenges in collecting the desired quality ultimately achieved in the experimental measurements disclosed herein. Dr. David Reuss, whose influential contribution to this work cannot possibly be overstated, receives my deepest gratitude for countless discussions and assistance that significantly shaped the outcome of this work. I would also like to thank the rest of my committee: Prof. Luis Bernal, Prof. Andreas Dreizler, and Prof. Kevin Pipe; whose diverse experience and points of view helped me narrow the focus of my work in the context of a deeper and broader understanding of how this work fits into the greater academic community.

This work would not have been possible without the support of my lab mates who patiently taught me to operate the engines systems and assisted me with my experiments. Special thanks and deepest appreciation goes to Mohammad Alzuabi whose time and physical contribution to this work enabled numerous repetitions of measurements that otherwise would not have been possible. I would also like to thank Dr. Peter Lillo and Dr. Philipp Schiffmann for their instrumental role in teaching me about engines and specifically the complex systems utilized in our laboratory.

Last but not least, I would like to acknowledge Dr. Douglas Neal of LaVision Inc. for his time and patience in assisting me with the implementation of the PIV uncertainty estimations presented throughout this work as I integrated these estimations into our laboratory procedures.

Table of Contents

List of Figures

List of Tables

List of Symbols

BDCi = bottom dead center intake piston position (180 CA)
C_1, C_2, C_3 = experimentally determined constants with values that may be unique in each occurrence
C_p = specific heat of fluid at constant pressure
d = cylinder bore
$\dot{q}$ = heat transfer rate
A = area
M = magnification factor
P = pressure
Pr = Prandtl number
R = gas constant
Re = Reynolds number based on mean piston speed
T = bulk gas temperature
T_l = local gas temperature
T_w = wall temperature
U = free stream velocity
U^+ = dimensionless Law of the Wall velocity
V = instantaneous cylinder volume
V_p = mean piston speed
h = heat transfer coefficient
p = gas pressure
r = compression ratio
s = entropy of fluid
TDCc = top dead center compression piston position (360 CA)
TDCe = top dead center exhaust piston position (0 CA)
u = instantaneous velocity
$\bar{u}$ = mean velocity
u' = turbulent fluctuation of velocity
u_τ = shear velocity
x = wall-parallel dimension
y = wall-normal dimension
Λ_x = integral length scale
δ = 99% momentum boundary layer thickness
δ_T = thermal boundary layer thickness
ρ = density
τ_w = shear stress at wall
ν = kinematic viscosity
ω = angular frequency of swirl
< >= ensemble average

Abstract

Accurately modeling the transfer of mass, momentum, and energy through engine near-wall regions is critical to achieving the long-standing goal of predictive engine simulations. This work presents the first planar near-wall velocimetry measurements to be recorded in a fired engine, the first near-wall velocimetry measurements to be recorded at the piston surface, the first planar near-wall velocimetry measurements to be recorded at multiple surfaces in the same engine, and expands the engine speed envelope of planar near-wall velocimetry measurements to higher engine speeds. These measurements were performed in an engine with well-characterized boundary conditions that serves as a reference and validation platform for researchers around the world. The velocimetry measurements were accompanied by head surface temperature and heat flux measurements. A unique particle image velocimetry (PIV) system was developed that both overcomes inherent experimental challenges in the engine used in this work, but also teaches general techniques broadly applicable to near-wall imaging in internal-combustion engines. The utility of an imaging system inclined towards the surface, specific selection of PIV processing parameters, and careful alignment of the vector grid to the surface are all shown to be important contributions to improve near-wall vector quality. High-resolution PIV measurements were taken in a 5- x 6 mm field of view at the head and piston surfaces. Measurements were recorded at engine speeds of 500- and 1300 rpm under both motored and fired conditions. High crank-angle resolution tests permit visualization of the variety of flow types imposed upon engine in-cylinder surfaces including wall-parallel flow, impinging jet-like flows, wall jet-like flows, and shear flows. The influence of the wall is observed to have an effect on the wall-normal velocity component farther from the wall than for the wall-parallel velocity component. Velocity magnitudes are found to be similar at the head and piston surfaces when the piston is stationary, but significant differences develop at high piston speed even after normalizing for the piston speed. The effects of inviscid compression are found to account for a significant portion of the observed wall-normal flow at the head and piston surfaces. These investigations are an essential effort towards the development of improved models for wall heat transfer in reciprocating internal-combustion engines.

Introduction

Since their first development internal-combustion engines have revolutionized power generation and use. Their utility from high energy density liquid fuels, and scalability, has led them to become one of the most prevalent machines in the world today. From sub-single horsepower model airplane engines to hundred-thousand horsepower ship engines, one simply could not imagine life today without the internal-combustion engine.

This easy access to mechanical power is not without consequences however, especially to our health and the environment. Incomplete combustion products such as carbon monoxide and nitrous oxides contribute to the formation of smog, and pose health risks. Furthermore the release of tremendous stores of the earth's carbon due to the mining and combustion of fossil fuels has affected the global climate in irreversible ways. For these reasons ongoing efforts continue to decrease cylinder-out emissions and improve fuel efficiency. Understanding in-cylinder heat transfer plays a critical role in overcoming both of these challenges.

In-cylinder heat transfer contributes significantly to controlling both emissions and efficiency. The peak cylinder pressure and temperature reached during combustion partially controls pollutant formation, and this in turn is affected by heat exchange between the cylinder walls and the combustible charge. Similarly, a large fraction of the fuel energy is lost as heat transferred to walls resulting in a decrease in engine efficiency.

Not surprisingly, significant effort has been placed towards understanding in-cylinder heat transfer over many decades (Taylor 1951, Overbye, Bennethum et al. 1961, Annand and Ma 1971, Alkidas 1980, Chen and Karim 1998, Chang, Guralp et al. 2004). While much has been learned over this time, a fundamental understanding of the physical processes involved and their interactions remains elusive. The slow progress in the field is largely due to a lack of diagnostic tools to adequately study the relevant physical processes on the time and length scales at which

they develop. As a result, in-cylinder heat transfer remains an active area of research and is the topic of the present work.

Recent developments of high-speed cameras and lasers now allow these physical processes to be investigated (Alharbi and Sick 2010, Jainski, Lu et al. 2013). The present work aims to utilize these technologies to characterize the in-cylinder flow near walls which are responsible for convective heat transfer to these surfaces. This document shall be organized in the following manner. In Chapter 1, a historical overview of previous work on engine heat transfer followed by an analysis of current gaps in understanding will be presented. In Chapter 2, a compilation of canonical boundary layer development and characteristics is presented, along with an analysis of how in-cylinder near wall regions differs. In Chapter 3 a thorough discussion of ongoing work will be had. Results from the experimental measurements are presented in Chapter 4. Lastly, in Chapter 5 discussions and remarks on a variety of remaining topics will be presented.

Chapter 1
A Review of Engine Heat Transfer Research

Ideally the design of all mechanical systems is based upon precise mathematical descriptions of the physics governing a machine's operation. This process allows for an optimal system to be designed without the need for expensive and time-consuming iterative prototyping and testing of design concepts. Such first-principle based design has been achievable for a wide range of components such as structural columns and beams, and electrical circuitry, for many years. For some more complicated systems the mathematical equations for the governing physics cannot be explicitly written down and solved directly to yield the optimal design. Yet for many of these, modern digital computers can be utilized to accurately simulate the behavior of systems and components from first-principle equations, thereby facilitating a virtual prototyping and design process that still avoids the extremely expensive and slow iterative physical prototyping and testing process. An excellent example for this latter application using mathematical direct-simulation is the design of geometrically complex structural components from linearly-elastic materials through the use of finite element analysis. However despite the vast array of systems that can currently be designed from first principles, some remain where this is still not possible.

Despite decades of research and countless careers spent on the topic, the understanding of the physics that govern operation of internal combustion engines still falls well short of that required to design these complex devices from first-principles. From the chemistry of millions of reactions of thousands of species to the complex heat transfer characteristics through unique unsteady near wall regions, elucidating the physics which governs engine operation is certainly formidable. Indeed, the understanding of engine operation from first-principles has been a sort of 'holy grail' for the engineering community for many decades, with the desire to attain such knowledge perhaps first stated by G. Eichelberg over 75 years ago. Yet as he so eloquently stated engineers cannot wait for this physics to be fully understood before further improving upon the design of the internal combustion engine (Eichelberg 1939). Indeed at that time researchers made

use of the limited diagnostic technology available to learn what they could to solve the most pragmatic aspects of engine design.

In the earliest days of engine research the only diagnostic available to researchers were so called “indicator diagrams” that plotted engine P-v diagrams mechanically. Analysis of the indicator diagram can be used to calculate the heat loss from the cylinder based upon assumed wall temperature and mean bulk temperature estimated from polytropic compression calculations (Janeway 1929, Janeway 1938). Similar detailed analyses of indicator diagrams yielded heat loss to cooling jacket and other quantities of practical interest, and noted need for higher speed diagnostics (Lanchester 1939).

Meanwhile other experimentalists incorporated thermocouples into their engine designs in order to directly measure wall temperatures both inside the cylinder and in the cooling channels in order to calculate the heat flux out of the cylinder. Due to the size of early thermocouples it was necessary to install them below the surface to be measured. Temperature measurements were taken on the cylinder head walls and piston top, and used to calculate periodical heat flux by the correlation

$$\frac{\dot{q}}{A} = 8.06\times10^{-5} V_p^{\frac{1}{3}} (pT)^{\frac{1}{2}} (T - T_w) \qquad 1\text{-}1$$

(Eichelberg 1939). Due to its simplicity the Eichelberg equation was used for several decades for practical modeling of heat transfer in engines (Whitehouse, Stotter et al. 1962, Annand 1963). When higher speed diagnostics became available it became clear that Eichelberg’s equation did not adequately reflect the increased heat transfer due to higher in-cylinder gas velocities. A colleague accordingly proposed revisions to increase the sensitivity of the speed dependent term and also account for changes in intake manifold air pressure. This revised Pflaum equation takes the form (Eichelberg and Pflaum 1951, Pflaum 1961)(as in (Annand 1963))

$$\frac{\dot{q}}{A(T-T_w)} = C_1 C_2 \left(3 \pm 2.57\left[1 - e^{\pm\left(1.50 - 0.127 V_p\right)}\right]\right)(pT)^{\frac{1}{2}} \qquad 1\text{-}2$$

Several years later the advantage of presenting correlations in terms of dimensionless groups became apparent for scaling of engine geometry. (Elser 1954) used thermocouples under

surfaces in two and four stroke diesel engines to develop his non-dimensional correlation. This correlation

$$Nu = 6.5\left(1 + 0.5\frac{\Delta s}{C_p}\right)[RePr]^{1/2}\,, \qquad 1\text{-}3$$

where Δs is the increase in entropy of the charge per unit mass from the start of compression, agrees well for his two stroke data but not his four stroke data (as in (Annand 1963)).

Other attempts to measure heat transfer focused on total heat rejected from the engine as measured by the cooling water. These studies which presented the results in terms of dimensional quantities were reviewed by (Taylor 1951). A later study combined the use of gas- and water-side thermocouples with total heat rejection measurements to obtain improved correlations of dimensionless values for the purpose of estimating engine cooling needs with greater accuracy (Taylor and Toong 1957). The thermocouples in this experiment were slightly above the head surface. While this study yielded more accurate predictions of time-averaged heat transfer and cooling requirements than previous correlations, it still only achieved an accuracy of ±20 percent.

Although previous attempts to model engine heat transfer to this point implicitly (Janeway 1938, Eichelberg 1939, Lanchester 1939, Taylor and Toong 1957) included the effects of in-cylinder radiation in their global analyses, it was not until the work of Chirkov that a radiative heat transfer term was included in engine heat transfer models based on black body radiative concepts ((Chirkov and Stefanovski 1958) as in (Annand 1963)).

By 1960 experimentalists finally were able to place surface thermocouples at the actual surface to be measured. Oguri conducted experiments similar to Eichelberg's but in a four-stroke SI engine (Eichelberg 1939, Oguri 1960). His instantaneous correlation coefficients matched the latter's coefficients quite well in the expansion stroke despite their calculation from a two-stroke diesel engine. Oguri used his data to present an improvement on Elser's dimensionless equation (Elser 1954) to obtain

$$Nu = 1.75\left(1 + \frac{\Delta s}{C_p}\right)[RePr]^{\frac{1}{2}}[2 + \cos(\theta - 20°)] \qquad 1\text{-}4$$

where θ is crank angle degrees from top dead center (as in (Annand 1963)). The following year Overbye et al. published a second paper using true surface thermocouples but did not calculate instantaneous coefficients due to the phase lag between gas temperature and heat flux measurements despite obtaining cycle-resolved measurements ((Overbye, Bennethum et al. 1961) as in (Annand 1963)).

$$\frac{\dot{q}L}{3600Ak_iT_i} = \left(\frac{LV_p\rho_iC_{pi}}{k_i}\right)\left(\frac{0.26p}{rp_i} - 0.035\right)\times 10^{-4} + 0.1\frac{p}{rp_i} - 0.02 \qquad 1\text{-}5$$

Where gas properties with subscript *i* are evaluated at intake manifold conditions. Their notable contribution is conducting the first data analysis on a digital computer.

Overbye et al. were not the only engineers to turn to computers as they became available. By the 1960s engine designers were making use of the physical knowledge learned from these early experiments by incorporating calculations based on these insights into their design process. But these computations were involved and quite time consuming. Hand computations to design valve timing and gas exchange during the exhaust and intake stroke of a diesel engine could take three months. When digital computers became commercially available they were quickly applied to these calculations, thereby reducing the computation time to less than a day. These first simulations used tabulated heat transfer coefficients versus crank angle (Williams 1960). Early attempts at engine simulations were improved upon, calculating some aspects of entire engine cycles including some fluid dynamics phenomenon such as scavenging efficiency (Whitehouse, Stotter et al. 1962). A single spatial-averaged surface temperature was calculated before starting the simulation and used to calculate the heat transfer during the closed part of the cycle with the Eichelberg correlation. No heat transfer was calculated during scavenging.

In the United States a more detailed simulation of a diesel engine was conducted by (McAulay, Wu et al. 1965). This attempt still used the Eichelberg formula but simulated the in-cylinder surface temperature in five zones and computed heat transfer during the entire cycle. Their combustion model also accounts for dissociation effects which they claim to improve the results of their calculated volumetric efficiency.

Given the shortcomings of previous heat transfer models for test conditions beyond which they were calibrated, Annand derived a new dimensionless correlation incorporating distinct

convective and radiative terms most similar to that presented by Chirkov and Stefanovski of those before him. Annand distinguishes his equation due to its correct dimensionality and physical derivation

$$\frac{\dot{q}}{A} = C_1 \frac{k}{D} Re^{0.7}(T - T_w) + C_2(T^4 - T_w^4) \quad 1\text{-}6$$

(Annand 1963). He validates his work through comparison to previous cycle-resolved experiments (Elser 1954, Overbye, Bennethum et al. 1961) and time averaged experiments including (Ku 1940, Zipkin and Sanders 1945). His model requires a different constant C_1 for engines with differing flow intensities with a value for C_2 that depends on cycle phase and ignition type.

In 1967 the most prevalent and enduring in-cylinder heat transfer model was published by Woschni

$$h = 110 d^{-0.2} p^{0.8} T_l^{-0.53} \left[C_1 V_p + C_2 \frac{V T_r}{P_r V_r} (p - p_0) \right]^{0.8} \quad 1\text{-}7$$

where p_0 is the corresponding pressure in cylinder under motored operation, and the subscript r on gas properties denotes evaluation at a reference condition (Woschni 1967, Heywood 1988). The Woschni model clearly shows for the first time independent terms for the heat transfer due to piston motion and that due to forced convection (Woschni 1967). Three years later the author presented a modification of his equation to better include the effect of swirl in high swirl engines by changing the constants C_1 and C_2 to become functions of the piston and swirl velocities (Woschni 1970, Heywood 1988). Decades later a second modification that mainly replaced the characteristic length with the instantaneous cylinder volume instead of the bore was introduced with only modest acceptance ((Hohenberg 1979) as in (Torregrosa, Olmeda et al. 2008)). These equations' simplicity, relative accuracy, and universal form across engine architectures caused its widespread application for many decades. Indeed, the Woschni model and slightly modified forms are still the dominant spatial-averaged in-cylinder heat transfer correlations in use today (Torregrosa, Olmeda et al. 2008, Gamma Technologies 2013).

Prior in-cylinder temperature measurements to this point had used bulky nickel-iron thermocouples set in an iron plug and fitted into a hole drilled into the head surface. In 1971 Annand and Ma developed a technique to install thin-film surface thermocouples on any location

on the head using vacuum deposition (Annand and Ma 1971). From their study of calculated heat flux between these new surface thermocouples and traditional thermocouples installed on the coolant side of the head in their diesel engine they developed the correlation

$$\dot{q} = \frac{k}{D} Re^{0.7} \left[C_1 (T - T_w) + \frac{C_2}{\omega} \frac{dT}{dt} \right] + C_3 \sigma (T^4 - T_w^4) \qquad 1\text{-}8$$

which is the same as that proposed by Annand in 1963 (Equation 1-6) but with the addition of the time derivative term to compensate for the unsteady nature of in-cylinder heat transfer (Annand 1963). Despite acknowledging the spatial variation of heat transfer in the cylinder they present the model as a spatial average correlation. The three constants vary with operating condition so they present the average values in their final model. While their work advanced the technology of surface thermocouples, the proposed model required experimentally determined engine-specific constants that contributed to its poor acceptance. Experimental work to broaden heat transfer and temperature data available for model development and validation has continued since and includes the work of (Whitehouse 1970, Annand and Ma 1971, Alkidas 1980, Chen and Karim 1998, Chang, Guralp et al. 2004)

The 1970 paper by LeFeuvre et al. shows a marked shift in the analysis of in-cylinder heat transfer as it introduces the concept of "boundary layer models" rather than the broader consideration of heat transfer models discussed by others previously (LeFeuvre, Myers et al. 1970). Noting that none of the existing correlations adequately predict the surface temperature and heat flux variation measured in their diesel engine, they present a new model for motored conditions of the form

$$\dot{q} = C_1 \frac{k}{r} Re_\omega^{0.8} Pr^{0.33} (T - T_w) \qquad 1\text{-}9$$

where Re_ω is the Reynolds number based on in-cylinder swirl and radius. Despite presenting yet another spatially averaged heat transfer correlation these authors state the importance of velocity and temperature measurements within the boundary layer in order to develop physics-based boundary layer models in engines. The introduction of these boundary layer concepts represents a paradigm shift in the analysis of in-cylinder heat transfer that has guided the engine community ever since.

The effect of LeFeuvre et al.'s contribution can possibly be seen in the fundamental work conducted by (Grief, Namba et al. 1979). These researchers solved the continuity and energy equations for the isentropic compression of a gas and verified their calculations with a rapid compression machine. In their derivation they assumed spatially uniform pressure and negligible viscous dissipation. Their work is a good example of early attempts to understand the physical processes governing heat transfer in engines.

Furthering the development of heat transfer models based upon physically significant quantities, (Borgnakke, Arpaci et al. 1980) presented a model similar to those of Annand and Woschni (Annand 1963, Woschni 1967). Noting that the latter models were based on only marginally relevant quantities of mean piston speed and the bore diameter they instead chose to evaluate the Reynolds number using square root of the bulk gas turbulent kinetic energy as the characteristic velocity scale and the bulk gas turbulent integral length as the characteristic length scale. While these quantities of course could not be determined experimentally they did find their model

$$\dot{q} = k_{laminar} \frac{\Delta T}{l_\infty} \left(\frac{K_\infty^{\frac{1}{2}} l_\infty}{\nu} \right)^{\frac{2}{3}} f(\frac{\delta}{l_\infty}) \qquad 1\text{-}10$$

more accurately matched experimental data.

This group later introduced another model that was the first model to not be of the form the $Nu \sim Re^n$ which they showed offered improved accuracy over the correlations of (Woschni 1970, Annand and Ma 1971, Poulos and Heywood 1983) when compared against the experimental data of Alkidas et al (Alkidas, Puzinauskas et al. 1990, Torregrosa, Olmeda et al. 2008)

$$\frac{d\delta_T}{dt} = \frac{2\delta_T}{\rho_\delta - \rho_w} \left[\frac{d\rho_m}{dt} + \frac{(R - C_p)}{RC_pT_\delta} \frac{dP}{dt} + \frac{q_w}{C_pT_\delta} - \frac{1}{2C_pT_\delta} (C_1 \omega \Lambda_x \bar{\rho} \bar{C}_p \right] \qquad 1\text{-}11$$

where on gas properties the subscripts *w*, δ, and *m*, indicate evaluation at the wall, thermal boundary layer thickness, and mixing length, and over bars the mean values (Puzinauskas and Borgnakke 1991).

A review article covering past and present experimental and modeling techniques for in-cylinder heat transfer emphasized the spatial inhomogeneity of surface temperature and heat flux (Borman and Nishiwaki 1987). It echoes sentiment of (LeFeuvre, Myers et al. 1970) by emphasizing the significant need for the measurement of velocity, temperature, and turbulence profiles in engines in order to gain further understanding of the gas-side physics. Fortunately several diagnostic techniques had developed sufficiently by this point to begin to fill this void of knowledge.

Hot-wire anemometry uses the change in electrical resistance of a heated wire due to convective cooling to measure the gas velocity. It is one of the earliest developed techniques, yet due to its simplicity, reliability, and economical price continues to be the most commonly used gas velocimetry techniques used today (Bernard and Wallace 2002). Unfortunately the physical constraints in access to the in-cylinder flow and inability to readily move the measurement location, compounded by the intrusiveness of the technique, makes hot-wire anemometry have only limited application in engines. Despite these shortcomings, hot-wire anemometry was applied to in-cylinder flows when no other techniques were available (Lancaster 1976, Witze 1977).

However fairly quickly laser technology advanced sufficiently to allow the development of a less-intrusive technique based upon the Doppler frequency shift of light reflected from a moving particle. Laser Doppler Anemometry, also called Laser Doppler Velocimetry, requires seeding the flow with particles small enough to faithfully follow the flow structures. While nominally this technique only measures the velocity in a single direction, systems can be combined in orthogonal directions to simultaneously measure multiple components of the particle velocity at a single point, provided sufficient optical access exists (Bernard and Wallace 2002). Again, due to the limited optical access inherent in engine research most experiments measured only one velocity components (Asanuma and Obokata 1979, Rask 1979, Cole and Swords 1980, Liou, Hall et al. 1984) or at most two (Rask 1979, Fansler 1985). One of the main concerns with using LDV during combustion was the effect of index of refraction gradients on signal quality and interpretation of measured values. Fortunately this concern was laid to rest by (Witze and Baritaud 1985) who showed that combustion only decreased signal quality. While the above LDV experiments represented the first application of laser diagnostics to velocimetry of engine flows,

they contributed only to our understanding of the bulk flow and did not contribute to flow development in the boundary layers where heat transfer occurs.

The first velocity measurements recorded in the boundary layer of an engine were conducted by (Hall and Bracco 1986) using LDV at the cylinder wall. They successfully resolved the radial component of the velocity profile as close as 1.5 mm from the wall and the tangential velocity as close as 0.5 mm from the wall. Their closest measurement to the wall yielded a velocity 90 percent of the free stream, indicating a very thin boundary layer in an engine operating at 1200 rpm. Despite only measuring two velocity components 1.5 mm from the wall they claim the turbulence to be within 20 percent of being isotropic. They noted that turbulence intensity increased sharply near the wall which they attributed to wall generated turbulence. This last observation would later be contradicted at certain conditions by other researchers (Foster and Witze 1987).

Hall and Bracco's measurements were limited in distance to the wall due to constraints in optical access. Other researchers employed a specially designed engine with a toroidal shaped head in order to measure velocities with LDV down to 60 μm from the wall (Foster and Witze 1987). They tested low and high swirl cases, both motored and fired, at 300 rpm. For the low swirl motored case they recorded a laminar-like profile of thickness 700-1000 μm with turbulence intensity decreasing when approaching the wall. For the high swirl motored case a thickness of less than 200 μm was found with the turbulence intensity increasing as the wall was approached. In both cases the boundary layer thickness increased under firing conditions due to the increased viscosity from the elevated gas temperature. In all test conditions precession of the swirl center caused changes in the free stream velocity and subsequent variation of boundary layer thickness. These experiments' identification of both laminar and turbulent boundary layers in the same engine but under different conditions highlighted the continued need to understand in-cylinder flow physics in order to accurately predict engine heat transfer.

Another application of LDV to engine boundary layers was that of (Pierce, Ghandhi et al. 1992). Here they recorded measurements to within 50 μm of a surface protruding from the head. They used the protruding surface to mimic the geometry of a heat transfer probe previously installed in the engine and to avoid a previously unpresented problem with applying LDV near

surfaces. In their experiments they determined that for measurements taken closer than 0.5 mm from the wall, index of refraction gradients shifted the probe volume closer to the surface when imaging a flat surface. This effect would introduce unknown errors in determining the measurement location, and brings into question the accuracy of previous LDV measurements near flat surfaces. It is possible however that Foster and Witze inadvertently avoided this issue due to the convex toroidal surface at which they were measuring.

In addition to their LDV measurements Pierce et al. recorded the first near wall particle image velocimetry (PIV) measurements, building on the accomplishments of (Reuss, Adrian et al. 1989) who first successfully applied the technique to the engine environment. An introduction to PIV is presented in section 3.1. Their measurements indicated that in typical four-stroke engine geometries only a very thin low momentum region exists and its profile does not present as a traditional boundary layer which directly contradicts the findings of (Foster and Witze 1987) who collected data at a substantially slower engine speed. Pierce et al.'s conclusion has since been supported by other experiments (Alharbi and Sick 2010, Jainski, Lu et al. 2013). Pierce et al. attributes the lack of conventional boundary layers in engines to fluid rotation, wall normal flow, and transient nature of near wall forcing functions. Their results also indicate dependence in the near wall flow on intake and combustion chamber geometry, and operating conditions.

The experiments of (Hall and Bracco 1986, Foster and Witze 1987, Pierce, Ghandhi et al. 1992) represent the first velocity boundary layer measurements in engines. Unfortunately the utility of LDV experiments, which inherently lack instantaneous spatial information as they only measure velocity at a single point, is quite limited in its ability to garner physical insights into the boundary layer processes that drive in-cylinder heat transfer. Likewise, the PIV systems used in these experiments were limited to generating one velocity field per cycle which is only of limited value as the near wall flow features throughout the cycle are highly dependent on intake flow structures and their development. For these reasons momentum boundary layer investigations in engines ceased for nearly two decades. During that time digital CCD and later high-speed CMOS camera technology rapidly developed to the point that they offered the opportunity to investigate engine boundary layers at the spatial and temporal resolution necessary to resolve the underlying physics.

While the momentum boundary layer in engines is important to heat transfer, the thermal boundary layer is as well. The first paper to investigate this topic applied Schlieren imaging to measure the thermal boundary layer thickness at various points in the cycle (Lyford-Pike and Heywood 1984). In their square piston engine they found the thermal boundary layer thickness to grow to a maximum at the end of the expansion stroke of 2 mm on the cylinder walls, with the thickness being 2-3 times greater on the head and piston top. In addition they verified that increased engine speeds decreased the thermal thickness and that the thickness was independent of load. They also presented the first correlation for thermal thickness of

$$\frac{\delta_T}{\sqrt{\alpha t}} = 0.6Re^{0.2} \tag{1-12}$$

where *Re* here is defined by the distance x_0 from the cylinder head and the free stream velocity *v*,

$$v = V_p \frac{x_o}{x} \tag{1-13}$$

and *x* is the distance from the piston to the head. As Schlieren imaging is based upon the index of refraction gradients due to variations in density and cannot provide quantitative temperature measurements, no further work was pursued utilizing this technique to resolve thermal boundary layers in engines.

The next notable experimental work on in-cylinder thermal boundary layers was conducted using Coherent Anti-Stokes Raman Scattering (CARS) thermometry (Lucht and Maris 1987). They successfully resolved the temperature profile at the head at three crank angles during the expansion stroke at a varying spatial resolution of 25-50 μm with the first measurement location 25 μm from the wall. They noted a distinct thickening during the expansion stroke and correlated their profiles with a power law. Later they combined their experiments with simultaneous heat flux measurements and recorded core gas temperatures during combustion (Lucht, Dunn-Rankin et al. 1991). They found the temperature profile to match that for flat plates. CARS requires aligning three laser beams to simultaneously cross at the measurement location, and like LDV measures at only a single point at a time and is therefore unable to resolve the instantaneous thermal boundary layer profile. For these reasons no further investigations using CARS thermometry in engines have been conducted.

The following year Chen and Veshagh built a quasi-steady boundary layer model that captures spatial and temporal changes in heat flux ((Chen and Veshagh 1992) as in (Torregrosa, Olmeda et al. 2008)). The model assumed a constant boundary layer profile following the power law and made use of the Colburn analogy that heat transfer depends only on the thermal boundary layer and free stream velocity.

A computational investigation developed a temperature wall function that accounted for the increase in turbulent Prandtl number in the boundary layer and variations in gas density (Han and Reitz 1997). The results of their simulations showed gas compressibility effects significantly affected heat transfer, yet the spatial incompressibility assumption is still often made. Furthermore, the effects of unsteadiness and heat release due to combustion were insignificant. Using their boundary layer model developed from the one-dimensional energy equation they found heat flux to be proportional to the difference of logarithms of the gas and wall temperatures rather than the arithmetical difference.

Despite these findings (Franco and Martorano 1998) determined that heat transfer was out of phase with the gas and wall temperature difference. Their multi-dimensional simulations were conducted in Fluent and investigated heat transfer in small two-stroke engines. They also identified the contribution of near wall vortices to increased heat transfer.

Yet another heat transfer model was developed by (Suzuki, Oguri et al. 2000) that includes the effects of molecular transport and turbulence processes to calculate mean heat transfer from cylinder pressure. They found that the turbulence intensity during the intake stroke can be determined by the mean gas density and mean piston speed during the intake stroke, and that the turbulence generated by combustion can be determined as a function of gas density and flame propagation speed. Their model yielded results similar to the Woschni equation (Torregrosa, Olmeda et al. 2008).

A coupled combustion-boundary layer model of an HCCI engine was published by (Fiveland and Assanis 2001). Their boundary layer model was based on that proposed by (Borgnakke, Arpaci et al. 1980, Puzinauskas and Borgnakke 1991) and allowed for the calculation of thermal boundary layer thickness, average heat transfer coefficient, and mass fraction trapped in boundary layer. Their computed boundary layer thickness varied from 0.2 mm near mid

compression to almost 3 mm at TDC. Other important observations include that 30-35% of the cylinder mass was contained in the boundary layer at the time of ignition.

(Chang, Guralp et al. 2004) measured surface temperature and heat flux at seven locations on piston top and cylinder head surface of an HCCI engine. Their results showed small spatial variation in direct contrast to the findings in diesel engines of (LeFeuvre, Myers et al. 1970, Annand and Ma 1971) and the SI engine of (Alkidas 1980). They presented a modified Woschni model with an improved flame propagation term.

An excellent review article of progress in engine modeling since (Borman and Nishiwaki 1987) can be found in (Torregrosa, Olmeda et al. 2008) which discusses much of the work mentioned previously but also presents progress in diesel engine heat transfer which has not been discussed here.

In 2008 (Cho, Assanis et al. 2008) published an experimental investigation comparing heat transfer between homogenous and stratified operation in an SIDI engine. They found much larger spatial variations of heat flux in the stratified mode and could detect the effects of spray impingement in cooling the piston during late injection at high loads. In their experiments the stratified mode produced 30 percent less average heat transfer than the homogenous mode. They compared their results with the Woschni and Hohenberg models with the conclusion that the Woschni model better predicted the heat transfer of the homogenous mode while the Hohenberg model better predicted the heat transfer of the stratified mode.

A comparison study of the Woschni model (Woschni 1967), the Hohenberg model (Hohenberg 1979), and the Assanis model (Chang, Guralp et al. 2004), for heat transfer in HCCI applications was conducted by (Soyhan, Yasar et al. 2009). They compared these models to measurements conducted in a Ricardo HCCI engine and simulations obtained using TRICE. They found that the combustion compression velocity term in the Woschni model was not relevant in HCCI applications and caused unrealistically high gas velocities and over predictions of heat transfer rates. The Assanis model underestimated heat transfer thereby over predicting peak pressures. They found that the Hohenberg model matched their measurements and simulations the best as it lacked a compression velocity term.

The following year (Rakopoulos, Kosmadakis et al. 2010) published another comparative study of existing heat transfer models. This time they compared the models of Launder and Spalding (Launder and Spalding 1974), Huh et al. (Huh, Chang et al. 1990), Angelberger (Angelberger, Poinsot et al. 1997), and Han and Reitz (Han and Reitz 1997). They compared these as well as their proposed model to the published data from the spark ignition engines of (Alkidas 1980, Yang, Pierce et al. 1988, Nijeweme, Kok et al. 2001), from the diesel engines of (Lawton 1987), and the motored engine of (Dao, Uyehara et al. 1973). Their results showed some improvement but the main contribution of their model is its applicability to both diesel and SI engine operation.

As digital PIV systems capable of crank-angle resolved measurements became available, interest returned to investigating the in-cylinder velocity boundary layer. (Alharbi and Sick 2009, Alharbi and Sick 2010) were the first to apply a digital PIV system to specifically study the near-wall processes. They used a telemicroscope to image a 1.69- x 2.25 mm field of view below a boss on the cylinder head surface in the tumble plane of a four-valve pent-roof optical engine. They recorded measurements for 98 consecutive cycles from 180-490 CA with the engine motored at 800 rpm. The high resolution measurements with a nearest-vector wall distance of 45 µm allowed identification and tracking of sub-millimeter-sized vortical structures as they moved within the boundary layer. Their results showed poor agreement with both Blasius' laminar boundary layer profile solution as well as the turbulent $1/7^{th}$ power law.

Later (Jainski, Lu et al. 2013) built upon the work of (Alharbi and Sick 2010) by expanding the latter's experiments to 400-, and 1100 rpm in the same engine. (Jainski, Lu et al. 2013) recorded their velocity measurements in a 2- x 2.25 mm field of view every 1-3 CAs, dependent engine speed, from 180- to 420 CA. The results of these experiments showed poor agreement with the logarithmic law-of-the-wall model to be introduced in Section 2.2 and were unable to resolve the viscous sublayer at 1100 rpm.

Recent direct numerical simulations of a rapid compression/expansion machine have shed light on some of the most interesting aspects of in-cylinder heat transfer to date (Schmitt, Frouzakis et al. 2015, Schmitt, Frouzakis et al. 2015, Schmitt, Frouzakis et al. 2016). Schmitt et al. simulated eight consecutive cycles of a compression/expansion machine using Direct Numerical Simulation.

With fully resolved mass, momentum, and energy distributions finally obtained for an engine-like geometry the authors were able to draw some very interesting inferences. Of most relevance to the present discussion, Schmitt et al. showed the significant discrepancy between contributions between the wall-parallel and wall-normal velocity components on wall heat flux at the cylinder head. The reproduced figure shown in Fig. 1-1 presents the three velocity components on a horizontal slice 0.375 mm below the head surface along with the calculated wall heat flux at the head. As can be seen the size-scale and structure of the velocity fluctuations in the wall-parallel directions of Fig. 1-1(a) and Fig. 1-1(b) poorly match the size-scale and structure of the heat flux calculated at the cylinder head in Fig. 1-1(d). Conversely, the size-scale and structure of the wall-normal velocity component presented in Fig. 1-1(c) matches the same characteristics of the heat flux remarkably well. The correlation of the wall-normal velocity and heat flux distribution continues to be one of the most important conclusions drawn from their work.

Figure 1-2 is a reproduction of another figure from the work of (Schmitt, Frouzakis et al. 2016). Here joint probability density functions (PDFs) have been computed between the wall heat flux at the cylinder head and the fluid temperature on a horizontal slice near the wall, and between the heat flux and the wall-normal velocity on the same cutting plane. All three quantities have been normalized by the planar average on the cutting plane and the joint PDFs are shown for four wall-normal distances from the wall. The important aspect to notice in these joint PDFs is the gradient of the density functions which indicates the correlation between the variables, as shown by the red dashed lines in Fig. 1-2(b). A strong correlation would appear as a 45° line as present in the lines marked A1-A4. A perfect decorrelation would be indicated by either a horizontal line or vertical line as shown by the red dashed line marked B4. As can be seen in Fig. 1-2(a) the correlation between the heat flux and fluid temperature decorrelate (more vertical) rapidly as the cutting plane is removed from the wall, to the point that by 3.75 mm from the wall little correlation exists between these quantities. However, in Fig. 1-2(b) it can be seen that the correlation between the heat flux and wall-normal velocity component remains as out towards nearly 4 mm from the wall, as indicated by the roughly constant gradients marked by dashed lines A1-A4. Note this correlation exists however only for wall-normal flow away from the wall ($-v_z$), which "results in locally lower and more uniform heat fluxes" (pg. 730). The "significantly higher and strongly fluctuating heat fluxes" (pg. 730) associated with wall-normal flow towards the wall decorrelate from the flow as the cutting plane is removed from the wall.

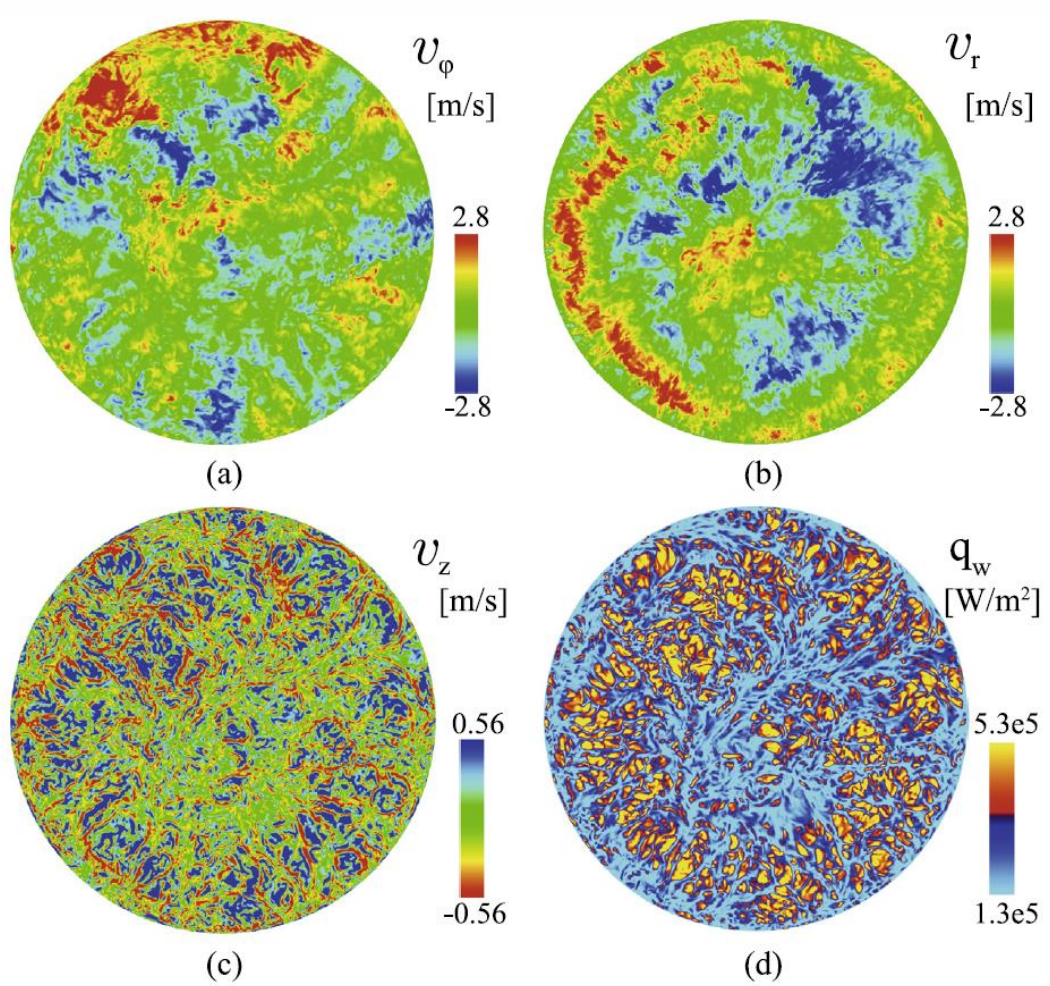

Figure 1-1 Velocity components in the (a) azimuthal, (b) radial and (c) axial direction at a horizontal slice at z = -0.375 mm and 346 CA; (d) heat flux distribution on the cylinder head at 346 CA. Reproduction of Figure 3 (Schmitt, Frouzakis et al. 2016).

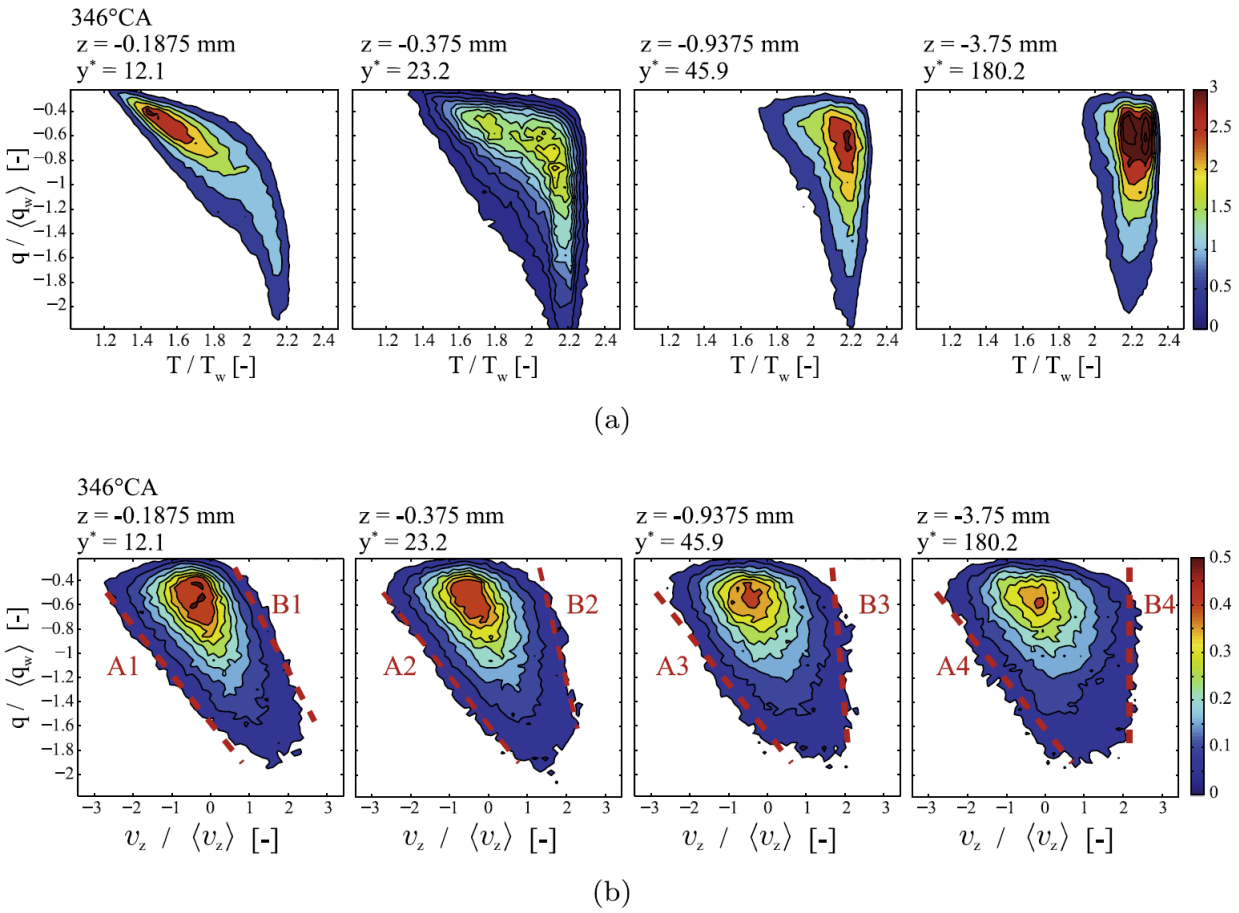

Figure 1-2 (a) Joint PDFs of temperature vs. heat flux and (b) joint PDF of the wall-normal velocity vs. the heat flux at 346 CA and four different distances from the cylinder head. Reproduction of Figure 12 (Schmitt, Frouzakis et al. 2016).

The above has been a thorough yet not exhaustive discourse on the historical development and progress in engine heat transfer measurements and computations. The interested reader can find more details and a broader discussion of published research in the three main review articles written over the last decades, namely (Annand 1963, Borman and Nishiwaki 1987, Torregrosa, Olmeda et al. 2008). Yet due to the vast amount of work on this topic not even these review articles include the entirety of completed work on engine heat transfer. What might be gleaned from this summary however is how little work has been done to explore the physical processes of the fluid mechanics that drive heat transfer in engines. The rest of this document will deal exclusively with this matter.

Chapter 2
Boundary Layer Theory

As seen in Chapter 1 research in engine in-cylinder heat transfer has gradually developed from global heat rejection studies to detailed microscopic measurements of the boundary layer in the in-cylinder near wall region. The increased scrutiny at the wall is due to the fact that all heat transferred from a fluid to a wall, or *vice versa*, must pass through the boundary layer. For this reason the characteristics of canonical boundary layers ought to be understood. The most studied, and best understood, boundary layer forms are those of steady laminar and turbulent flow over a flat plate. Therefore they warrant some discussion.

2.1 The Steady Laminar Boundary Layer

Steady laminar flow is characterized by a predictable flow field that contains only nonintersecting streaklines. Laminar flow can be observed in low Reynolds number situations often found in pipes and on the leading surfaces of bodies such as airfoils, automobiles, and sports balls. In many instances these surfaces can be considered approximately flat when a small enough region is considered. Therefore laminar flow over a flat plate is of extreme importance for many of these problems.

The direct solution to the continuity and Navier-Stokes momentum equations for 2D incompressible laminar flow on a flat plate was first obtained by (Blasius 1908), where the 99% boundary layer thickness δ at location x can be determined by

$$\delta = 5.0\frac{x}{\sqrt{Re_x}} \qquad 2\text{-}1$$

from which other properties may be calculated, such as the momentum thickness and drag coefficients (White 2006). For flows where the incompressibility assumption holds, the energy equation is decoupled from the velocity equations. Therefore the velocity can be calculated first and the energy equation solved subsequently to determine the heat transfer.

Figure 2-1 shows the development of the momentum and thermal boundary layers for laminar flat plate flow. The free stream enters the near wall region at velocity U and temperature T. From the leading edge of the plate the boundary layer starts developing in a consistent profile $u(y)$ with increasing penetration depth with distance from the leading edge. In this example, at a distance x_0, the plate is heated to a temperature of T_w causing heat transfer to the fluid at rate $\dot{q}$ and a temperature distribution $T_1(y)$.

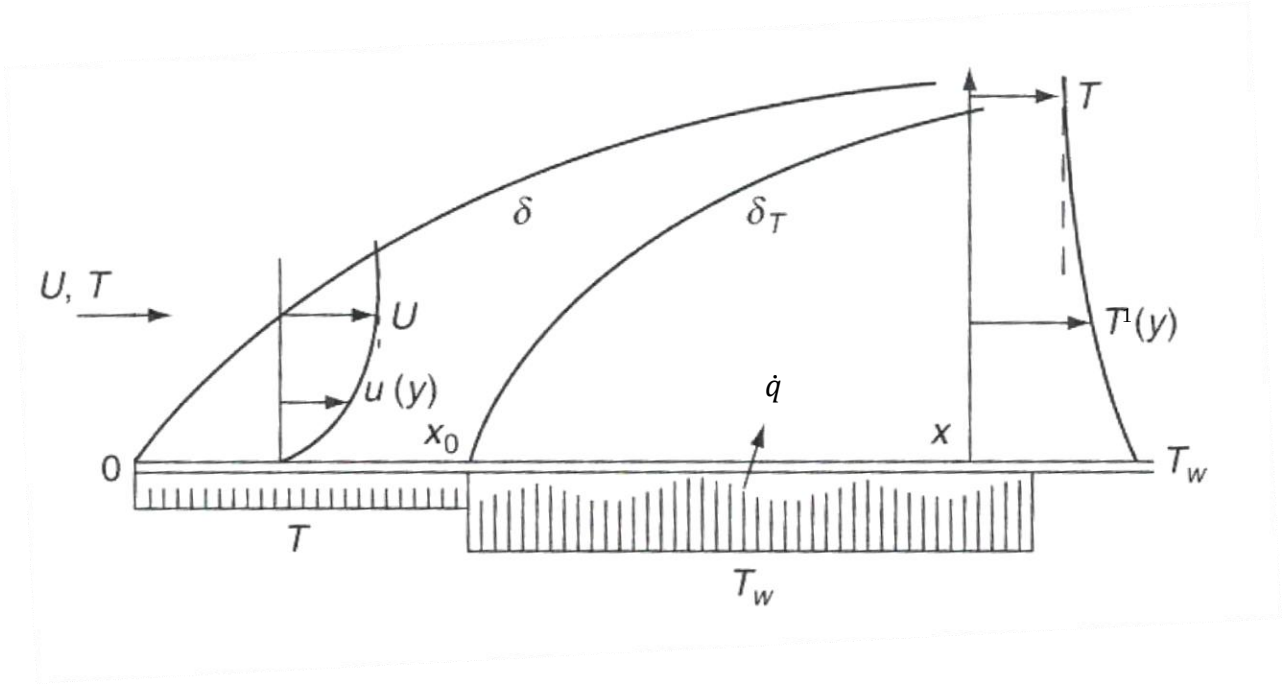

Figure 2-1 Schematic of laminar momentum and thermal boundary layer development along a flat plate. Adapted from (White 2006).

The boundary layer equations for compressible laminar flows remain coupled and must be solved simultaneously. Fortunately however these canonical flows are considered to be steady-state, where compressibility effects are relevant spatially only. Whereas, internal combustion engine flows are generally considered spatially incompressible, with a time-dependent density based on cycle phase and instantaneous cylinder volume. This assumption holds well except during

combustion where the hot burned gas region expands rapidly and compresses the unburnt gas ahead of the flame causes large disparities in density between the burned and unburned gas regions. But for the majority of the engine cycle spatial incompressibility holds which allows for comparisons to be made with the canonical incompressible boundary layer solutions.

2.2 The Steady Turbulent Boundary Layer

Where laminar flow is characterized by nonintersecting streaklines, the turbulent flow field is chaotic, containing statistically random velocity fluctuations. These fluctuations result from the growth of flow instabilities due to shear, either at a wall or due to mixing. The presence of instabilities is not unique to turbulent flow, they form in laminar flows as well but are dampened by the forces of viscosity and do not grow. In higher Reynolds number flows, momentum overcomes the effects of viscosity causing the disturbances to grow and the flow to eventually develop into a fully turbulent regime. The state where these disturbances are present and growing, but the flow not yet wholly turbulent, is known as the transition region. The critical Reynolds number based on streamwise length, Re_x, at which disturbances start to grow, is around 10^6. This process is represented by the instantaneous depiction of boundary layer thickness for a wall-bounded flow in Fig. 2-2.

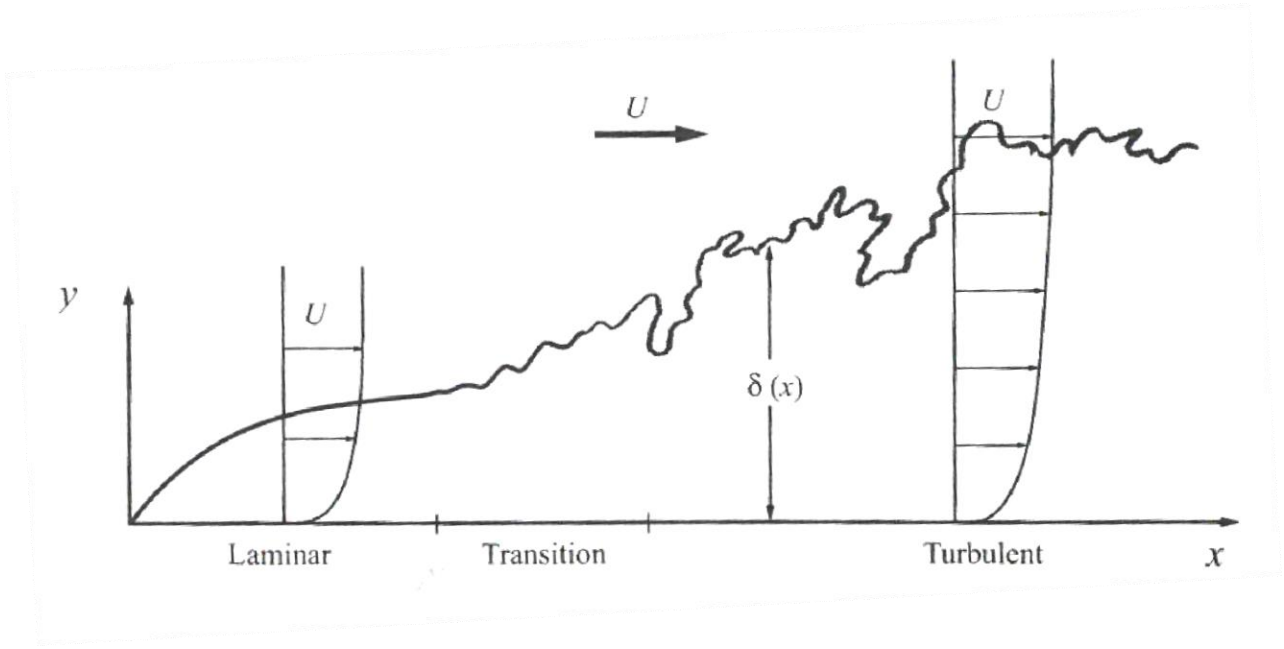

Figure 2-2 Instantaneous representation of boundary layer thickness for a wall-bounded flow, including the laminar, transition, and turbulent regions. Adapted from (Bernard and Wallace 2002).

Discussion of turbulent flow properties begins with the statistical analysis and separation of the fluctuations from the mean flow. This is achieved by defining

$$U = \bar{u} + u' \tag{2-2}$$

where U is the instantaneous velocity, $\bar{u}$ the average velocity, and u' the instantaneous fluctuation. Time, spatial, or ensemble averages may be used in this analysis. Average turbulence is often quantified by the root mean square of the instantaneous fluctuations

$$u_{rms} = \sqrt{\overline{u'^2}}. \tag{2-3}$$

This then allows for the calculation of the instantaneous and average turbulence intensity defined respectively by the ratios

$$\frac{u'}{\bar{u}} \text{ or } \frac{u_{rms}}{\bar{u}}. \tag{2-4}$$

Turbulent flat plate boundary layers are often described using dimensional analysis based upon the shear stress at the wall. This technique is named the “Law-of-the-Wall”. For these flows

the shear stress must be highest at the wall and decrease to zero far away from the wall. The velocity is made dimensionless by a fictional velocity, termed the "shear velocity", derived from the shear stress at the wall as in

$$u_\tau = \sqrt{\frac{\tau_w}{\rho}} \tag{2-5}$$

to generate the dimensionless velocity

$$U^+ = \frac{\bar{u}}{u_\tau}. \tag{2-6}$$

Likewise, the wall normal coordinate is made dimensionless by the wall shear stress and fluid properties

$$y^+ = \frac{y}{\nu}\sqrt{\frac{\tau_w}{\rho}}. \tag{2-7}$$

Experiments measuring the near wall velocity profile on flat plates at varying Reynolds numbers show that this Law of the Wall analysis works very well with all data collapsing to one curve up to the wake region as shown in Fig. 2-3. The logarithmic region is well described by

$$U^+ = \frac{1}{\kappa}\ln(y^+) + B \tag{2-8}$$

Where the Logarithmic-Law constants κ and B are commonly taken as 0.4 and 5 respectively (Kundu, Cohen et al. 2012). An alternative profile for the turbulent velocity profile can be built from

$$U^+ = C_1 y^{+C_2} \tag{2-9}$$

Where the constants C_1 and C_2 are functions of Reynold's number. C_2 is sometimes taken as a constant of 1/7, hence yielding the naming of "1/7th power law" for this choice of C_2.

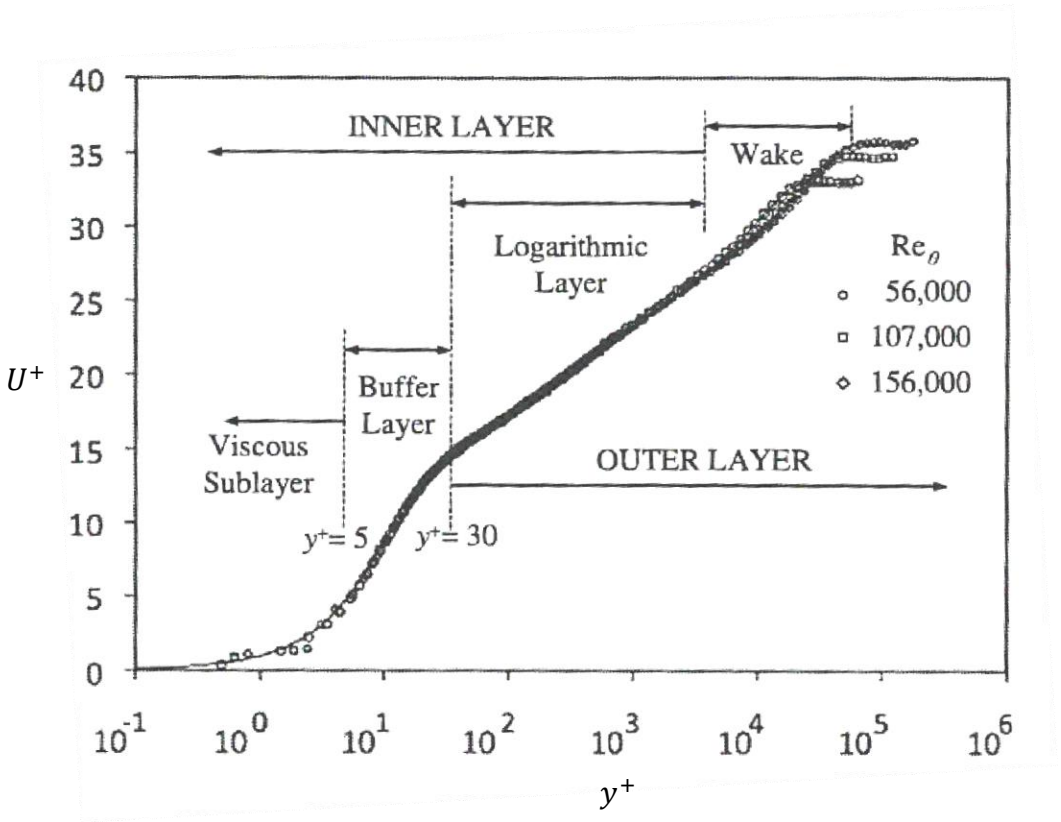

Figure 2-3 The Law of the Wall collapses experimental velocity distributions at various Reynolds numbers to a single line until the wake region. (Kundu, Cohen et al. 2012)

The above analysis describes the mean flow field of flat plate boundary layers quite well. But for a more detailed understanding of the nature of near-wall turbulence the fluctuations of the velocity field must be discussed as well. Near wall velocity fluctuations are often driven by the passing of turbulent structures advecting with the flow. The traditional coherent structures studied form due to shear at the wall. Many excellent references present the formation of hairpin vortices, and their coalescence into horseshoe vortices. Some examples are (Robinson 1991, Zhou, Adrian et al. 1996, Zhou, Adrian et al. 1999, Pope 2000, Bernard and Wallace 2002, Adrian 2007). Figure 2-4 shows an artist's representation of wall-shear generated structures advecting with a flow.

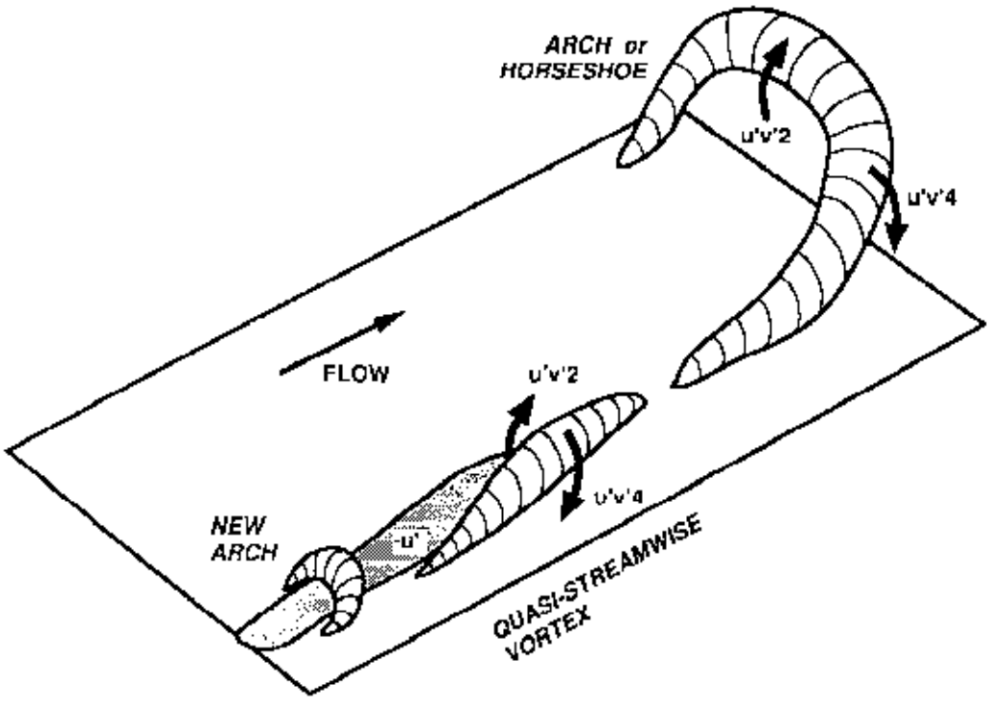

Figure 2-4 Drawing representation of some coherent turbulent structures within a boundary layer. (Robinson 1991)

Coherent turbulent structures often entrain fluid from both the bulk flow as well as from within the boundary layer which leads to the formations of both sweeps and ejections. A sweep occurs when high-speed fluid from outside the boundary layer is deep within it, while an ejection is when low-speed fluid from within the boundary layer is expelled into the free stream. The presence of sweeps and ejections can clearly be seen by plotting the velocity fluctuations on the $u'v'$ plane as shown in Fig. 2-5. Points located in the second quadrant are associated with ejection events while points plotted in the fourth quadrant correspond to sweep events.

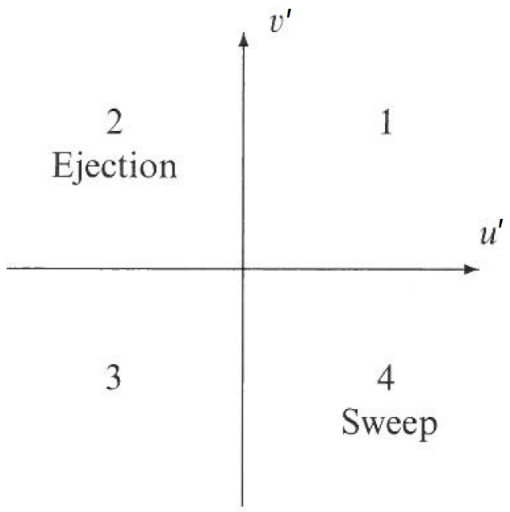

Figure 2-5 Location of sweep and ejection events in the u′v′ plane. Adapted from (Pope 2000).

The above discussion on turbulent boundary layers has been limited to those occurring on flat plates subjected to uniform flow. In this type of flow turbulence is generated by shear at the wall and diffuses into the bulk flow. This process is fundamentally different than that found in engines as will be seen in the following section. However due to the detailed understanding of flat plate boundary layer processes gained through an immense body of scientific research, these concepts form an important foundation upon which to build understanding of boundary layer processes in engines.

2.3 The RICE Near-wall Region

The most significant difference between flow in reciprocating internal combustion engines and the canonical flows discussed is the highly unsteady nature of in-cylinder flows. Investigation of the canonical flows discussed previously has been driven by steady external flows over airfoils and steady internal channel flows. But in engines the flow is highly unsteady as the piston alternatively covers and exposes roughly 60 percent of the in-cylinder surface area twice per cycle. This creates a pulsatile flow where the boundary layer is constantly restarting in these regions. While the boundary layer in the combustion chamber is not scraped by the piston motion it is subjected to high degrees of compression both by piston motion and flame propagation. Therefore low Mach number compressibility effects are important in studying in-cylinder flows as the order

of magnitude change in density and associated rise in temperature greatly alters the viscosity and the scaling of the dimensionless wall units and alters the spatial scale of the bulk turbulence.

Engine flows are driven by the reciprocating motion of the piston. As the piston falls during the intake stroke the generated vacuum pulls air from the intake port through the intake valves. The flow in the port can be related to pulsatile pipe flow. The flow around the valves is highly dependent on the instantaneous valve lift, and valve geometry. The quasi-axisymmetric flow around the valves is highly turbulent, with strong jets penetrating deep into the combustion chamber. Recirculation regions form under the valves and around the perimeter of the valve seats as the intake jet entrains air from within the cylinder. The intake process often generates a combination of two highly-turbulent large-scale flow structures: swirl and tumble flow. Swirl flow is a solid-body rotation about the cylinder axis and tumble flow a bulk rotation about an axis perpendicular to the cylinder axis. Drawings of swirl and tumble flow are depicted in Fig. 2-6. The amount of swirl or tumble in an engine can be controlled by valve and head design.

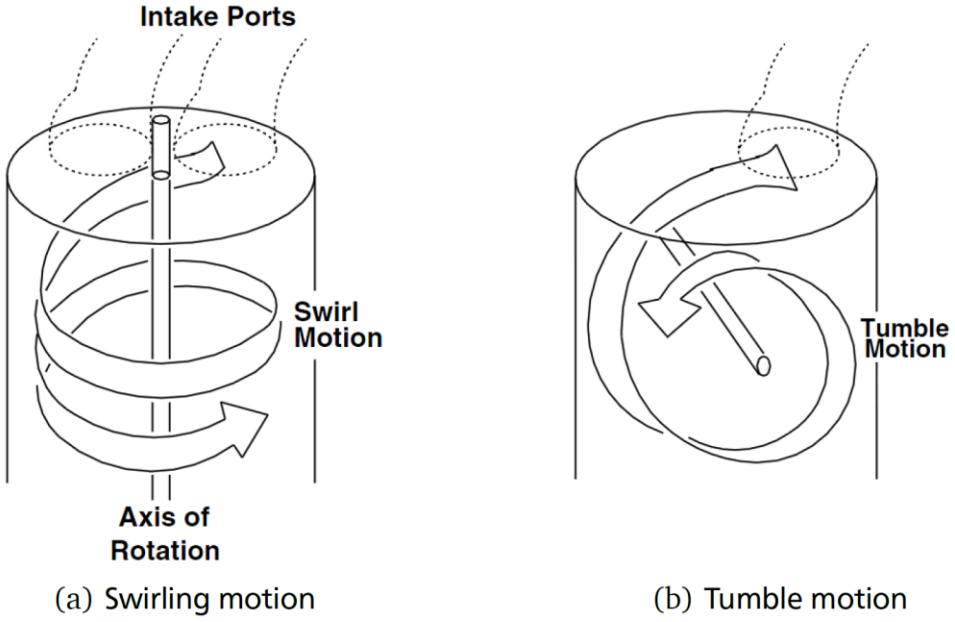

Figure 2-6 Drawings of characteristic in-cylinder bulk flows. (a) Swirling motion about cylinder axis, and (b) tumble motion about axis perpendicular to cylinder axis. (Laramee, Weiskopf et al. 2004)

During the compression stroke the piston compresses these large scale flow structures. In engines with highly directed flows this squish can result in significantly increased swirl velocities. In undirected engines however the compression of the turbulence results in a breakdown of large

structures and an associated increase in energy holding of smaller structures. The latter case is true for the TCC engine.

If we take a moment to reflect back to the classical depiction of a turbulent boundary layer presented in Fig. 2-2 we see that the flow phenomenon in an engine is quite different. In the classical depiction as the uniform flow begins over the plate edge a laminar boundary layer develops. Instabilities at the wall form due to shear and initially dissipate. As the flow progresses the momentum contained by the instabilities increases until eventually the instabilities no longer dissipate and instead start to grow. This development continues until the near wall region is filled with turbulence.

The flow structure in engines is quite different from this. In engines the bulk flow outside the boundary layer is wholly turbulent, and this turbulence is then imposed upon the boundary layer by both advection of the flow and compression from the piston. An order of magnitude calculation based on the critical transition Reynolds number $Re_{x,cr}$ of $\sim 10^6$, a free stream velocity of $\sim 10^1$ m/s, and kinematic viscosity of $\sim 10^{-5}$ m^2/s yields a streamwise distance of $\sim 10^0$ m for instabilities to begin to grow. This is yet an order of magnitude higher than length scales typically encountered in common engines! Therefore it is a reasonable hypothesis that wall-shear generated turbulence is not a significant phenomenon in engine boundary layers.

If engine boundary layers are not wholly turbulent, then what are they? Recall that laminar boundary layers are characterized by nonintersecting streaklines. Given the frequent interaction of vortices with the in-cylinder boundary layers this clearly cannot be the case. So engine boundary layers are neither classically laminar nor wholly turbulent. This conclusion is consistent with published research findings by (Pierce, Ghandhi et al. 1992, Alharbi and Sick 2009, Jainski, Lu et al. 2013).

In 2009 Alharbi and Sick compared the Blasius laminar profile (Equation 2-1) and the turbulent $1/7^{th}$ power law (Equation 2-9) to their measurements in a four valve pent roof engine motored at 800rpm. They found poor agreement between the models and the measurements, with agreements improving between the Blasius solution and measurements towards the end of the compression stroke. In 2013 Jainski et al compared motored measurements taken at 400-, 800-,

and 1100 rpm in the same engine with the Logarithmic Law model (Equation 2-8) again showing poor agreement between experiments and model predictions.

The poor agreement between these models and experiments is not surprising given the earlier discussion in the differences in the physics between the canonical flows for which these models were developed and validated, and the flows encountered in engines. The presence of wall generated turbulence in the former and free-stream imposed turbulence in the latter is a major difference. Furthermore the canonical flows discussed consider flows with only wall-parallel free stream flows, which is not an adequate boundary condition for all crank angles and locations in an engine. But given the complexity and vast array of factors compounding measurements in engines it would be useful if there were a canonical flow with inherent engine-like physics that could be studied on the benchtop. One such flow that tackles both the non-wall parallel free stream flow and imposes vorticity on the boundary layer is the impinging turbulent jet.

2.4 Steady Impinging Jet Boundary Layers

Unlike most of the canonical flows, in-cylinder boundary layers are characterized by free-stream vortical structures interacting with a laminar or developing boundary layer; whereas most bounded turbulent flows experience significant wall-shear generated turbulence production. Two canonical flows relevant to engines are the impinging turbulent jet and the turbulent wall jet as shown in Fig. 2-7 and Fig. 2-8. Of course an impinging jet becomes a wall jet away from the stagnation point, so the two are quite similar. Both of these flows share with engines boundary layers characterized by advected turbulence entering the viscous region. If the Reynolds number is low enough, or the region of interest short enough, these boundary layers will present laminar-like or developing characteristics just as in engines. Due to their similarities, and that the impinging jet includes physics at times relevant in engines due to the inclusion of wall normal flow, only results from impinging jets will be presented here. Large scale features of impulsive impinging jets have been studied and include additional features relevant to reciprocating internal-combustion engines (RICEs), mainly the pulsatile characteristics on the cylinder wall where the boundary layer is scraped twice per cycle by the piston. However, as will be seen in Chapter 4, the location under investigation at the cylinder head does not have these characteristics. Therefore due to the simpler

experiments and analysis of the steady impinging jet, only this flow will be discussed in this section.

For the steady impinging jet, if the Reynolds number is high enough in the jet's nozzle then the flow will be fully turbulent at the exit. Shear between the jet and surrounding fluid in the mixing layer between the nozzle and wall will generate additional flow instabilities and turbulent structures. Furthermore the flow at the stagnation point will also generate shear and vorticity. All of these turbulent structures are advected radially in the free stream flow and interact with the developing boundary layer. If the free stream velocity remains high enough wall-shear may cause the boundary layer to develop with similar characteristics to that shown in Fig. 2-2. However given that continuity requires the average velocity to decrease with increasing radial position this is unlikely for a large range of flow rates. This implies that for a large variety of operating conditions, wall-shear generated disturbances are damped in these boundary layers and turbulent fluctuations within are due to interactions with the free stream turbulence. These characteristics are the same as those found in engines, and make the turbulent impinging jet an excellent benchtop flow for comparison with IC engine research.

Due to the wide array of applications for impinging jets a vast amount of literature is available on their properties (Bovo and Davidson 2013). A significant amount of this literature concerns nearly exclusively with heat transfer (Sutera, Maeder et al. 1963, Gardon and Akfirat 1965, Sutera 1965, Baughn and Shimizu 1989, Hattori and Nagano 2004, Bovo and Davidson 2013). Another portion of these investigations have focused on the jet approaching the stagnation point (Angioletti, Di Tommaso et al. 2003, Tsubokura, Kobayashi et al. 2003). Still more work has been completed to measure the overall flow field (Landreth and Adrian 1990, Maurel and Solliec 2001, Jainski, Lu et al. 2014) but none of these investigations looked into the physics of vortex interactions in the boundary layer itself. Fortunately others did (Sakakibara, Hishida et al. 1997, Chung, Luo et al. 2002, Hadziabdic and Hanjalic 2008, Rohlfs, Haustein et al. 2012).

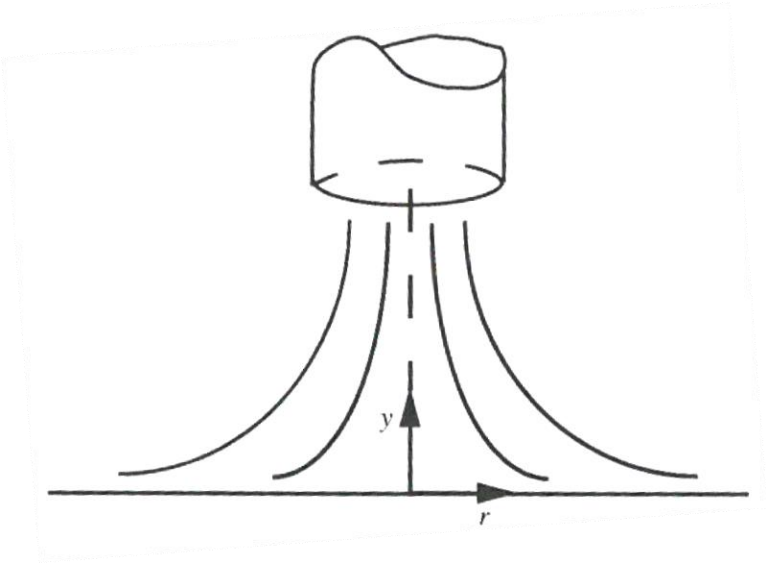

Figure 2-7 Representation of mean stream lines of a round impinging jet. Adapted from (Bernard and Wallace 2002).

Sakakibara et al. measured velocity, temperature and heat transfer near the stagnation point of a plane jet. Their thorough analysis used a joint probability density function to show that heat transfer is greatly enhanced by the ejection of hot fluid from the boundary layer, and used the mean-square vorticity fluctuation equation to explain the production of vorticity in the near wall region.

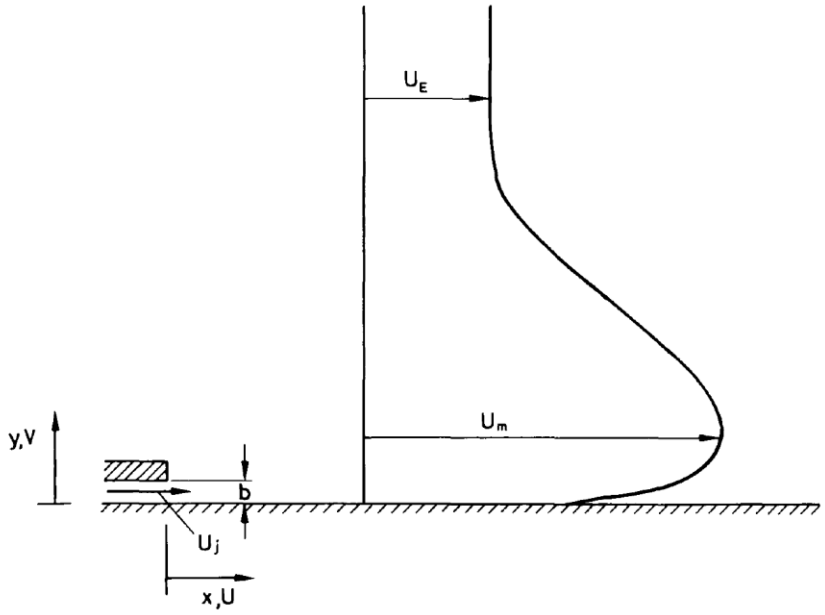

Figure 2-8 The velocity profile of a wall jet. Adapted from (Launder and Rodi 1979).

Chung et al 2002 noted the interaction of free-stream vortices produced by Kelvin-Helmholtz instabilities in the shear layer of the jet and the boundary layer of the round wall jet. They termed these structures primary vortices. They found that as the primary vortices expanded radially and approached the wall, secondary vortices formed at the wall causing a separation bubble of the boundary layer. Their DNS results predicted a spike in Nusselt number at the reattachment location as shown in Figure Fig. 2-9. This phenomenon was reproduced in the respective LES and DNS studies of (Hadziabdic and Hanjalic 2008) and (Rohlfs, Haustein et al. 2012), leading to the same conclusions regarding the underlying physical processes.

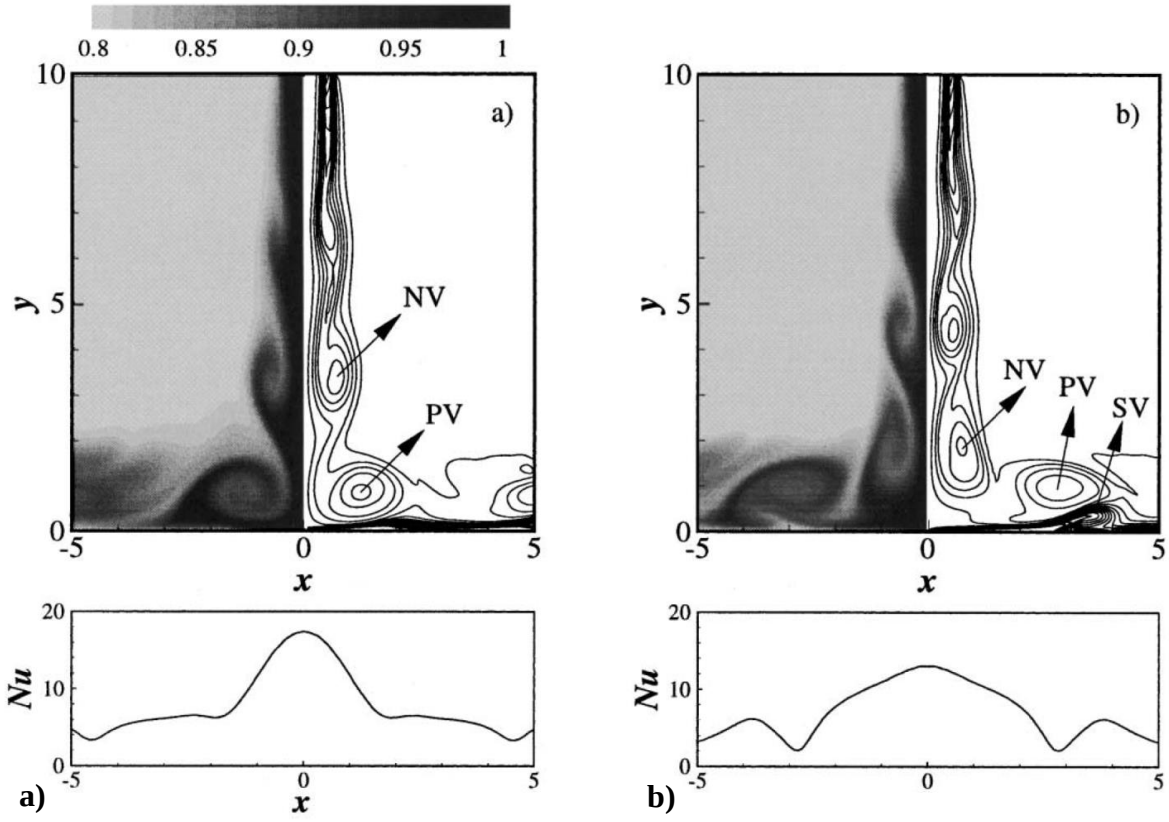

Figure 2-9 Results from (Chung, Luo et al. 2002) showing Kelvin-Helmholtz primary vortices (PV), the next primary vortex not yet interacting with the boundary layer (NV), and a second vortex generated by the interaction of the primary vortex and the wall. The lower plots show the impact of these vortices on the local Nusselt number. The grayscale image on the left plane of each image shows the temperature field of the flow.

Others have presented correlations for the centerline velocity of impinging jets, including plane impinging jets (Beltaos and Rajaratnam 1973). For $0.75 \leq x/H \leq 0.98$ at the end of the developed region into the impingement zone they recommend

$$\frac{U_C(x)}{U_0}\sqrt{\frac{H}{e}} = 5.5\sqrt{1-\frac{x}{H}} \qquad \text{2-10}$$

where U_C is the centerline velocity; U_0, e, and H the nozzle exit velocity, total nozzle width, and nozzle height; and x is the distance from the nozzle.

Chapter 3
Experimental Methodology

In recent years progress has been underway to extend the work of (Alharbi and Sick 2010, Jainski, Lu et al. 2013) that provided the first high-resolution planar particle image velocimetry measurements in engine boundary layers. The aim of the current work is to enhance physical understanding of boundary layer momentum transport processes while providing a limited database for validation of direct number simulation calculations and boundary layer submodels for large eddy simulations and Reynolds-averaged numerical simulations efforts. The current work is conducted in a canonical engine with a disk-shaped combustion chamber which provides a simplified physical geometry to facilitate ease of analysis and simulation. Unless otherwise noted, in the following sections any reference to boundary layers refers to in-cylinder momentum boundaries of internal combustion engines.

3.1 Particle Image and Particle Tracking Velocimetry

Particle image velocimetry (PIV) uses two laser pulses to illuminate particles seeded into a fluid flow twice which are then imaged by a camera. Traditional PIV systems measure two velocity components in a plane. More complicated arrangements are available to measure three components in a plane (stereoscopic PIV), and three components in a thin volume (holographic, tomographic, and plenoptic PIV). A typical planar PIV setup for a water tunnel is shown in Fig. 3-1. If the time delay between laser pulses, the resolution of the camera images, and the displacement of some particles in those images are known, then the flow field velocities may be determined. In PIV, displacements are calculated by computing cross correlations of small windows in image pairs (frames), as shown in the bottom left of Fig. 3-1. Depending on the nature of the flow one or two lasers may be necessary.

For the experiments of concern here two frequency-doubled Nd:YAG lasers are applied, each of which are capable of nominally producing 9 W at 3 kHz for a pulse energy of 2.9 mJ at 523 nm. These lasers are configured for single-mode operation which produces a Gaussian distributed beam that is highly focusable, as will be shown to important to these experiments.

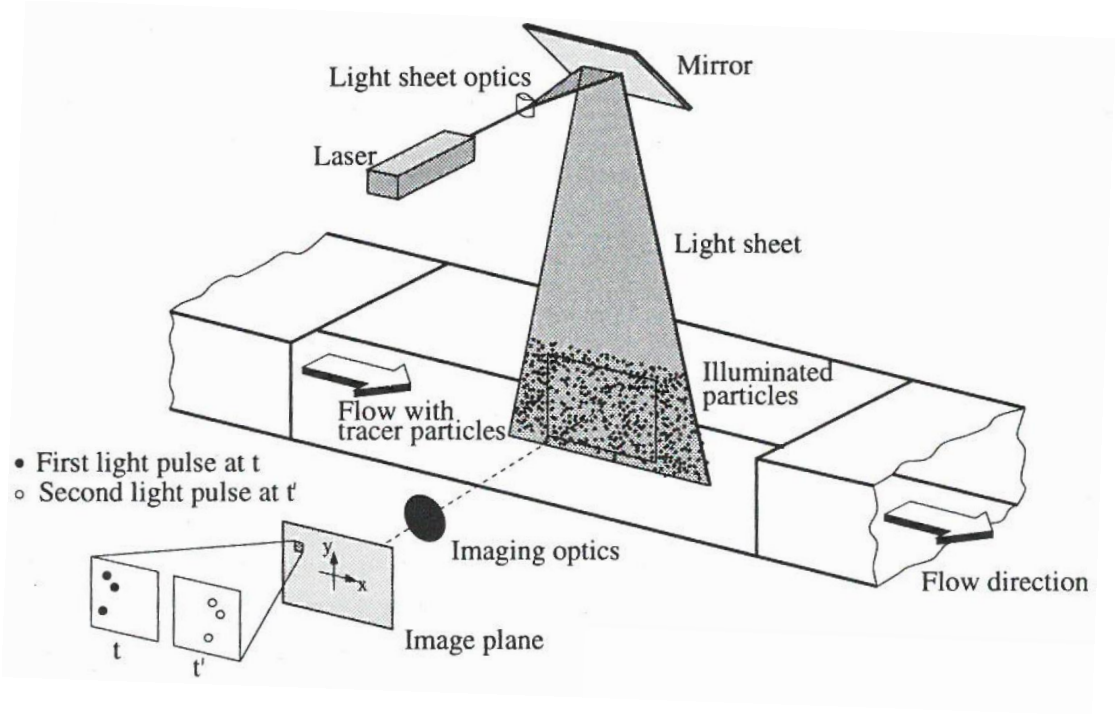

Figure 3-1 Typical PIV setup for a water tunnel. (Raffel, Willert et al. 1998)

Figure 3-2 shows the double frame method of PIV where each laser illumination is captured on a separate camera image, or frame. The frames are divided into small interrogation windows upon which the correlation function is applied between corresponding windows in each frame. Typically values of 16x16 or 32x32 pixels are chosen for the interrogation window size depending on the image sensor dimensions. Figure shows two such corresponding interrogation windows. A cross-correlation function is applied to them which generates a single velocity vector for the window. Therefore the spatial measurement resolution of the resultant velocity field is equal to the interrogation window size. Often it is desirable to overlap windows in order to increase the spatial sampling of the measurements, even though this does not increase the measurement resolution. An overlap of 50 percent is common. With an 800x600 pixel sensor, 32x32 pixel windows with a 50 percent overlap, 1875 vectors are produced on a 16x16 pixel grid at a spatial measurement resolution of 32 pixels.

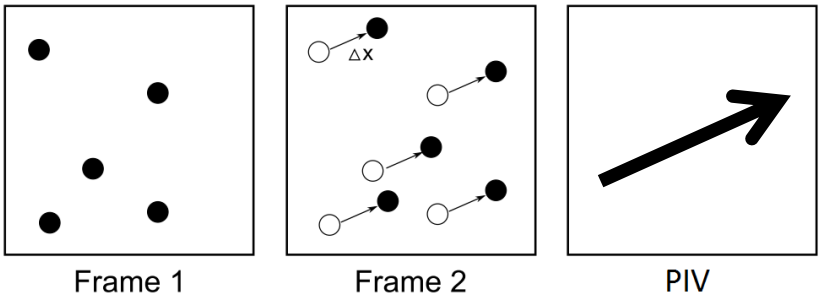

Figure 3-2 Double frame PIV method. Cross correlation of two corresponding camera interrogation windows (as shown in 'Frame 1' and 'Frame 2') generates a single velocity vector. See Figure for schematic of interrogation windows pulled from the image plane. Adapted from (Jainski 2011)

The maximum velocity resolvable by a given double-frame PIV system is determined by either the minimum pulse separation of the laser pulses or the interframe delay of the digital camera during which the chip is reading out the signal from the previous image. For systems utilizing two lasers the latter is usually the limiting factor. If higher velocities need to be measured, or if a higher temporal sampling is desired, a single-frame PIV method can be used. In single-frame PIV both laser pulses occur during one camera exposure creating a double-exposed image of the particle field. An autocorrelation function applied to interrogation windows generates a single velocity vector in a similar fashion as in double-frame PIV as shown in Fig. 3-3. As the research discussed in this work utilizes double-frame PIV, any reference to PIV hereafter refers to that method.

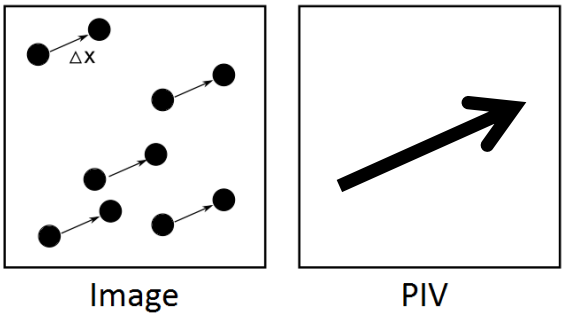

Figure 3-3 Single frame PIV method. Autocorrelation on camera interrogation window as shown on left generates single velocity vector as shown on right. Adapted from (Jainski 2011)

There are four additional very important considerations to the design of a PIV system. The first of these results from the laser sheet thickness. As a particle field with three components of velocity is illuminated by a laser sheet of finite thickness and imaged onto a 2D sensor, out of

plane particle displacements can have a negative effect on the PIV results. This can occur in two ways. First, particles can move through the sheet thickness during the pulse delay, such that either particles appear and disappear between frames, or this out-of-plane motion is captured as in-plane motion by the image sensor. The former instance can cause erroneous vector calculations as different particles form correlation peaks between frames, while the latter causes uncertainties in the in-plane velocity calculations. Concerns of sheet thickness and out-of-plane motion are minimized during investigations of largely 2D flows such as those in wind and water tunnels, but are a significant issue in engines due to the highly turbulent and non-stationary nature of in-cylinder flows.

The second consideration to PIV system design is selection of appropriate particles. It is of paramount importance that the particles be small and light enough to faithfully follow the flow structures while being large enough to be imaged by the camera system. However, the particles follow the flow structures due to the drag exerted upon them due to their relative velocity in the flow. Therefore the particles never follow the flow perfectly and it is up to each researcher to ensure that the error is small relative to the spatial and velocity resolution of the measurements.

The third consideration in PIV measurements is choosing the time delay between laser pulses to optimize particle displacement between frames. If the delay is too short then the particle displacement will be too small and the displacement cannot be determined accurately. If the delay is too long then the particle displacement will be too large and particle pairing will be lost. Generally it is best for the delay to be chosen to maintain particle displacements of 2-8 pixels. This can be difficult when imaging flow fields containing high velocity gradients, as found near walls and in eddies. In these situations a compromise must be found.

The final consideration when designing PIV systems is the particle seeding density. The correlation algorithm can be thought of calculating the shift of a particle pattern advected with the flow (Westerweel 1997). If there are too few particles per interrogation window then accuracy is lost, but if there are too many then the signal distribution around each particle becomes weak as the particles form a cloud of signal noise. It is known that PIV algorithms function optimally with approximately 8-10 particles per interrogation window. In some situations however this is not achievable, most notably in the boundary layer near surfaces where particles are rarely advected

into the viscous sublayer. This issue often requires over-seeding the bulk flow and therefore either a compromise must be had or an alternative particle image evaluation technique must be used.

Fortunately particle tracking velocimetry (PTV) offers a good alternative to PIV for velocity calculations in sparsely seeded flows. As shown in Fig. 3-4 the displacement of each particle is determined separately, yielding a single velocity vector for each particle in irregular locations. Typically the calculated vectors are then interpolated onto a regularly spaced grid. It can therefore be seen that for the same particle seeding density PTV offers a higher resolution measurement than PIV as it offers more vectors by a factor of the number of particles per interrogation window. For equal seeding density, the increase in spatial resolution over PIV is therefore equal to the square root of the interrogation window seeding concentration (Stitou and Riethmuller 2001). Unfortunately, due to unreliable particle matching the seeding density is usually reduced when using PTV compared to PIV. This results in a loss of the resolution benefit of PTV over PIV. However, PTV does provide a method to calculate velocity fields in flows too sparsely seeded for use with PIV, while still providing a slight benefit in spatial resolution compared to PIV under ideal circumstances.

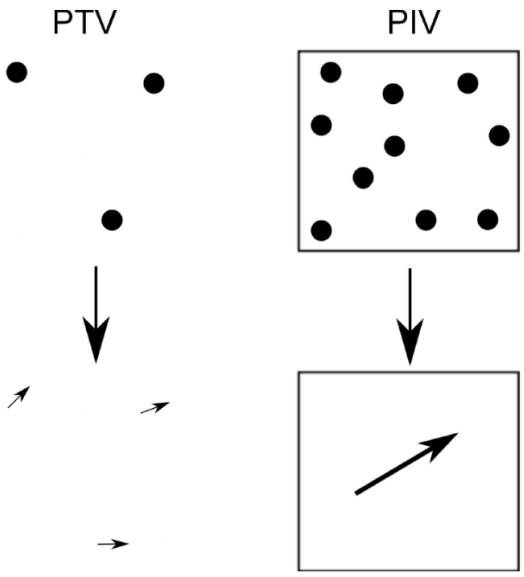

Figure 3-4 Diagram comparing PIV and PTV. Adapted from (Jainski 2011)

For sparsely seeded flows there is an alternative to PTV that provides excellent results if only averaged quantities are desired. In sum-of-correlations PIV the particle images are processed

as for regular PIV but the correlation planes are ensemble averaged before calculating the velocity vector for each interrogation window. This allows for very high resolution mean velocity measurements, with resolutions as high as a single pixel (Westerweel, Elsinga et al. 2013).

3.2 Transparent Combustion Chamber Engine

The current experiments were conducted in the Transparent Combustion Chamber (TCC-III) engine, which is described in detail in (Schiffmann, Gupta et al. 2016). The TCC-III engine was designed with simplified architecture to facilitate analysis and modeling, while maximizing optical access. As such it has two symmetrical valves with four-angle valve seats, a centrally located spark plug, simplified port and runner geometry, and features a 92 mm full quartz cylinder liner and piston window to allow optical access to the pancake-shaped combustion chamber. A schematic of the TCC-III engine is provided in Fig. 3-5 where yellow components represent quartz windows. The engine contains a Bowditch-style piston extension that provides optical access into the engine cylinder through a window in the center of the piston. Intake air properties are accurately controlled with sonic orifices and intake system heaters. Boundary conditions in the TCC-III engine are well documented by the five pressure transducers located in the intake and exhaust ports, the entrance to the intake plenum, the exit of the exhaust plenum, and within the cylinder. The TCC-III engine is also equipped with a dual-thermocouple heat-transfer probe. Due to the highly undirected intake jet the in-cylinder flow field of the TCC-III engine is characterized by high cycle-to-cycle variability (Reuss 2000, Schiffmann, Gupta et al., 2016). The cyclic phase notation used throughout this paper is crank angle degrees after top dead center exhaust (CA aTDCe) where the cycle starts at the beginning of the intake stroke, which lasts from 0 to 180 CA, followed by the compression from 180 to 360 CA, expansion from 360 to 540 CA, and exhaust from 540 to 720 CA.

Engine speed is regulated with a hydraulic dynomemter up to speeds of 2000 rpm. Some critical dimensions are presented in Table 3-1.

Valves are operated with a direct acting cam and designed for a 9 mm peak lift and slight overlap as shown in Fig. 3-6. Valve timing confirmed optically shows hydraulic lifter dynamics that reduce valve overlap to approximately 10 degrees.

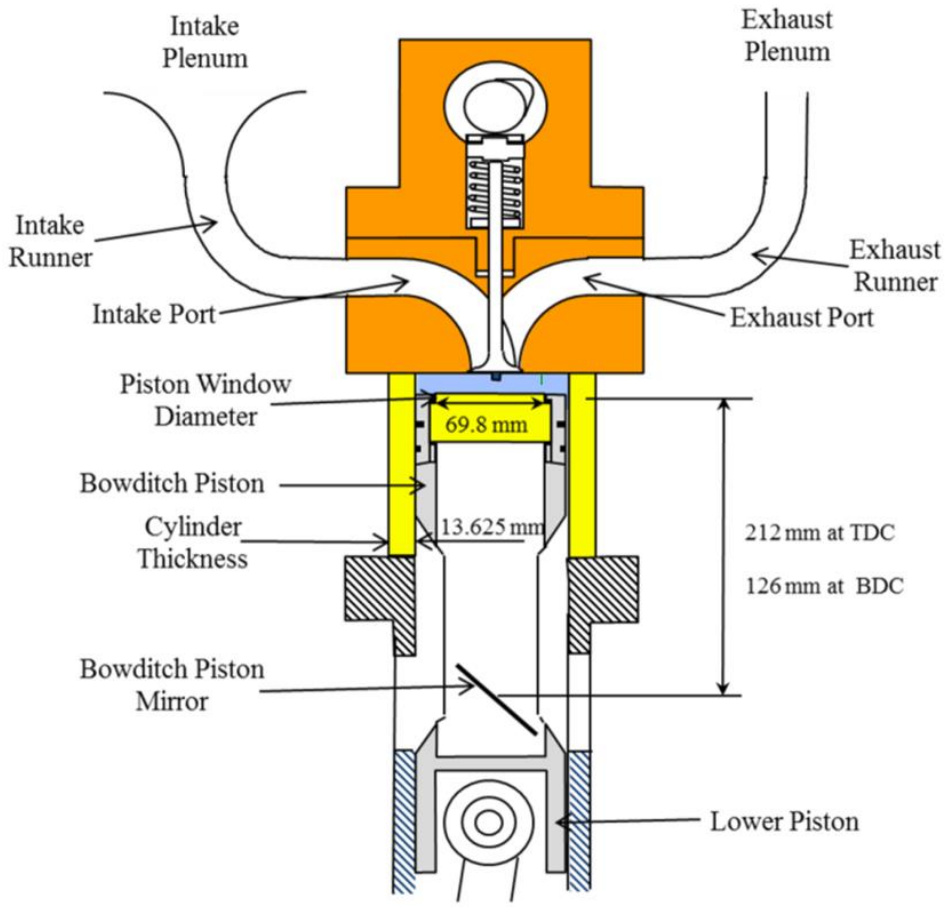

Figure 3-5 Diagram of TCC engine.

Table 3-1 TCC engine specifications.

Bore	92 mm
Stroke	86 mm
Compression Ratio	10
Valve Diameter	28 mm
Piston Window Diameter	70 mm
Cylinder Thickness	13.5 mm

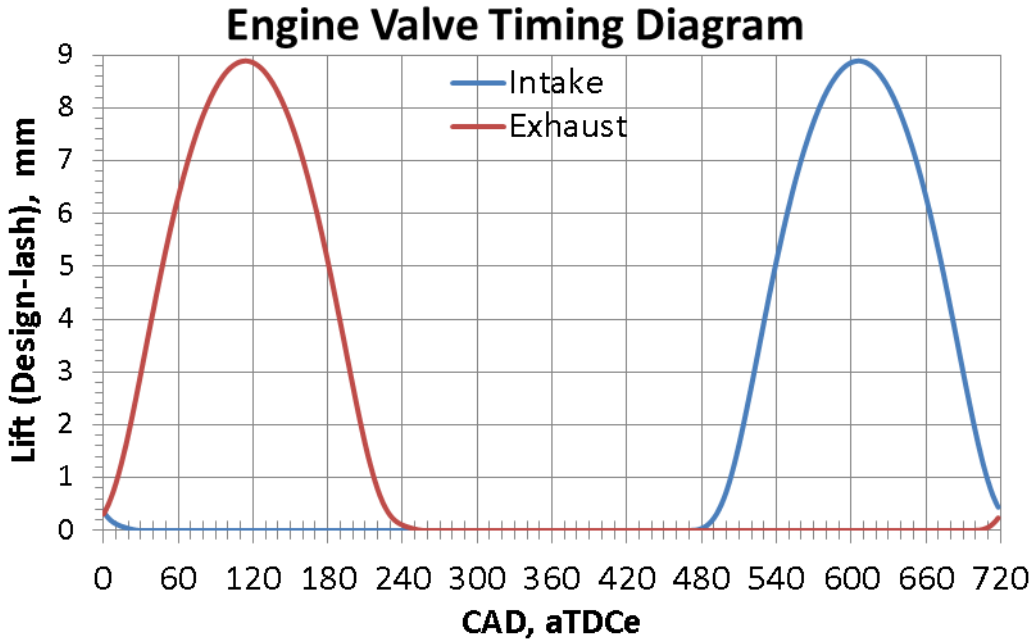

Figure 3-6 Engine valve timing diagram as designed.

3.3 Application of high-magnification PIV to the TCC engine

As seen in Chapter 1, a shortcoming of our understanding of physical transport processes in boundary layers exists. This knowledge gap is largely due to a lack of robust experimental investigation. For this reason particle image velocimetry has been applied to the boundary layer region of the TCC engine by imaging through a long distance microscope. The TCC engine has been chosen for this investigation as the simple geometry of the combustion chamber removes higher order bulk flow effects of more sophisticated head geometries. This facilitates the study of the development and interaction of in-cylinder boundary layers and the turbulent field imposed by the unsteady, compressible, low Mach number bulk flow.

The development of increased physical insight for engine heat transfer is driven by the need of higher accuracy models for advanced combustion strategy engines (Dec 2009). For this application the combustion chamber walls are the surfaces of interest as they control the heat transfer from the combustible charge prior to ignition. Therefore the surfaces on the head, cylinder walls near TDC, and piston, are the most relevant surfaces to be investigated experimentally.

The TCC-III engine does not provide optical access of the horizontal wall-normal plane at the cylinder wall as the metal outer portion of the piston blocks optical access. This is unfortunate as the importance of boundary layer investigations at this location have been highlighted by (Torregrosa, Olmeda et al. 2008). An alternative head for the TCC engine exists that includes a quartz prism above the cylinder at the edge of the head that allows for imaging down the side of the cylinder. This head could be used to measure the boundary layer due to swirl at the cylinder wall, but it would likely be more relevant to investigate the boundary layer formed at the cylinder wall due to gases driven by the oscillating piston motion. Unfortunately resolving the boundary layer at the cylinder wall in this vertical plane is not possible in the TCC engine. Unpublished exploratory investigations by Alharbi in the engine used for the experiments published in (Alharbi and Sick 2010) showed that measurements in this plane at the wall might be possible using stereo PIV. However, due to optical distortions this would not be possible at the spatial resolution required to adequately resolve the boundary layer.

For practical reasons this leaves the surfaces of the head and piston available for investigation as the quartz cylinder of the TCC-III engine provides optical access to the surfaces of the flat head and piston top. Though not without their own experimental challenges, previous PIV investigations in engine boundary layers were conducted by imaging through a flat plate which formed the head (Pierce, Ghandhi et al. 1992), or through flat windows installed in a pent roof head above the cylinder liner (Alharbi and Sick 2010, Jainski, Lu et al. 2013). The advantage of these engines is that all imaging could be performed through flat windows that introduce negligible distortions to the images. Unfortunately this is not the case with the TCC engine as imaging of boundary layers at the head or piston surface require imaging through the thick quartz cylinder which acts as a negative cylindrical lens. In this instance simplicity for analysis and modelling comes at the expense of enhanced experimental difficulty.

The distortions introduced by imaging through the 13.5 mm-thick quartz cylinder must be corrected before useful images can be obtained. At low magnifications (M=~1) this can be achieved by correcting for the cylindrical distortion in post-processing of the images. But at higher magnifications, such as a magnification of nearly 3 as used here, the astigmatic distortion caused by the cylinder must be corrected optically in order to form a proper image on the camera sensor at all. This was corrected with a cylindrical meniscus lens (-4 m focal length, 135 mm from

cylinder axis) used to apply an opposite distortion to that caused by the cylinder, following the work of (Reeves 1995). Figure 3-7 presents sample particle images with and without the corrective lens in place.

In Fig. 3-5 the degree to which the flat engine head (orange) extends beyond the measurement location is clearly evident. For the measurements taken at the head surface, this causes a problem for traditional imaging systems given the need for a high degree of image quality nearest the wall, as the head surface occludes the upper half of the imaging system as shown in Figure . This causes a decrease in signal level (photons) and increased aberrations, which result in non-physical velocity calculations characteristic of these near-wall PIV systems. This effect is shown in a simplified schematic in Fig. 3-8. The red lines represent the most extreme possible paths of light through the imaging system originating at a point at the bottom of the field of view (farthest from the wall). For even this point farthest from the wall, less than the whole imaging system is utilized, causing reduced signal counts and possible aberrations. Likewise, the blue lines represent the most extreme possible paths of light originating at a point located on the wall. For this point, only the bottom half of the optical system is utilized with the result of significant reductions in signal intensity.

The effect of on-axis imaging on PIV results at surfaces is well documented (Cierpka, Scharnowski et al. 2013). Figure 3-9 shows the characteristic velocity profile (blue) as calculated with PIV when imaging in this axial configuration, demonstrating a phenomenon the authors term a measured “velocity shelf”. The issue was not relevant to the previous work of (Alharbi and Sick 2010, Jainski, Lu et al. 2013), who imaged below a narrow raised boss in the pentroof of their engine.

As discussed in (Cierpka, Scharnowski et al. 2013) this velocity shelf is a common problem encountered in near-wall PIV experiments; these authors advocate use of an inclined imaging system in a Scheimpflug arrangement and even capitalize on this adaptation by utilizing the now captured particle image reflections off of the polished wall in their wind tunnel experiment to remove out-of-plane parallax errors. This modification allows for the use of the entire imaging system as the surface no longer covers the lens aperture. In the present study an inclined imaging

system was used for measurements taken at the head surface with the benefit of significantly increasing the

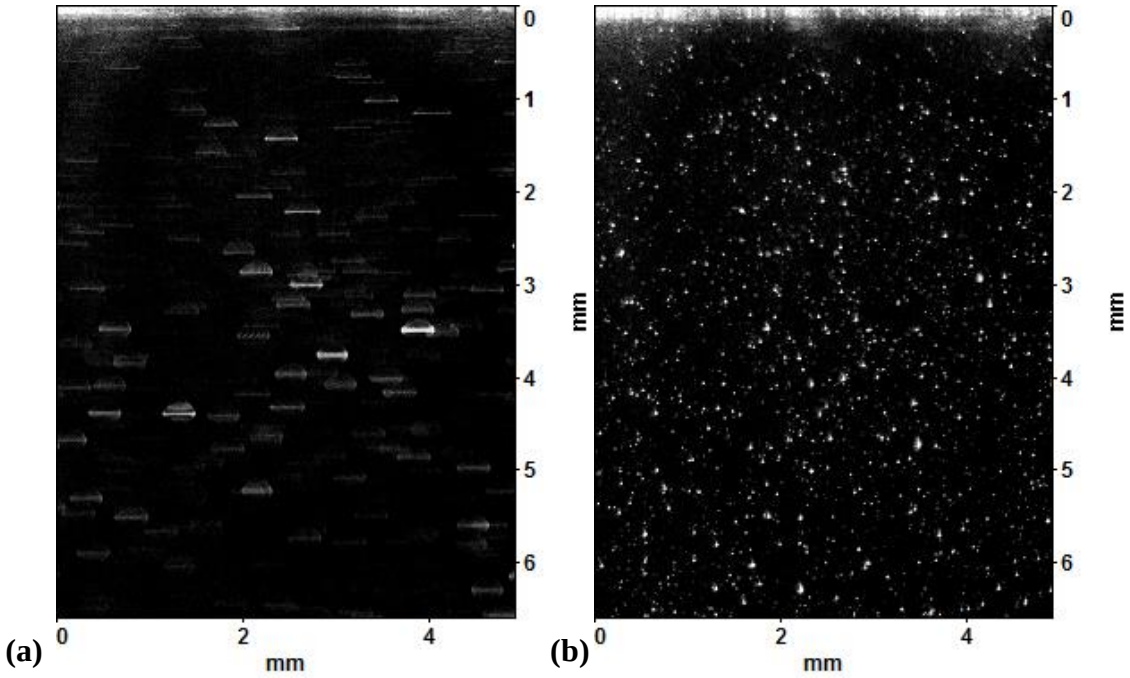

Figure 3-7 (left) uncorrected image of target shows strong astigmatism introduced by imaging through quartz cylinder (right) same target after installation of corrective optics.

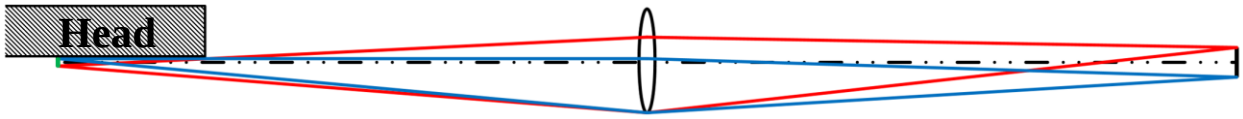

Figure 3-8 On-axis imaging at surfaces. The surface blocks light from half of the imaging system.

particle signal intensity nearest the wall. A simplified schematic of the adapted imaging system is shown in Fig. 3-10, where from the red and blue lines it is clear that the entire aperture of the collection lens is now utilized. This arrangement does however require tilting the image sensor relative to the imaging optics as shown in Fig. 3-10 which in these experiments was performed using a LaVision Scheimpflug adapter. A horizontal imaging system was utilized for measurements recorded at the piston surface.

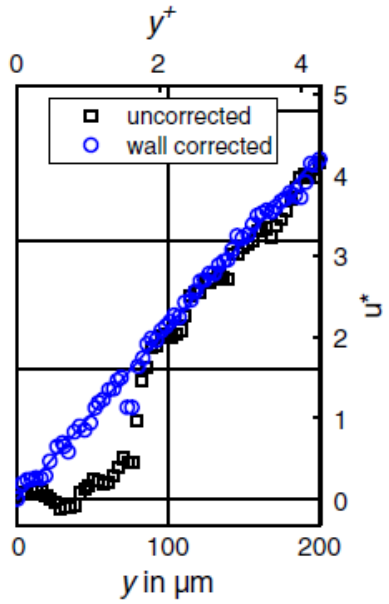

Figure 3-9 Characteristic (black) velocity profiles calculated from on-axis PIV near surfaces. The blue profile was measured with their proposed corrections. (Cierpka, Scharnowski et al. 2013)

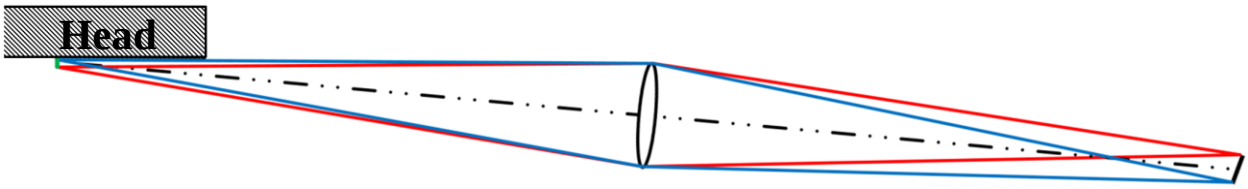

Figure 3-10 Correction proposed by (Cierpka, Scharnowski et al. 2013) to improve near wall imaging using a tilted optical axis in a Scheimpflug arrangement. Note the tilted image plane.

The final imaging system is presented in Fig. 3-11. Shown is a schematic of the engine head, the location of the lens used to correct for the astigmatism produced by imaging through the curved cylinder, the 200 mm Nikkor macro lens used as the objective, the 18.5 cm extension tube, and the camera, a Vision Research Phantom v7.3 mounted on a LaVision Scheimpflug mount. The lowest f/# available on the macro lens of 4.0 was used as it was found to form less aberrated particle images. The small f/# results in fewer aberrations caused by the oil film that forms on the cylinder wall during operation as it places the film farther out of focus. The Scheimpflug mount was set to tilt the camera at a 20-degree angle off of the optical axis of the lens. These approximate settings were later fine adjusted to maximize image quality.

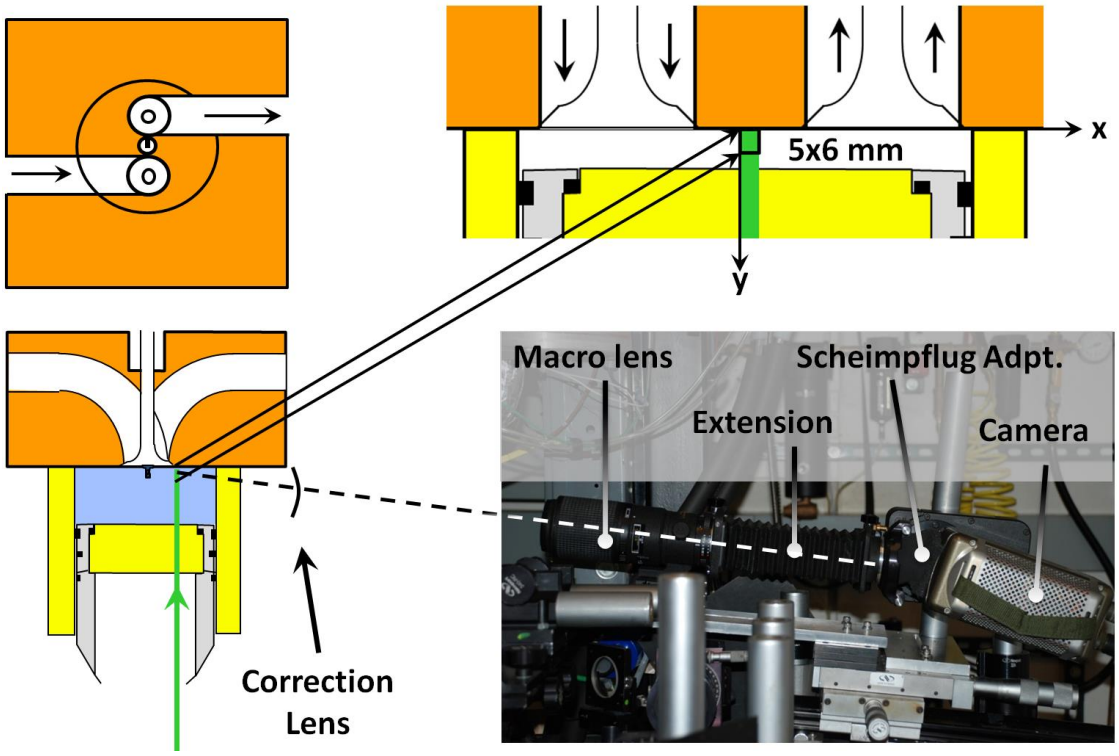

Figure 3-11 Optical system arrangement for imaging at the head surface of the TCC engine reflecting the tilted optical access and image plane in order to allow utilization of entire imaging system aperture. Measurements at the piston surface imaged the same laser sheet in a coordinate system attached to the piston surface with *y*-axis in the surface normal direction (i.e. upwards) from the piston surface. The *x*-axis remained in the same direction as shown in this figure.

In situ alignment of the imaging system was not possible due to the rapid cylinder fouling by the seed oil in the running engine. Focusing of the optical system includes: the main objective lens focus, the Scheimpflug adjustment, and the vertical and axial placement of the correction lens. The steady flow rig in Fig. 3-12 was built to facilitate optical system alignment and focusing. A spare cylinder and "head-surface" were positioned on the engine block at identical positions to the operating engine, and then replaced with the actual head for testing. Seeded air flows from the intake system, into the test cylinder, and then exits through the exhaust system.

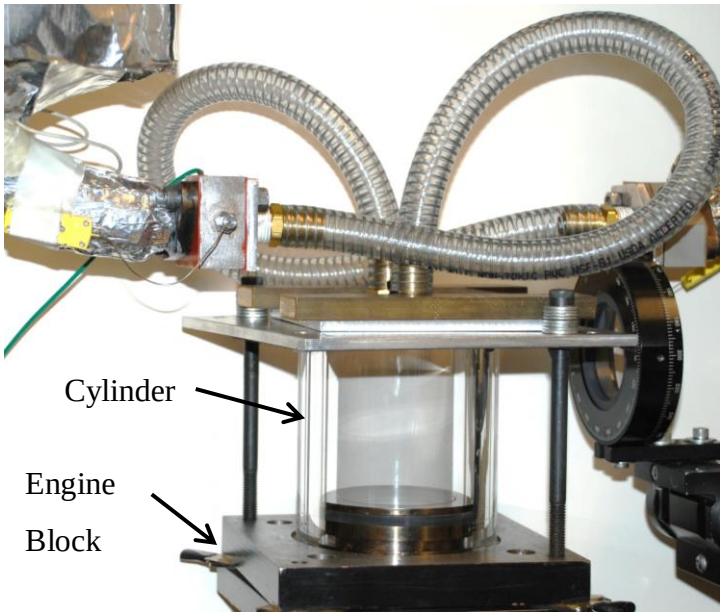

Figure 3-12 Alignment cylinder fixture used to focus imaging system (c.f. Fig 1). The corrective lens is visible on the right.

The laser light sheet was produced from two Quantronix Hawk II frequency-doubled Nd:YAG lasers, the beams of which were combined using a ½ wave plate and a Brewster plate then circularly polarized with a ¼ wave plate. The lasers have been modified to operate in a single-mode operation to provide low divergence, high beam quality, and stability. The light sheet was formed with custom sheet optics and beam homogenizer designed and built by the Center for Laser Technology of Fraunhofer-Gesellschaft. The optics consist of a cylindrical microlens array to homogenize the beam and produce a sheet, followed by a positive spherical lens to focus and collimate the sheet as discussed previously in (Jainski, Lu et al. 2013). The laser sheet thickness was 0.5 ± 0.1 mm within the measurement volume. The sheet was directed through the piston window terminating on the cylinder head wall. This results in a line of scattered light from the head in the images for the tests conducted at the head location, an unfortunate consequence of the engine geometry and experimental constraints. A similar line of scattered light from the piston surface was also visible in fired tests where the seed oil soot scattered the light. The use of this scattered light for identifying the wall position will be discussed below. The laser pulses and camera acquisition were phased to the engine crankshaft encoder by a LaVision High Speed Controller.

Particles were created using Dow Corning 510 50 cSt silicon oil, atomized by a TSI 6-jet atomizer, and introduced to the engine's intake system upstream of the intake plenum. The 185-kPa pressure drop across the atomizer produced a particle density of approximately 0.01 particles per pixel in the core region. A single atomizer jet was used for the measurements at 500 rpm, while four jets were used for the measurements at 1300 rpm. The TSI atomizer utilizes the Venturi effect to draw seed oil into the supplied air stream by way of straws between the air channel and oil reservoir. These straws were removed from the remaining two jets of the 6-jet atomizer during the 1300 rpm tests, thereby allowing them to introduce dilution air into the seeded air flow to prevent particle agglomeration downstream of the atomizer. When imaged by the imaging system described below, the particles produced an image size of approximately 2 pixels. Unlike steady-flow wall layers that can be seeded upstream at the wall (Kähler, Scholz et al. 2006), here the seeding is only present near the wall following turbulent injection events from the core-region turbulence. Thus, the wall-layer measured statistics are conditionally sampled by the presence of seed particles introduced by injection events; this effect on the results must be recognized, but quantification is beyond the scope of this paper.

Determining the exact location of the wall in images is an inherent challenge to all boundary layer experiments. For this purpose, the alignment cylinder in Fig. 3-12 was used to create and validate a procedure that could be used during the testing. In particular, the location of peak image intensity from the light scattering at the head surface (due to the terminated laser sheet) was found to be coincident with wall position. The validation of this is described with the aid of Fig. 3-13. Figure 3-13(a) shows an image of wall scattered laser light off of the clean head surface, along with the average in the horizontal direction to obtain a mean intensity profile in the vertical direction. The estimate for the wall location in the image is taken as the location of peak intensity of the profile. In Fig. 3-13(b) the head surface was coated with seed oil so that particle images and their reflections could be identified. It was found that the image intensity peak bisected each image/reflection pair (c.f. Fig. 3-13(b)); the head location calculated with this method differed by only 11 μm from that computed as shown in Fig. 3-13(a). Since the particle image reflections were not visible when the engine was running, the laser-scattered intensity peak is identified for all images to determine the estimate of the wall location in each image. To further complicate matters in this experiment, the wall of interest is the head surface of a running, and vibrating, engine. Significant effort has been placed to mechanically isolate the engine from the optical table

to which the diagnostics are mounted, as well as stiffen the camera support structure. Despite any remaining vibrations and measurement noise the standard deviation of the estimated wall location for all images in each dataset is less than one pixel (8 µm) at 500 rpm.

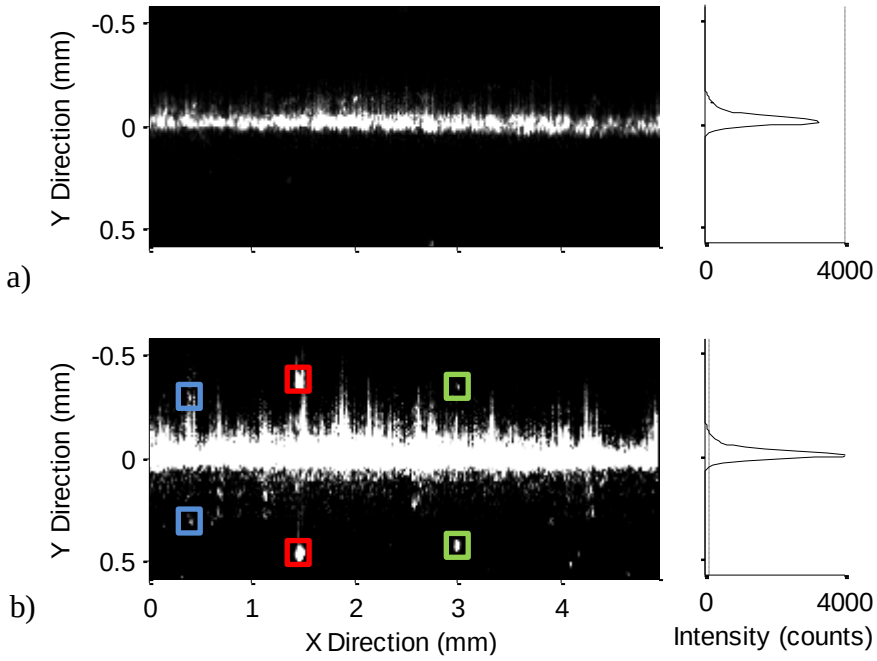

Figure 3-13 To determine the location of the head surface in the images; a) each image is averaged in the horizontal direction to develop an average intensity profile as shown on the right. b) Location of particle images and their reflections as seen with a seed oil film applied to the test head with the engine stationary.

Due to the large variation in in-cylinder velocities over the course of each cycle it was necessary to vary the laser pulse delay as a function of CA to ensure optimum velocity dynamic range for each image. The delay between laser pulses was varied as a function of crank angle as in (Abraham, Reuss et al. 2013), with the delay iteratively optimized for a spatial and ensemble average pixel shift of 3 pixels. This small pixel shift was required to limit the number of particle pair losses due to out of plane motion in this highly three-dimensional in-cylinder flow.

All PIV processing was conducted in LaVision's DaVis 8.2.3.3902 software. The image preprocessing steps used to obtain the best vector quality nearest the surface consisted of a subtract minimum time filter followed by a particle intensity normalization filter with a scale length of 10 pixels. The subtract minimum time filter was computed over either the entire cycle, or the entire ensemble at each crank angle. The direction the subtract minimum time filter was applied did not

affect vector quality, with the former direction applied to data collected at the head surface and the latter direction applied to data recorded on the piston surface to facilitate following processing steps.

Great care was taken to align the vector grid to the surface to ensure highest nearest-wall vector quality. As DaVis places the vector grid from the top-left corner of the images, the images recorded on the piston surface were flipped vertically. Most of the pixels above the surface were removed from the images so that a uniform number of pixels could be obtained between the top of the images and the surface location. As the final interrogation window size was 32x32 pixels with 50 percent overlap, 8 pixels above the surfaces were retained in the images so that the first vector grid row would be directly at the wall. These pixels above the wall were masked out before vector calculation. Additionally, the first 16 pixels below the wall were masked out in order to eliminate the light sheet reflection. This provided a distance of 250 µm from the first vector to the wall.

The vector calculation routine used a decreasing window scheme starting with one pass at 128x128 pixels at 75 percent overlap with square interrogation window shape, down to two passes at a final window size of 32x32 pixels at 50 percent overlap with a round interrogation window shape. This resulted in a vector spatial resolution of less than 250 µm oversampled to a final vector spacing of 125 µm. A B-spline high accuracy technique was used for final passes and vector-by-vector uncertainty estimates based on the correlation statistics approach were calculated (Neal, Sciacchitano et al. 2015, Sciacchitano, Neal et al. 2015, Wieneke 2015). Significant improvement in vector quality was achieved by using a direct correlation (rather than an FFT as typically used) for the final correlation pass.

The vector post-processing settings used for these calculations consisted of a maximum allowable pixel shift of 15 pixels, and an outlier detection scheme. These vector calculations were computed along with uncertainty estimations of each individual vector following the correlation statistics approach recently presented by (Neal, Sciacchitano et al. 2015, Sciacchitano, Neal et al. 2015, Wieneke 2015). No smoothing or interpolation functions have been applied to any of the results presented in this paper.

As a consequence of the masking above the wall, the 250 µm spatial resolution, and flow dependent seeding, it was not expected to resolve a “viscous sublayer” as found in steady boundary

layers. Rather, the methods here were expected to allow quantification of the spatial extent to which the wall affects the flow in the in-cylinder core region. A similar analysis was presented for a study on a heated impinging jet that examined how outer-flow statistics changed as the wall was approached (Jainski, Lu et al. 2014).

The high-magnification, near-wall PIV results presented in this paper were taken from a measurement plane located in line with the cylinder axis and offset 28 mm towards the camera from the centrally located sparkplug, as shown in Fig. 3-15. Mechanical interference between the corrective lens mount and the head prevents moving the measurement location any closer to the sparkplug. The 28 mm offset was within the range for which the corrective lens could be positioned without interference, and was chosen to match the radial position of the valves. Yellow components in Fig. 3-15 are quartz elements. The placement of the measurement volume was limited to along the cylinder centerline to minimize off-axis distortions created by the cylinder. The measurement volume was offset from the sparkplug to avoid interferences caused in the near-wall flow field around the sparkplug. As DNS investigations of the near-wall layer behavior and heat transfer characteristics have found a strong correlation between wall-normal velocity and heat flux even as far as 1 mm away from the wall (Schmitt 2014), a large field of view of 6 mm from the wall was chosen. Resolving the viscous sublayer profile was deemed to have limited utility towards understanding flow and heat transfer characteristics in engines compared to the core flow that drives in-cylinder flow. The 6-mm field of view allows sampling within the core flow, in fact out to the mid-plane of the clearance height at TDC.

The surface temperature and heat flux data were measured with a microsecond response Medtherm TCS-244-JU(JU-.156)-72-11340 heat transfer probe positioned 35.5 mm from the cylinder axis as shown in Fig. 3-15. One type J thermocouple was set at the probe surface, with a second thermocouple set 3.96 mm into the depth of the probe material. Thermocouple voltages were sampled by RC Electronics DTX-520CJ cold-junction module assemblies including electronic cold-junction temperature compensation. Thermocouple signals were amplified and converted to a 0-10 V signal linearized to temperature by an RC Electronics DTX-5120 thermocouple conditioner mounted in a DTX-5017 rackmount chassis. The 0-10 V linear thermocouple signals were recorded by the crank-angle based A&D Phoenix AM system that also records the high-speed pressure measurements in the engine. The surface and in-depth

temperatures were recorded every 0.5 CAD throughout the cycle. The Medtherm heat flux probe was installed vertically in a spare spark-plug hole and mounted flush with the TCC-III engine head.

The instantaneous heat flux was calculated from the surface and in-depth temperatures following the procedure set forth by (Nijeweme, Kok et al. 2001):

$$\dot{q}_s = k\frac{\overline{T_s}-\overline{T_{id}}}{l} + k\sum_{n=1}^{N}\frac{\sqrt{n\omega}}{2\alpha}\left[(A_n+B_n)\cos(n\omega t)+(B_n-A_n)\sin(n\omega t)\right] \qquad 3\text{-}1$$

where $\dot{q}_s$ is the instantaneous heat flux calculated at the surface, k and α are the thermal conductivity and thermal diffusivity of the probe material, $\overline{T_s}$ and $\overline{T_{id}}$ are the cycle-averaged surface and in-depth temperatures, and A_n and B_n are the coefficients of the Fourier series expansion of the surface temperature trace.

Data acquisition and diagnostic timing were controlled by LaVision's DaVis 8.2 software and a High-Speed Controller (HSC), respectively. The HSC was timed from the Engine System Controller via a 1 pulse/cycle and 2 pulse/CAD TTC signals. The HSC drove the Q-switch signal to the laser and the Frame-Sync and Trigger signals to the camera as shown in Fig. 3-14. The thermocouple signals from the heat transfer probe were recorded by the Combustion Analysis software along with the high-speed pressure transducer signals (not shown).

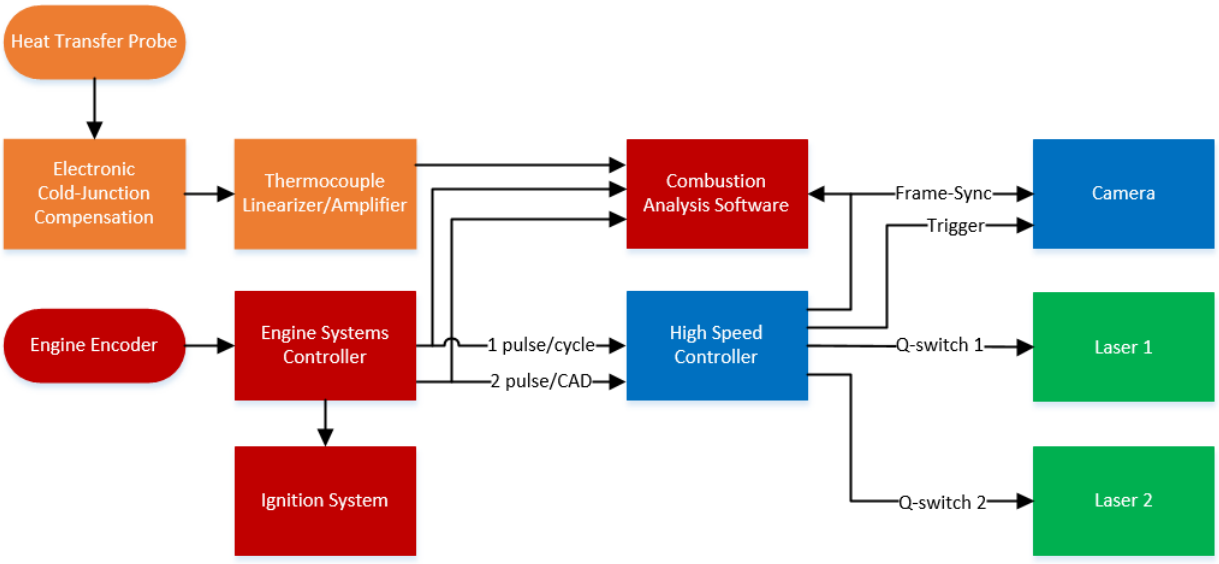

Figure 3-14 Engine systems signal diagram.

3.4 Overview of test conditions measured

The PIV system described in the Experimental section above was utilized to measure the near-wall region planar velocity field in the TCC engine operated at 500- and 1300 rpm under both motored and fired conditions. In all tests the intake system pressure was maintained at 40 kPa with an intake temperature of 80 °C as measured at the intake port. The cooling water was also maintained at 80 °C. For the fired experiments the engine was operated with homogeneous propane/air mixtures with a spark timing of 342 CA. For motored experiments the engine was operated with air only. Measurements were taken at the cylinder head as well as on the piston surface, accompanied by simultaneous head surface temperature and heat flux measurements. Figure 3-15 presents a schematic of the in-cylinder geometry including the location of the PIV measurement location as viewed from above, as well as the location of the head-surface temperature and heat-flux probe. The location of the PIV measurement volume in the horizontal plane as shown in Fig. 3-15 was identical for experiments conducted at the head and piston surfaces.

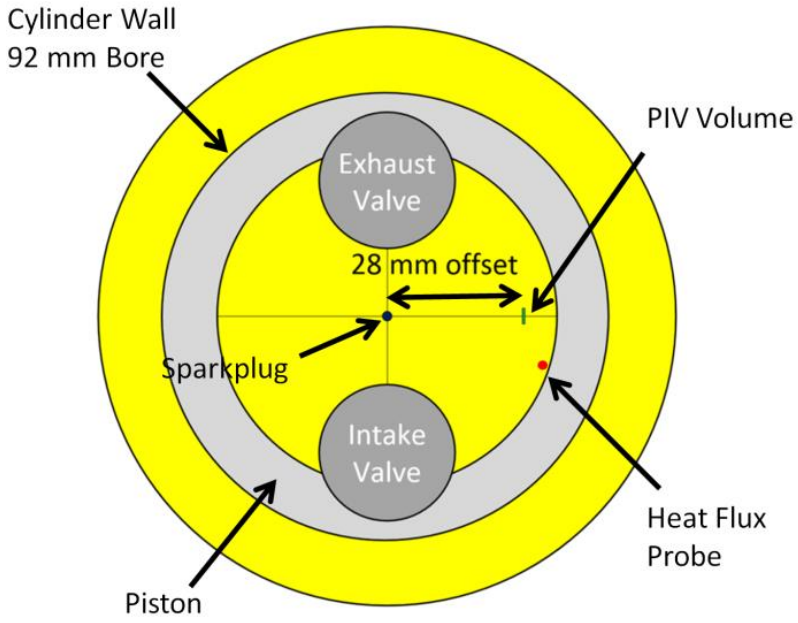

Figure 3-15 Measurement location on a vertical plane (out of the page) in the engine as viewed through the head. Vertically, the measurement location was positioned just below the head surface. Yellow is quartz and grey, steel.

Table 3-2 presents the measurements at the head surface location and shows the imaging interval in CAs, the recorded crank angle ranges, cycles recorded, and the number of tests with these parameters. Effort was made to acquire as close to cycle-resolved measurements as possible, but as can be seen in the 'recorded CAs' column, vectors were not able to be calculated for some crank angle ranges. In motored tests, a strong out of plane flow precluded PIV calculations for a crank angle range while the exhaust valve was open. As no seed remained in the cylinder during fired tests at the start of each cycle (TDCe), PIV calculations could not be performed until sufficient seed was drawn into the cylinder with the fresh charge and sufficiently mixed with the residual gases to permit PIV calculations to be made. Due to a limited camera memory of 16 GB it was necessary to balance the need between tests containing a high number of cycles to build statistics, with a need for high crank-angle resolution to observe flow developments. To meet these needs tests at two different imaging intervals were taken for each engine condition, as shown in Table 3-2. In motored operation at both engine speeds tests were conducted with 10 CA imaging intervals to record 141 consecutive cycles per test to build statistics on flow characteristics. Besides camera memory, the upper limit on the number of recorded cycles per test in motored operation was also limited by fouling of the cylinder wall by the seed oil. As images were only taken up to TDCc in fired operation due to consumption of seed particles by the flame, a smaller imaging interval was achievable and an interval of 5 CAD was chosen for both 500- and 1300 rpm which yielded 184 consecutively recorded cycles per test. For the flow visualization tests, the smallest possible imaging interval of 1 CA for 500 rpm and 2.5 CA for 1300 rpm was used, limited only by the maximum camera frame rate of 3.3 kHz. More consecutive cycles were able to be recorded in fired operation than motored operation as the soot film on the cylinder wall caused a slower degradation in image quality than the seed oil film formed during motored operation.

Table 3-2 Head surface location dataset parameters.

Speed (RPM)	State	Interval (CA)	Recorded CAs	Cycles Recorded	Tests
500	Motored	10 1	0-490;550-710 0-490;550-716	141 14	6 5
500	Fired	5 1	90-350 90-350	184 37	5 3
1300	Motored	10 2.5	0-490;620-710 0-490;620-710	141 35	6 2
1300	Fired	5 2.5	120-350 120-350	184 93	4 2

Table 3-3 presents the test information for each operating condition for measurements conducted on the piston surface. Measurements were taken as the piston traversed the field of view for three different camera heights that corresponded to TDC (360 CA), late compression (315 CA), and BDC (180 CA). If possible, given the same crank angle restraints as discussed above regarding lack of seed particles in fired tests during the early intake stroke and after combustion, measurements were taken each time the piston crossed the field of view, up to four times per cycle. Due to the small number of crank angles the piston was within the field of view, the number of recorded cycles was not limited by camera memory so the camera was operated at its maximum frame rate. The number of consecutively recorded cycles per test was still limited by cylinder fouling, especially for the tests conducted near TDC.

Table 3-3 Piston surface location dataset parameters.

Speed (RPM)	State	Location	Interval (CAD)	Recorded CAs	Cycles Recorded	Tests
500	Motored	TDC	1	0-13;347-373;707-716	199	4
		Late Comp.		38-45;315-323;397-405;675-682	195	4
		BDC		167-193;527-553	188	4
500	Fired	TDC	1	347-360	200	5
		Near TDC		315-323	400	4
		BDC		155-205	199-376	4
1300	Motored	TDC	2.5	0-12.5;347.5-372.5;707.5-710	200	4
		Near TDC		37.5-45;315-322.5;397.5-405;675-682.5	200-634	5
		BDC		150-210;510-570	203	4
1300	Fired	TDC	2.5	347.5-357.5	201	4

Chapter 4
Results

The results of the experiments will be presented in four sections. Section 4.1 will present observations from flow visualizations from individual vector fields. The near-wall region at the cylinder head will be discussed in Sections 4.2. Section 4.3 will introduce the results of measurements on the piston surface, and compare these results with those taken at the head surface. In Section 4.4 the temperature and heat flux measurements will be discussed.

4.1 Flow visualization

Figure 4-1 presents three of the commonly observed flows encountered in internal-combustion engine near-wall regions. Figure 4-1(a) shows an example of a vortical structure adjacent to the wall. These structures are formed in the core flow as the large scale flow structures break down and are compressed towards the wall by the piston motion. This vortex is approximately 2 mm in diameter and has been pushed right up against the wall, with its center 1 mm from the wall. This phenomenon of core-flow vortical structures interacting with the wall layer can have more similarities with impinging-jet flows than traditional flat-plate boundary layers. The relationships between vortex/wall interaction and heat transfer have been well studied in impinging-jet flows (Hadziabdic and Hanjalic 2008, Rohlfs, Haustein et al. 2012, Bovo and Davidson 2013, Jainski, Lu et al. 2014), but its application to engine wall models has not been examined.

Figure 4-1(b) shows an instantaneous flow structure resembling an impinging jet as close as 0.198 mm from the wall; of course continuity requires a strong out of plane component. The recent DNS results of the Imperial College single-valve compression/expansion machine showed strong correlations between wall-normal velocity and heat flux as far as 1 mm from the head (Schmitt

2014). They found (c.f. Figure 5.28 in (Schmitt 2014)) a strong correlation between wall-normal velocity and heat flux on a cutting plane 0.1875 mm down from their flat cylinder head, which is very nearly the same distance as the first vector from the wall in Fig. 4-1(b) here. From their DNS results, they found flow towards the wall to generate high and distorted heat flux fields on the cylinder head, while flow away from the wall caused low and uniform heat flux (c.f. Figure 5.30(a) in (Schmitt 2014)). The possibility to develop wall heat transfer models for internal-combustion engines based upon the wall-normal velocity component near the wall, even on a coarse grid, holds great potential for the attainment of predictive engine simulations in the future.

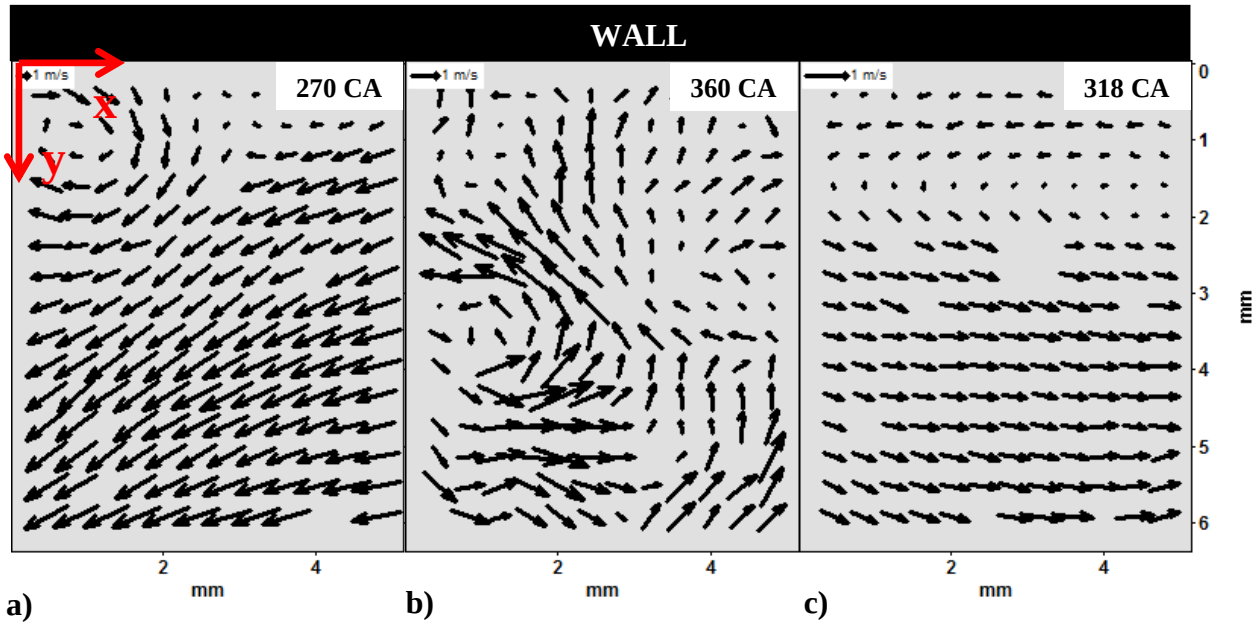

Figure 4-1 Three sample instantaneous vector fields from a motored test that demonstrate some various types of flows encountered in the near wall region of an internal combustion engine. (a) presents a large vortex interacting with the wall. (b) shows a flow field with flow directly impinging on the wall (at center). (c) Shows a narrow shear layer generated during a flow field reversal during the expansion stroke. These images are not from the same cycle. Only every 4th vector is shown in each direction.

Figure 4-1(c) depicts a narrow shear layer parallel to the wall. The flow closest to the wall moves in the negative *u* direction, while only a millimeter away the flow direction is in the opposite direction. This is reminiscent of the canonical pulsatile flow driven by an oscillating plate.

The sequence of a complicated flow reversal in the ensemble average is explained by Fig. 4-2. At the late-compression stroke (318 CA, Fig. 4-2(a)) the flow field is nearly uniformly flowing left in the negative $\langle u \rangle$ direction. As compression progresses the flow field begins to reverse its

wall-parallel direction. By 10 CA later (328 CA), a shear region forms pulling the lower left region of the flow downward, initiating counterclockwise rotation of the vectors. By 338 CA the flow has begun to split at y = 2 mm, with the flow farther from the wall reversing direction through counterclockwise rotations of the velocity vectors, while flow in the top left region and along the wall are now clearly flowing towards the wall as the results of some significant 3D structure of which only a 2D cutting plane is visible. The remaining process of the flow reversal occurs rather quickly in well under 10 CA. At 342 CA the core flow has finished reversing direction across the field of view and the top left corner of the near-wall flow is completing its clockwise rotation. By 346 CA the left half of the field of view has already finished reversing direction, and we see that by TDC the mean flow field has completely finished its reversal. It is also interesting to note that small-scale structures do exist in the ensemble average and in the flow reversal shown in Fig. 4-2.

While significant insights can be made from these high crank-angle resolution tests regarding flow development and movement of coherent structures of the flow, in fired tests they can also be used to visualize the high variability in flame propagation that exists in this engine. Figure 4-3 and Figure 4-4 present image sequences (a.1-c.1) at three consecutive crank angles, and their corresponding vector fields (a.2-c.2), for two cycles from the same test. These sequences depict the large cycle-to-cycle variability of flame propagation through the image plane in this engine. The sequence in Fig. 4-3(a.1) shows a flame front punching through the image plane 5 CA before TDC, and its subsequent outward propagation, which presents the highly 3D nature of the flame-front surface. Particles are visible in the unburned gas region around the periphery of the particle-less burned gas region at the center. Figure 4-3(a.2) shows the corresponding vector field and streamlines, where an algorithmic masking routine was utilized to make out the burned gas regions prior to vector calculation. In Fig. 4-3(a.2) the flame propagation does not appear to affect the generally upwards in-plane flow direction in this instance.

However for the sequence presented in Fig. 4-4, which shows a flame propagating generally from the lower left-hand corner of the field of view to the top-right corner, the flow at the flame surface in all realizations is in the direction of flame propagation, as the unburned gas is compressed due to the thermodynamic expansion occurring behind the flame front. It is important to note the one crank-angle degree difference between these sequences when comparing them. Not only do these sequences depict the variability of in-plane flame propagation, but the delay between them also

represents the variability of the flame propagation in the out-of-plane direction as well. The 3D nature of the burned region is again evident in this cycle, as in the bottom right of the image in Fig. 4-4(c.1) a peninsula of unburned gas is surrounded by burned gas regions indicative of the significant wrinkling of this turbulent flame.

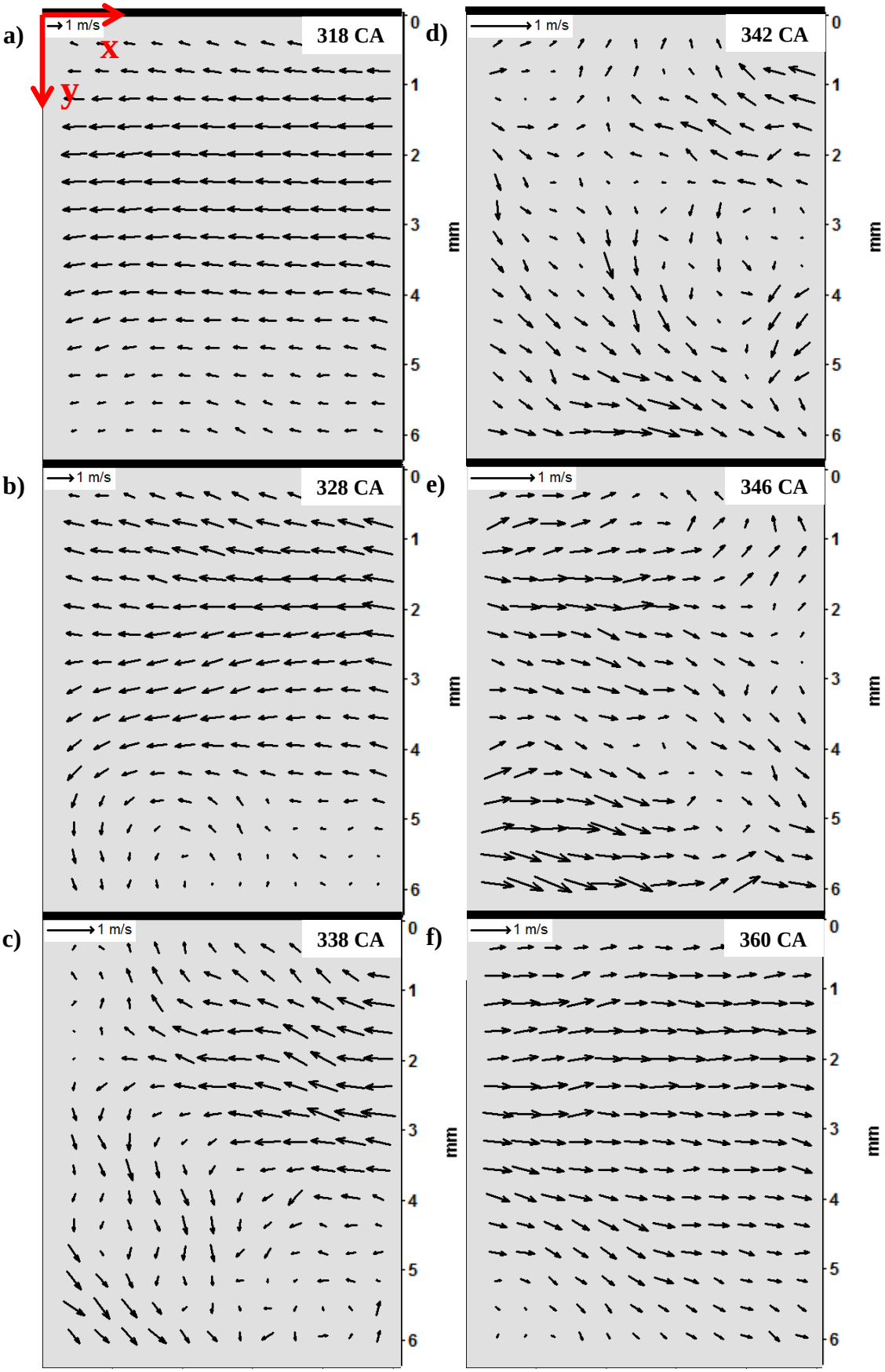

Figure 4-2 Ensemble average flow field series depicting flow reversal of the mean flow of a motored test.

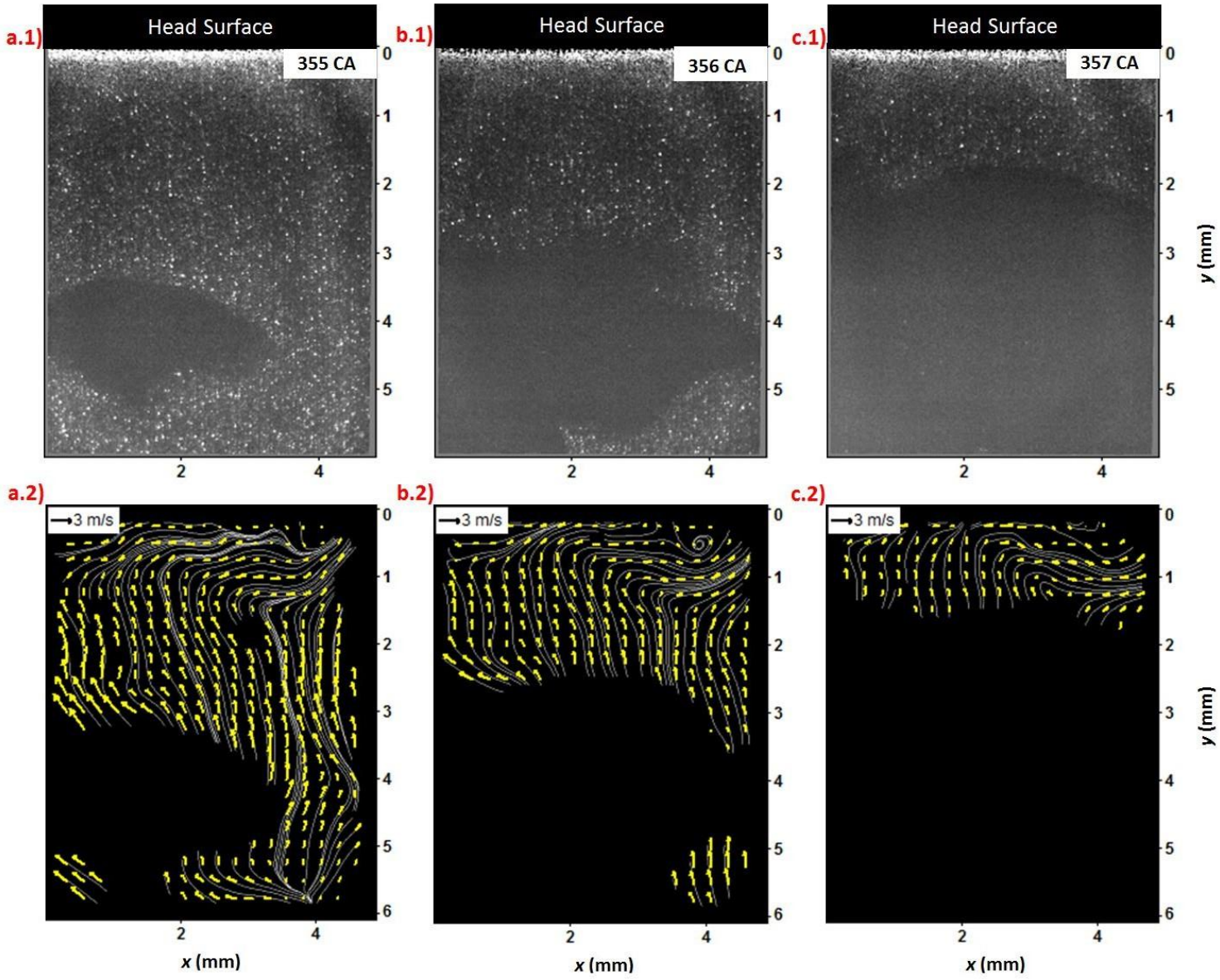

Figure 4-3 Flame propagation sequence images (x.1) and corresponding vector fields (x.2) near TDC depicting burned and unburned regions in field of view.

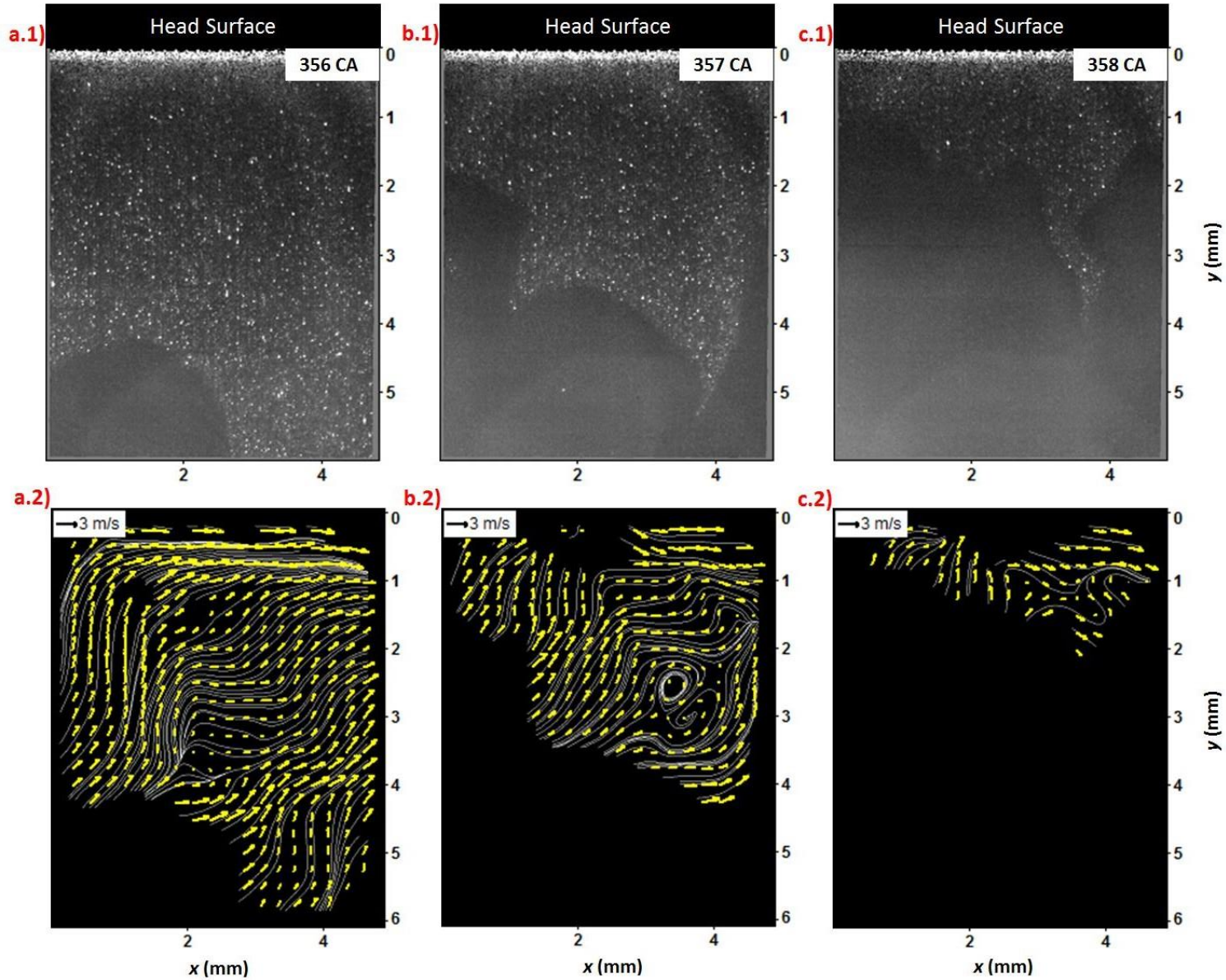

Figure 4-4 Flame propagation sequence images (x.1) and corresponding vector fields (x.2) near TDC depicting burned and unburned regions in field of view.

4.2 Head surface measurements

The analysis of near-wall region engine flows will continue with a discussion of the ensemble-averaged 500 rpm motored operating condition as presented in Fig. 4-5. Here the ensemble-average flow and ensemble standard deviation of the flow from cycle-to-cycle have been computed by sampling every cycle at fixed crank angles. While it would certainly be desirable to record for many more cycles than the 141 cycles recorded here in order to achieve a greater degree of statistical convergence of the results, this was unfortunately not possible due to rapid fouling of the quartz cylinder. Figure 4-5 presents the mean and standard deviation of both velocity components computed over this enlarged sample pool as a function of wall-normal distance *y*. The dashed vertical line at 5 mm marks the half-clearance height of the cylinder at TDC.

As the random uncertainty computed with the correlation statistics method (Neal, Sciacchitano et al. 2015, Sciacchitano, Neal et al. 2015, Wieneke 2015) falls out of averaging processes (Wilson and Smith 2013), only the true unknown systematic uncertainty, and the statistical precision uncertainty ($\sigma/\sqrt{n}$) contribute to the uncertainty of the mean profiles. As the true systematic uncertainty is unknown, only the statistical precision uncertainty of the measurements is shown on the mean here. The uncertainty on the standard deviation is computed as shown in (Wilson and Smith 2013) and takes into account both the random uncertainty of the individual velocity vectors as well as the statistical precision uncertainty. As can be seen in Fig. 4-5 (c) and (d), the uncertainties on the standard deviations are largely one sided. This is because both the actual flow fluctuations as well as fluctuations due to measurement uncertainty contribute to the standard deviation. Therefore the true standard deviation of the velocity field would be less than that calculated, as the latter also includes the contribution from fluctuations in the measurement system. Therefore, the calculated standard deviation is an overestimate of the flow-field fluctuation and the uncertainty bands should be, and are, one-sided.

The left column of Fig. 4-5 presents the first and second moments of the wall-parallel velocity component *u*, while the right column presents the same for the wall-normal component *v*. The requisite boundary conditions at the wall, namely no through flow and no slip, require both *u*, *v*, and their fluctuations to approach zero. These conditions are satisfactorily fulfilled.

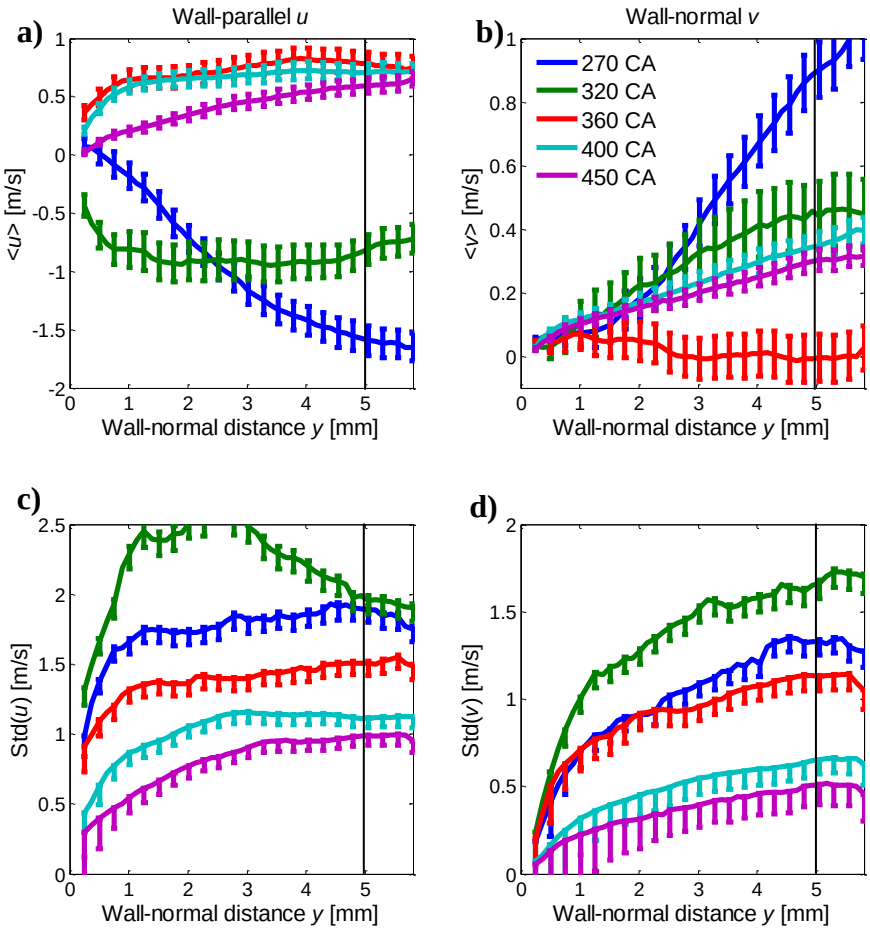

Figure 4-5 Representative ensemble mean and standard deviation profiles at the cylinder head with the engine motored at 500 rpm. Every other uncertainty band is shown.

Figure 4-5(a) presents the progression of the mean wall-parallel velocity component <*u*> through the imaged portion of the cycle: from mid compression stroke to mid-expansion stroke for a few select crank angles. The line at 5 mm is the mid-clearance point at TDC, and also 9% of the clearance at 270- and 450 CA. As can be seen the flow shows a negative <*u*> velocity, i.e. towards the left in the field of view. As the cycle progresses the dominant flow pattern reverses direction beginning from the core region until by TDC the entire field of view holds positive <*u*> velocities. As the expansion stroke develops the flow field typically becomes increasingly uniform, and lower in energy, as much of the turbulence generated by flow through the valve during the intake stroke has dissipated. The standard deviation profiles in Fig. 4-5(c) show how widely the flow field varies about the ensemble average from cycle to cycle. In fact, the standard deviation is greater than the

mean value for all crank angles shown! A reference back to Fig. 4-1 reveals a partial explanation: frequent interactions between core-flow turbulent structures and the near-wall region cause numerous interruptions to the near-wall flow, increasingly so as TDC is approached as these structures break down to more numerous and smaller length scales. However, as shown in (Reuss 2000) the undirected flow in the TCC engine is characterized by extreme amounts of large-scale cycle-to-cycle core-flow variability as viewed in the plane parallel to the head, that could cause shifts in the timing of the local mean flow reversal as TDC is approached. Additionally, large-scale mode-switching in the core flow has been identified in this engine due to a slight azimuthal rotation of a predominant large-scale structure, both from test-to-test and during a single 3000 cycle test (Abraham, Yang et al. 2015).

A similar result can be seen in Fig. 4-5 for the mean of the wall-normal velocity component $<v>$. As can readily be seen by comparing to the larger magnitude mean profiles in the left column, the flow is dominantly wall parallel, which is to be expected. Comparing the left and right columns of Fig. 4-5 it is important to note the subtle difference in the location where the core flow statistics start to roll off as the wall is approached. Comparing the two columns visually, it can be seen that the gradient at the wall is steeper for both the mean and standard deviation quantities for $<u>$ than for $<v>$. The standard deviation profiles of $<u>$ are slightly flatter than for $<v>$. These observations suggest the presence of the wall impacts the wall-normal component $<v>$ of the flow farther from the wall than for the wall-parallel component $<u>$.

Figure 4-6 compares near-wall velocity profiles at the head surface for all four engine operating conditions for which measurements were recorded. Profiles are presented at a constant crank angle late in the compression stroke 22 CAD prior to start of ignition. Both the wall-parallel component $<u>$ and the wall-normal component $<v>$ are normalized by mean piston speed $\overline{V_p}$ to facilitate comparison between engine speeds. The most remarkable observation from the figure is that the 500 rpm fired profile appears to be a mirror image of what might be expected from the other operating conditions. This will be explored in the following two figures. Apart from the 500 rpm fired profile, however, the other three profiles show reasonable agreement with decent scaling between engine speeds especially in the horizontal component $<u>$ presented in Fig. 4-6(a). The slightly poorer scaling between engine speeds in the motored tests seen in the $<v>$ component in Fig. 4-6(b) could indicate that in the near-wall region the wall-normal velocity scales superlinearly

with engine speed. The large hump in the standard deviation in Fig. 4-6(c) for the 500 rpm motored case is believed to be due to some variability in the timing of the flow field reversal (see Fig. 4-2) occurring around this crank angle.

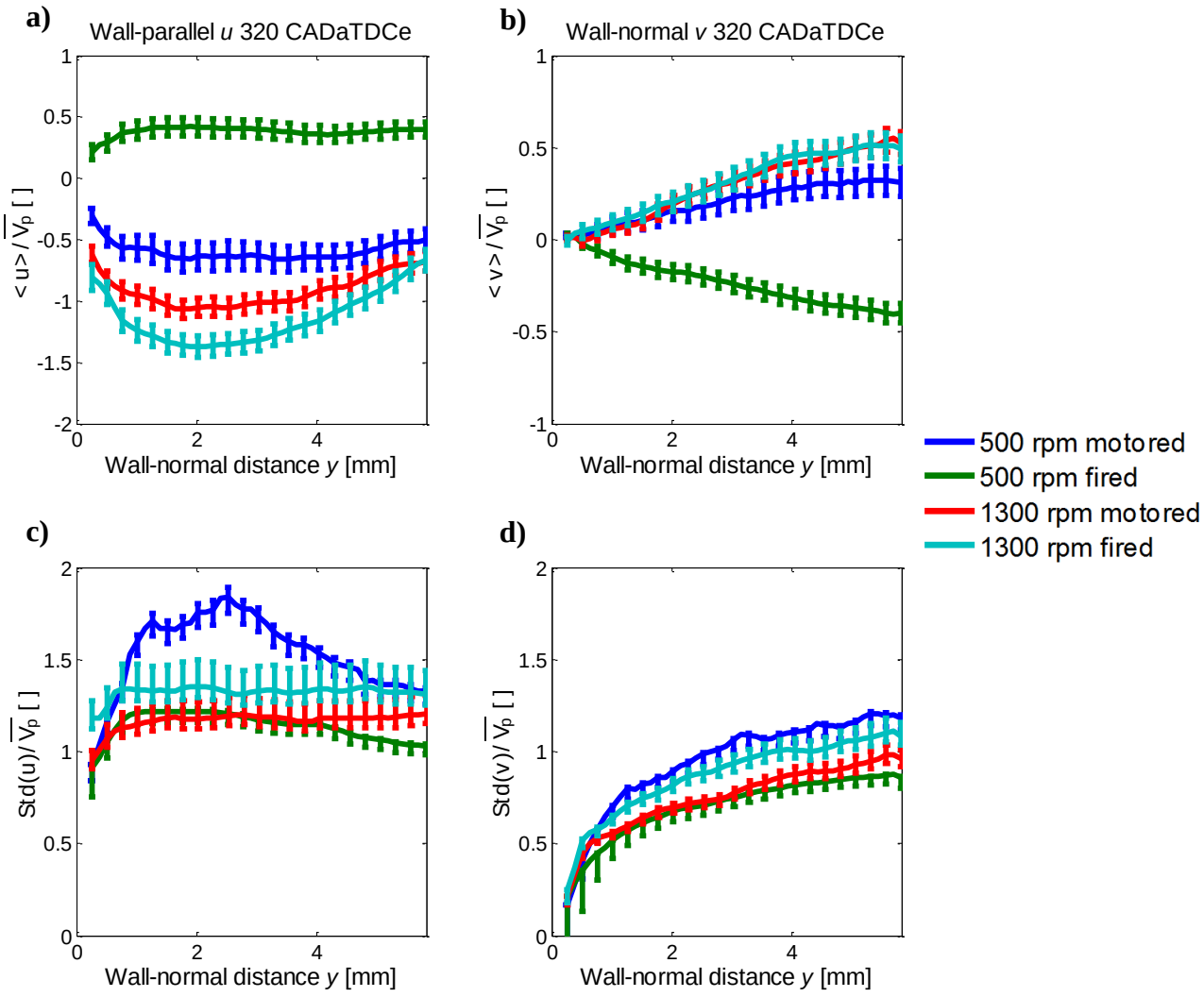

Figure 4-6 Average of all tests taken at head surface data for all four operating conditions.

The deviation of the average of the 500 rpm fired tests from what might be expected as seen above in Fig. 4-6 will be explored in Fig. 4-7 and Fig. 4-8. In these figures, the ensemble average of a single 500 rpm fired test, with the average of remaining tests at 500 rpm fired is compared. Figure 4-7 presents the wall-parallel <*u*> and wall-normal <*v*> velocity components as a function of crank angle for four wall-normal distances *y*. The vertical dashed black line marks the spark timing of the fired tests. Figure 4-7 shows the initial flow development of the motored and fired

tests are consistent during the intake stroke and early in the compression stroke. But a significant deviation develops in $\langle u \rangle$ in the average of remaining fired tests beginning at 210 CA. This deviation originiates in the core flow at about 210 CA and does not appear at y = 0.5 mm near the wall for some 50 CA later. As similar trend is visible in $\langle v \rangle$ where a deviation begins at y = 4- and 2 mm near 220 CA, while no deviation between the average of motored and fired tests is apparent in $\langle v \rangle$ until the onset of ignition at 342 CA, at which point $\langle v \rangle$ turns negative (towards the wall) consistent with compression of the unburned gas region by the approaching flame front.

However, the single fired test ensemble average shown in red in Fig. 4-7 looks remarkably similar to the average of tests at the motored condition. While this is the only test of the eight fired tests recorded to display this 'motored-like' behavior in both $\langle u \rangle$ and $\langle v \rangle$ it precludes the conclusion that the deviation between the average of motored and fired tests seen in green and blue in Fig. 4-6 is due to the presence of combustion. Additionally, all three of the fired tests recorded every 1 CAD as indicated in Table 1 above exhibit this 'motored-like' behavior in $\langle u \rangle$ but they do not exhibit this behavior in $\langle v \rangle$, where they instead show a behavior consistent with the remaining fired tests. None of the motored tests collected exhibit the characteristics of the remaining fired tests.

A definitive explanation for this behavior in the 500 rpm fired tests is not apparent. The routine pressure data recorded by the TCC-III engine systems shows no significant difference in engine operation for these tests. It is unlikely an explanation for this flow behavior exists in the small planar field of view where these measurements were recorded, given the highly three-dimensional nature of the core-flow structures that drive the in-cylinder flow. Either larger field of view three-dimensional measurements or simulations capturing this phenomenon would likely be required to resolve this open question. However, given the significant changes in planar flow field structures seen in motored operation at 800 rpm due only to a few degree azimuthal rotation of a large scale structure (Abraham, Yang et al. 2015), as determined by motored LES, it is most likely that a similar phenomenon of a small shift of a large structure is responsible for the inconsistent characteristics discussed here.

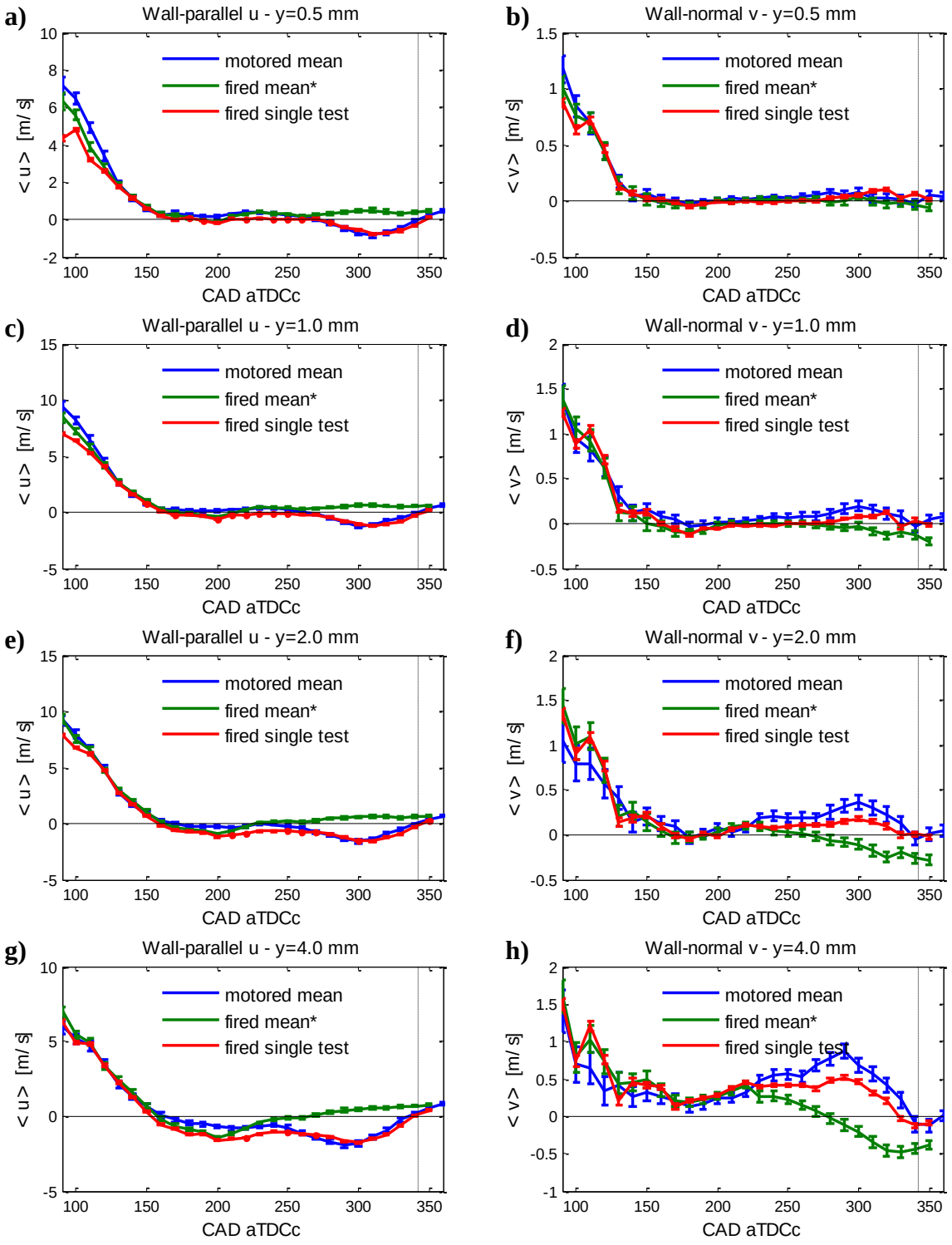

Figure 4-7 <u> and <v> velocity components as a function of crank angle for four different wall-normal distances at 500 rpm comparing flow development between the average of motored tests, a single fired test, and the average of the remaining fired tests.

Other interesting observations visible in Fig. 4-7 are that the flow velocity only decreases slightly in magnitude as the point of interest is moved from 4-, 2-, 1-, and 0.5 mm away from the wall. A flow reversal originating in the core flow is evident during the late intake stroke where the wall-parallel flow $\langle u \rangle$ reverses direction (crosses $\langle u \rangle = 0$) first at $y = 4$ mm at approximately 155 CAD, then at 160-, 170-, and lastly 180 CAD, for 2-, 1-, and 0.5 mm respectively. The discrepancy between the single fired test and the remaining data in Fig. 4-7 in the intake stroke (e.g. 100 CAD), though appears significant, is not notable as this is within the typical range of variability of single tests during this highly energetic part of the cycle.

Figure 4-8 is nearly the same as Fig. 4-6, except the average of 500 rpm fired tests has been replaced by the single 'motored-like' fired test presented in Fig. 4-8. As can be seen in the figure the single fired test matches the average of motored tests quite well, excepting the standard deviation on the *u* component which is somewhat higher as the wall is approached.

Figure 4-9 presents the wall-parallel $\langle u \rangle$ and wall-normal $\langle v \rangle$ velocity components as a function of crank angle for four different distances from the wall for the average of all tests at each condition measurements were taken. The dashed black line marks the spark timing of the fired tests. Here the crank angles over the entire cycle are shown, which allows for a visual representation of the crank angle ranges where PIV measurements could not be completed due to 1) particle pair loses due to high out-of-plane velocities, 2) the limited velocity dynamic range given the magnification and minimum interframe exposure period of the camera, and 3) absense of sufficient seed in residual gas during early intake stroke under fired conditions. As was seen with Fig. 4-7, the wall-normal flow on the right decreases in magnitude as the point of interest is moved from 4-, 2-, 1-, and 0.5 mm away from the wall. However, the wall-parallel flow actually reaches its peak velocity at 1-2 mm from the wall, not at the furthest wall distance as would be expected in traditional boundary layer theory. Also visible in Fig. 4-9 are the large fluctuations in the velocity when the valves are open as large high-energy structures are generated and penetrate the field of view.

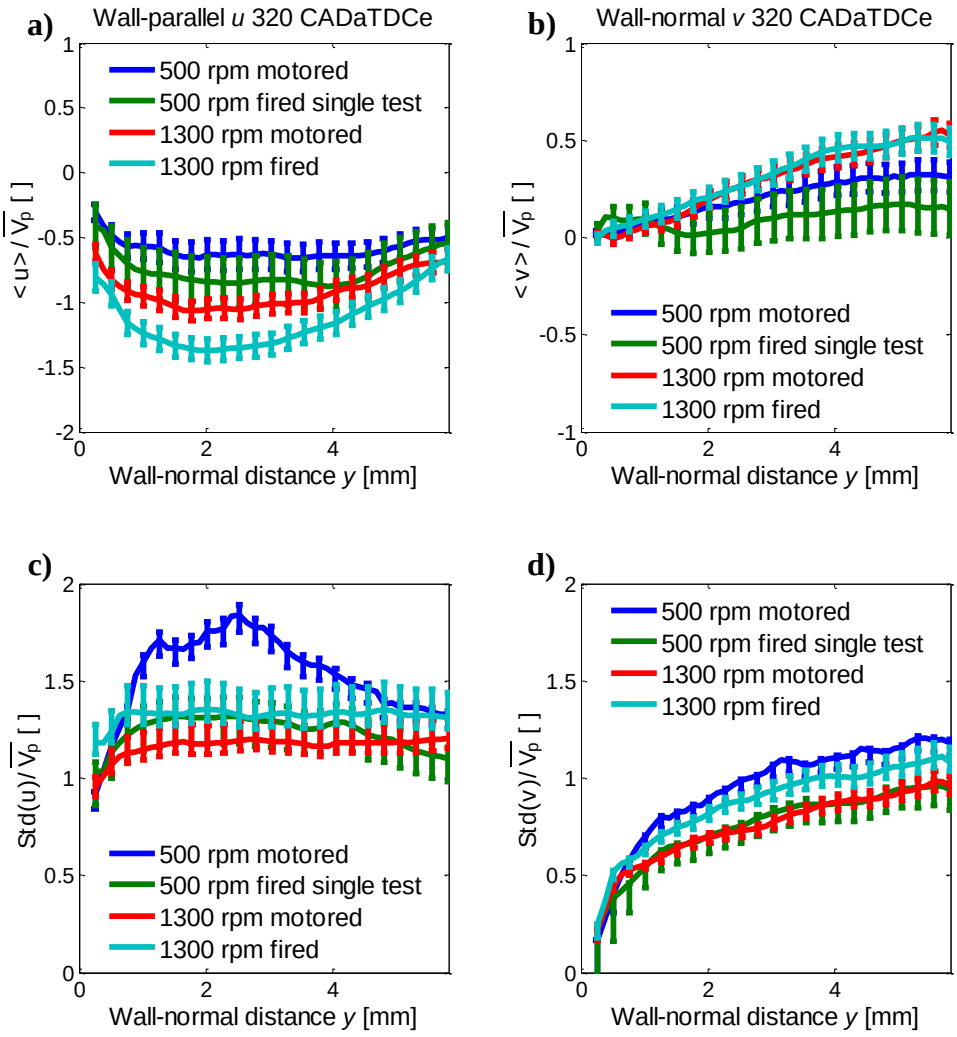

Figure 4-8 Comparison of four operating conditions for which measurements were taken at the head, but depicting the ensemble average of a single test at 500 rpm fired instead of the average of all tests for that condition. Compare to Fig. 4-6.

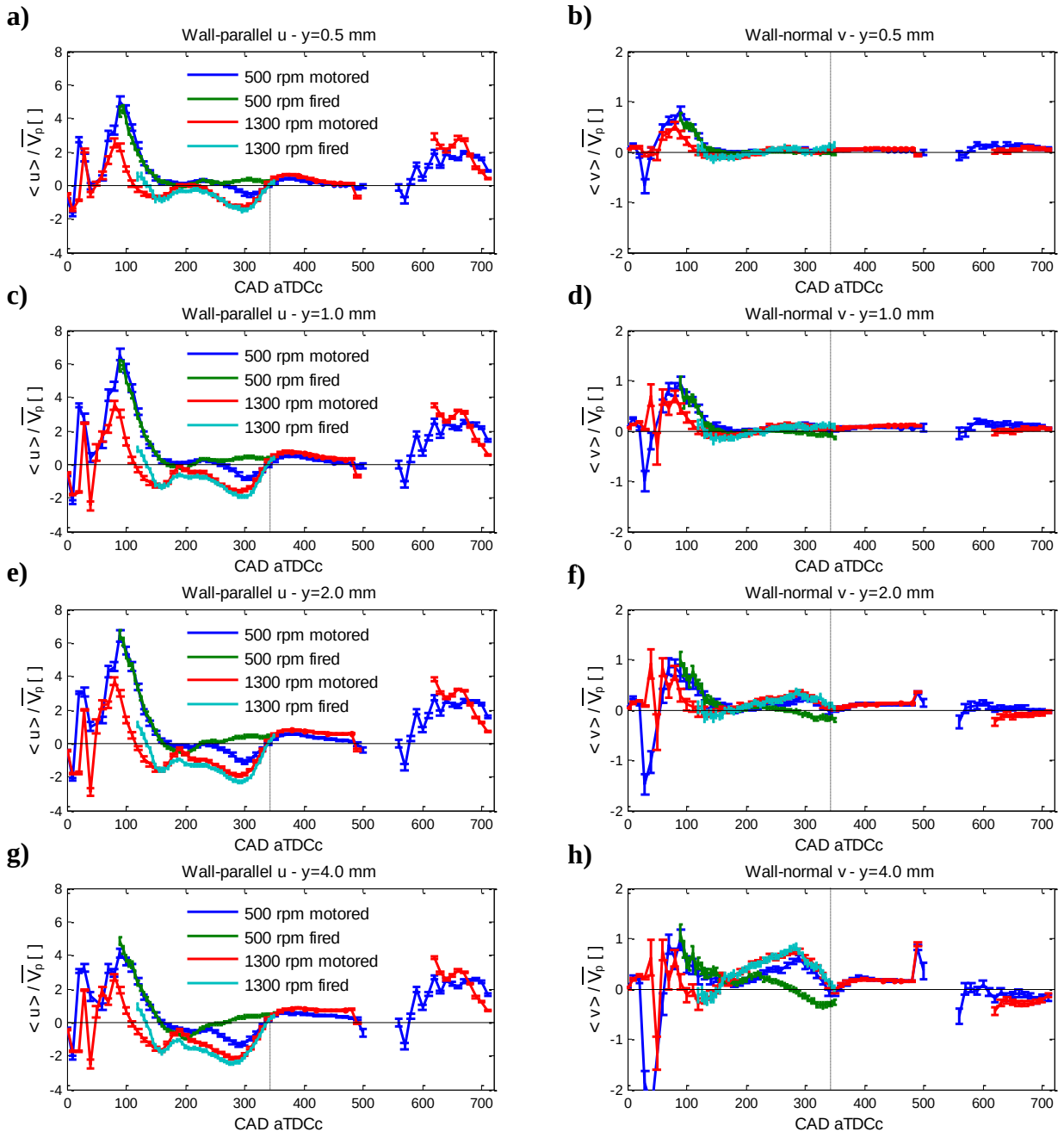

Figure 4-9 <u> and <v> velocity components as a function of crank angle for four different wall-normal distances for motored and fired tests at each condition. Average computed across all cycles of all tests at each condition.

4.3 Piston surface measurements

Now that the near-wall region flow at the head surface has generally been introduced, the flow on the piston surface will be examined. Figure 4-10 compares the head and piston surface flows at several selected crank angles for engine operation at 500 rpm. All data represents the average of all available tests at each condition and measurement location, including an averaging step in the wall-parallel direction to increase the sample size. Figure 4-10 (a) and (b) present velocity profiles on the piston surface at 500 rpm motored. Figure 4-10 (c) and (d) present the same but under fired operation. No measurements are reported following TDC for the fired condition as the seed particles have been consumed by the flame. Figure 4-10 (e) and (f) present velocity profiles on the head surface at 500 rpm motored for similar crank angles as presented in (a) through (d). As a reminder, throughout this dissertation a local coordinate system fixed to the investigated surface has been used. In all subfigures (a) through (f) the y-axis is normal to the surface extending into the measurement domain. For convenience, the *x*-axis has been aligned in the same direction at both surfaces, that is along the measurement plane towards the exhaust-valve side of the engine.

The measurements presented on the piston surface are provided relative to instantaneous piston speed to facilitate clear application of boundary conditions at the surface (no slip and no through-flow). However, as can be seen in Fig. 4-10 (b) and (d) for the test average velocity component <v>, the profiles tend toward zero only until y = 0.5 mm at which point the profiles make a marked shift towards flow into the surface (negative v), in a clear violation of boundary conditions. This is an artifact of the PIV process encountered as well in preliminary experiments at the head surface. It is believed this artifact is largely caused by differences in scattering intensity of the laser pulses between PIV image frames. This explains why the effect is more severe for the fired condition shown in Fig. 4-10(d) where the seed oil soot on the piston surface drastically increases the amount of laser light scattered at the surface. For measurements taken at the head location, this issue was largely resolved by the choice of PIV calculation parameters presented in the experimental section above. It is not clear why this effect is so much more pronounced on the piston surface but two possible explanations are 1) the movement of the piston surface affecting the distribution of scattered light captured by the camera sensor, and 2)

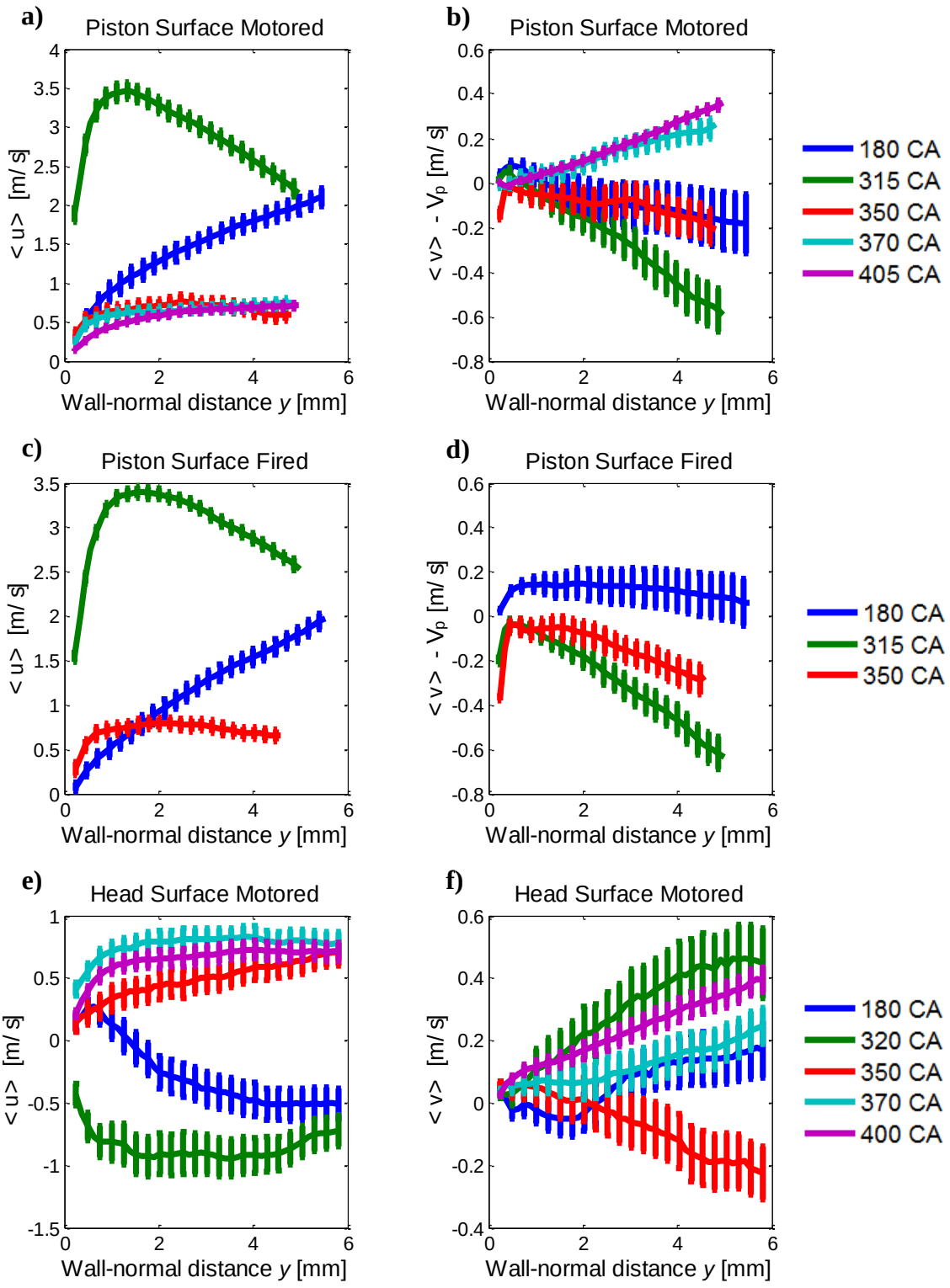

Figure 4-10 Comparison between ensemble mean near-wall profiles on the piston and head surfaces at 500 rpm motored condition. Wall-normal velocities at the piston surface are shown relative to instantaneous piston speed.

the use of a horizontal imaging axis as shown in Fig. 3-8 for imaging at the piston surface rather than the inclined axis of Fig. 3-10 used for imaging at the head surface.

The discussion on near-wall region flow development through the cycle on the piston surface will be continued with Fig. 4-10(b). Flow towards the surface is negative <v>, and flow away from the surface positive <v>. At 180 CA (BDCi) the piston has been pulling the fresh charge into the cylinder and as the piston has come to rest the flow continues to move towards the piston as would intuitively be expected due to momentum of the flow. By 315 CA late in the compression stroke the flow also presents towards the piston, again as would be expected given the piston is compressing the flow up towards the head. Close to TDC, at 350 CA, the flow has lost much of its energy but still shows a velocity towards the piston as the piston approaches TDC. In the expansion stroke at 370- and 405 CA the flow moves away from the piston surface as it expands in a low momentum state (note also the comparatively low velocities at 350-, 370-, and 405 CA in Fig. 4-10(a) compared to 180- and 315 CA). A similar flow development can be seen in Fig. 4-10(d) for the fired case, though higher wall-normal velocities are present at BDCi (180 CA). An explanation for this observation is not apparent.

For the wall-parallel velocity component <u>, Figure 4-10 (a) and (c) show similar profiles of the wall-parallel component between the motored and fired conditions. At 180 CA (BDCi) the high energy flow developed during the intake stroke creates a somewhat typically appearing profile commonly found in boundary layer analysis in Fig. 4-10(a). Figure 4-10(b) shows a similar profile at this point in the cycle, though somewhat less energetic and also more linear in form. Again, near TDC and into the expansion stroke (350-, 370-, and 405 CA) fairly canonical appearing flows appear in the wall-parallel direction <u>, with decreasing energy as the cycle progresses. What is most notable about these figures is the appearance of a strong wall jet appearing near y = 1 mm at 315 CA late into the compression stroke (green line). The presence of this wall jet, combined with the observation of the head flow moving in the opposite direction at a similar crank angle, indicates the possible presence of a tumble-like motion within the cylinder. The TCC engine has a single undirected intake valve and is not characterized by a strong tumble motion, however from this data it appears a strong coherent structure exists in the tumble plane at this crank angle as the piston compresses the flow upwards. It should also be noticed that at 180- and 320 CA, the velocities at the head and piston surfaces are going in opposite direction. On the head surface the flow is away

from the exhaust-valve side of the engine and away from the surface, while on the piston surface the flow is towards the exhaust-valve side of the engine and towards the surface. This suggests a large-scale structure exists at this portion of the cycle as well.

Figure 4-11 presents a comparison of the near-wall flow field development over the cycle at four distances from the wall at 500 rpm. The data presented at the head surface is the same as shown in Section 4.2. The presented data on the piston surface is relative to the instantaneous piston speed. As with the fired measurements taken at the head location, measurements on the piston surface were limited to 90-360 CA where there were sufficient seed particles. In all instances, no significant differences between motored and fired operation are discernible on the piston surface. For $y \leq \sim 1$ mm the velocities near the head and pistons surfaces match quite well (Fig. 4-11 (a)-(d)) except during the late compression stroke (315-323 CA) where the flow on the piston surface is significantly higher and in the opposite direction than at the head location under motored operation (and the single 'motored-like' fired tests discussed regarding Figs. 4-7 and 4-8). This again appears to indicate a large-scale structure present at this portion of the cycle. For $y > 1$ mm, increasing wall-parallel <u> velocities are observed at BDCi with increasing wall-normal distance. While these significant differences can be observed in the velocities magnitudes in the <u> direction between the head and piston surfaces, the velocity magnitude in the <v> direction shows much less difference between the two measurement locations.

A comparison between the motored and fired flows at 500 rpm and the motored flows at 1300 rpm late in the compression stroke is presented in Fig. 4-12. Here again the velocities and standard deviation quantities are normalized by mean piston speed, and the $\langle v \rangle$ velocity component is reported relative to instantaneous piston speed. As can be seen in Fig. 4-12(a) a strong wall jet in the wall-parallel component $\langle u \rangle$ is present along the piston surface in all three operating conditions. The presence of a wall jet on the piston surface during the compression stroke is not surprising as the flow characteristics are somewhat analogous to impinging jet flows, as the piston rises to compress the trapped gases. Here, what is seen can be thought of as the wall-jet region observed in impinging jet flows. The wall layer thickness, visible here as the location of maximum velocity in the field of view, is markedly thinner at 1300 rpm motored than

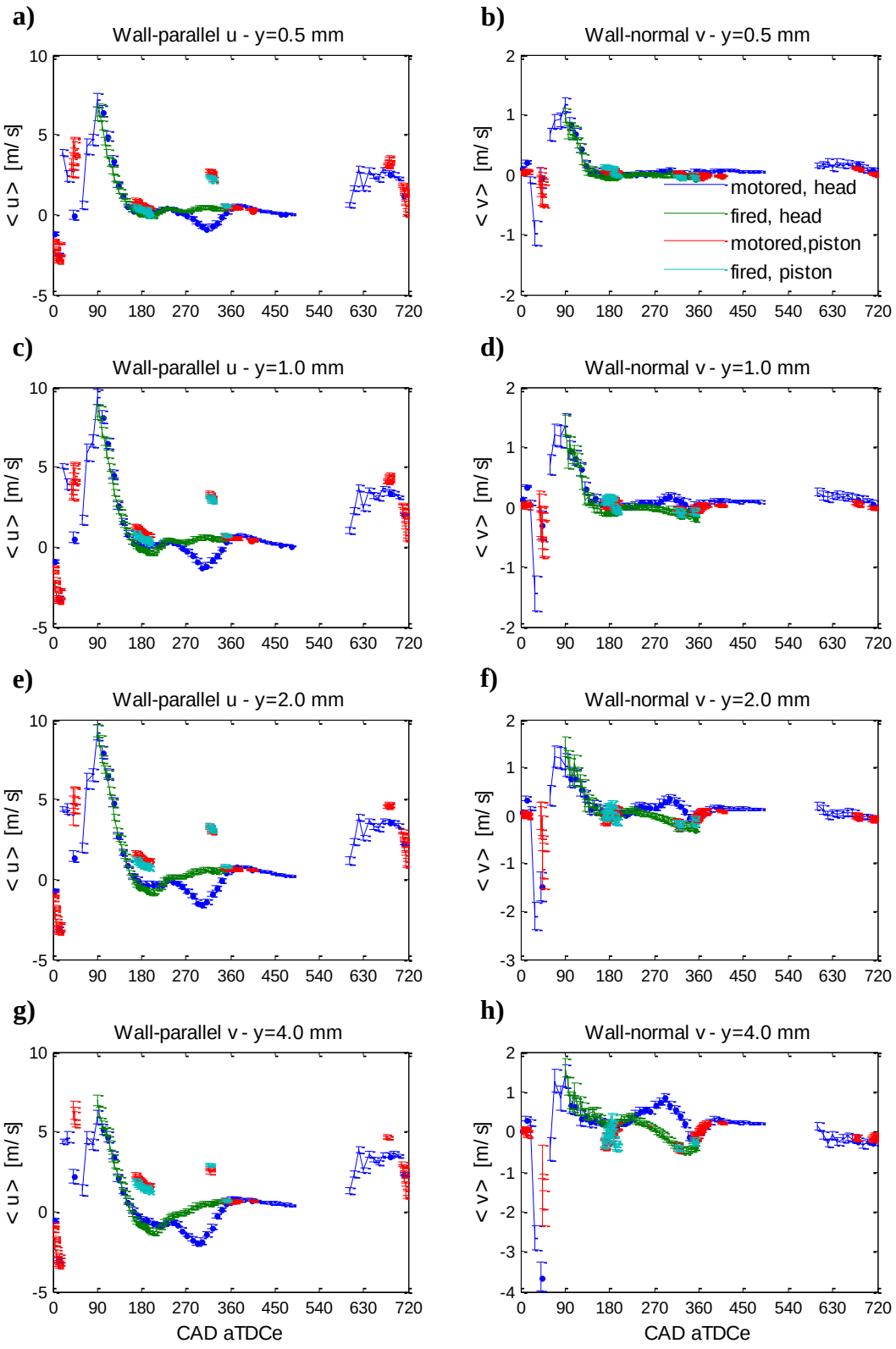

Figure 4-11 Comparison between flow development through the cycle on the piston and head surfaces at 500 rpm. <v> component on the piston surface is reported relative to instantaneous piston speed.

the 500 rpm motored condition, which would be expected based on fundamental boundary layer physics due to the 2.6 times greater piston velocity driving the flow. The wall layer thickness at 500 rpm fired operation is also somewhat thicker than that at 500 rpm motored, likely due to the increased viscosity of the gases due in part to the higher wall temperature on the piston surface during fired operation. The piston surface temperature could not be measured as part of these experiments, but surface temperature measurements on the head surface by the heat-transfer probe showed more than a 20 °C increase during fired operation at 500 rpm. Given the piston surface is quartz at the PIV measurement location, an even greater difference in wall temperature between motored and fired operation would be expected due to the near-adiabatic properties of the quartz material (Steeper and Stevens 2000).

Figure 4-12(b) shows the wall-normal velocity component $\langle v \rangle$ for the same crank angle and operating conditions. The scaling by mean piston speed again performs poorly in this case, as was seen regarding Fig. 4-8 above, and could indicate a superlinear scaling of the wall-normal velocity component $\langle v \rangle$ with engine speed. As also seen in Figs. 4-6 and 4-8, a marked difference in the standard deviation profiles presented in Fig. 4-12 (c) and (d) of the wall-parallel component u and the wall-normal component v is discernible. The substantially steeper gradient at the wall and relatively constant value for $y > 0.5$ mm for the u component, compared to the significantly shallower gradient at the wall and steadily increasing value of the v component indicates the presence of the wall has a significantly greater effect on the v component farther from the wall than the u component. That is to say the wall-effect distance is significantly greater in the wall-normal direction than the wall-parallel direction.

Figure 4-13 compares the flow development on the piston and head surfaces over the course of the engine cycle at 1300 rpm for four wall-normal distances. The wall-normal component $\langle v \rangle$ is reported relative to instantaneous piston velocity for measurements recorded at the piston surface. As seen previously in Fig. 4-9 the motored and fired trends match well for the data taken at the head surface. Unfortunately fired measurements on the piston surface were only able to be taken near TDCc at 1300 rpm, with only one data point shown that closely matches the

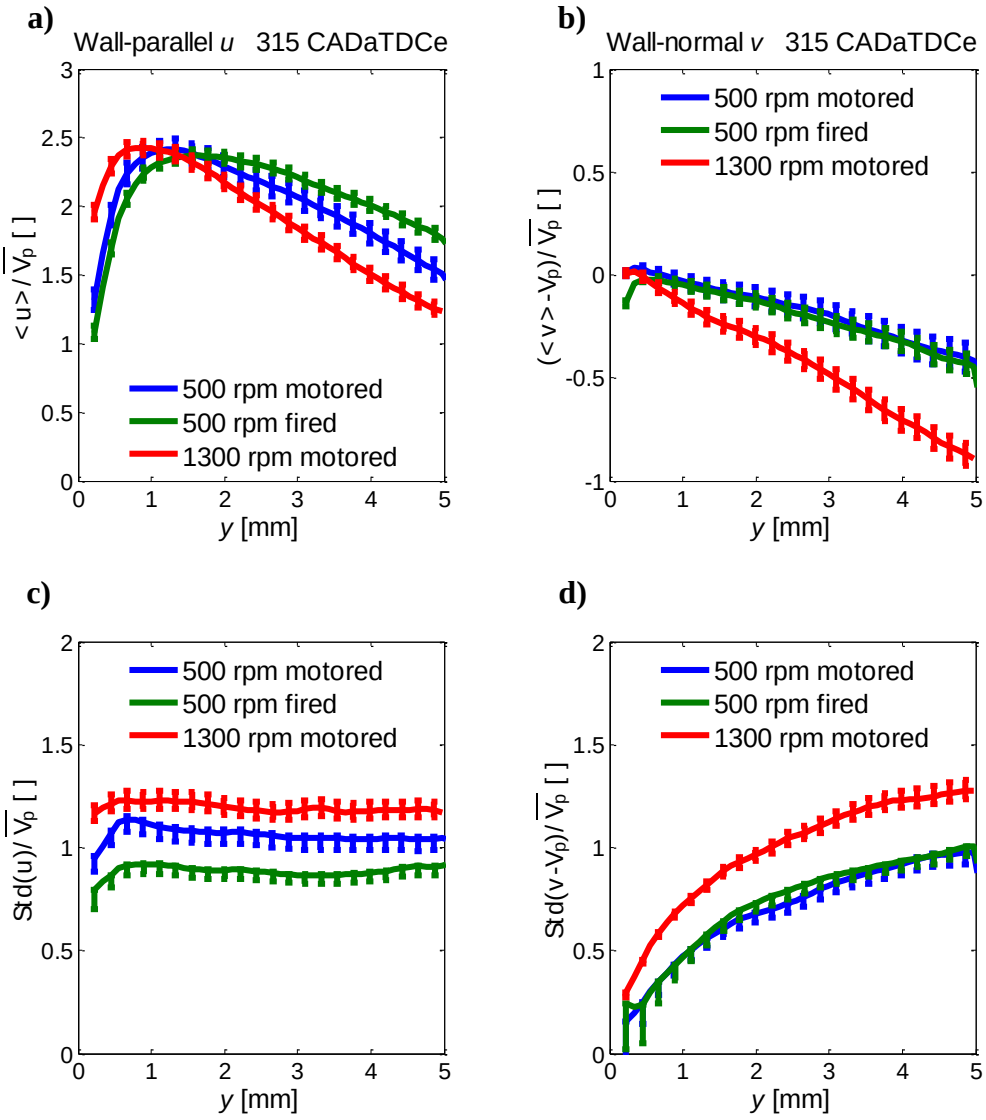

Figure 4-12 Comparison of near-wall region profiles at piston surface at 315 CADaTDCe. All quantities are normalized by mean piston speed, and the wall-normal component v is reported relative to instantaneous piston speed.

measured value under motored conditions at the same measurement location. When the equivalent representation was made for the data measured at 500 rpm in Fig. 4-11 it was observed that the velocity magnitudes were similar between the measurement locations. The same cannot be said here where significantly higher velocities were measured on the piston surface at BDCi, especially in the wall-parallel direction <*u*>. From the left column in Fig. 4-13 it might appear at first glance that significantly higher velocities were recorded close to the piston surface approaching BDCi (*i.e.* y = 0.5 mm at 150 CA in motored piston data) than at greater wall distances, however the

vertical dashed line at 165 CA is placed to dissuade the reader from this conclusion. As twice per cycle the piston uncovers and covers the field of view only a small amount of the flow field is visibly by 150 CA when the camera is set to image near BDC. At 150 CA less than 1 mm of the flow is available for PIV measurements, and no measurements were computed at this crank angle for wall normal distances $y > 0.5$ mm (Fig. 4-13(c)-(h)). As the piston continues to fall more field of view is exposed, and therefore access to measure velocities at greater wall distances until by 165 CA measurements were computed to $y = 4$ mm. Inspection of the intersection of the dashed line at 165 CA with the motored piston (red) profile shows that the wall-parallel component $\langle u \rangle$ is fairly consistent across the field of view. Also note in Fig. 4-13 that the velocity magnitudes at the head and piston surfaces are fairly similar near TDC, particularly in the wall-parallel direction $\langle u \rangle$.

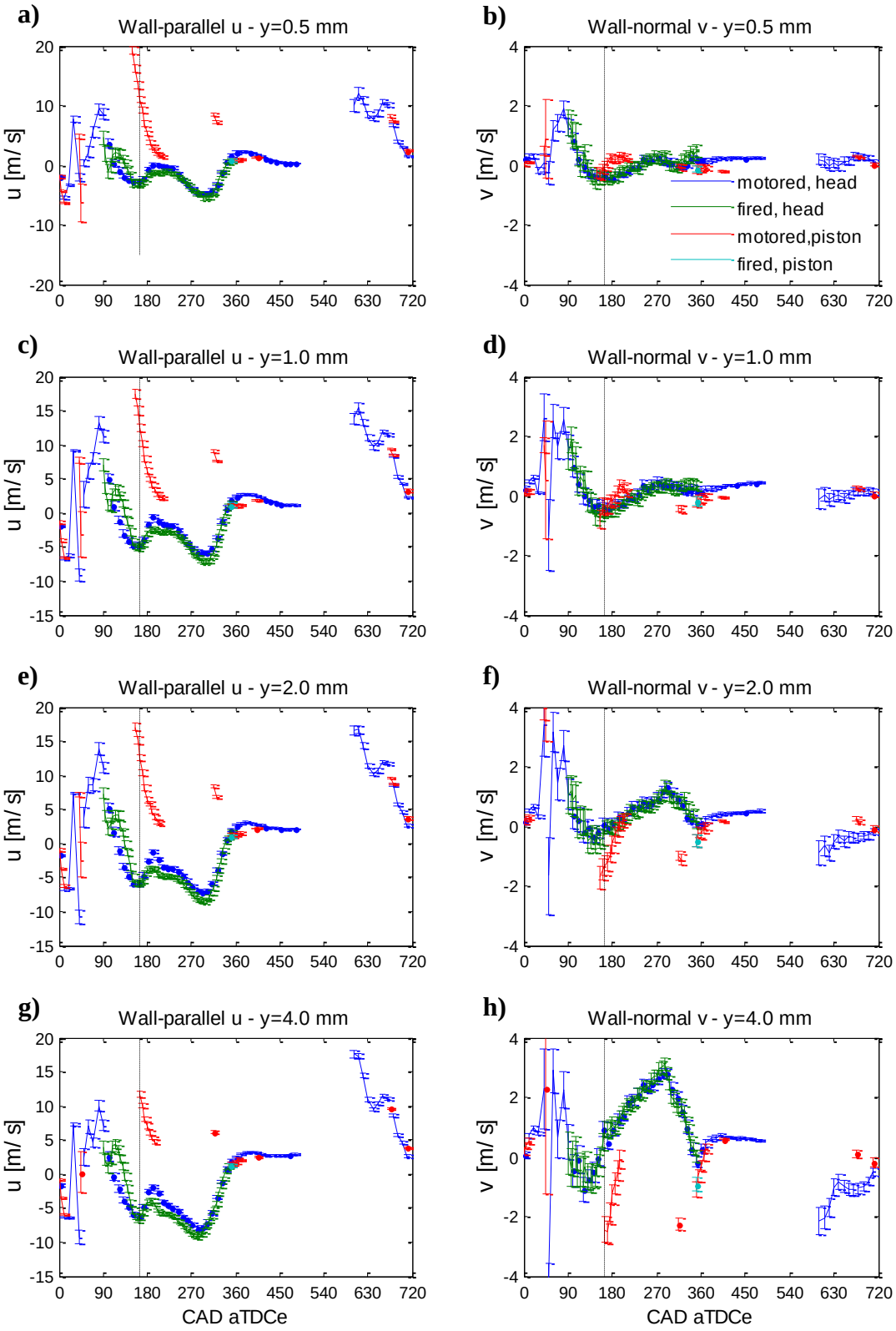

Figure 4-13 Comparison between flow development through the cycle on the piston and head surfaces at 1300 rpm. <v> component on the piston surface is reported relative to instantaneous piston speed.

4.4 Head surface temperature and heat-flux measurements

Heat flux and surface temperature measurements were recorded at the head surface as shown in Fig. 3-15. Figure 4-14(a) presents the ensemble average surface temperature measurements for each of the four operating conditions presented in this work. The ensemble average calculated heat flux is presented below in Fig. 4-14(b). The vertical dashed lines indicate spark timing. As can be seen in Fig. 4-14 there is a significant delay in the thermal response of the wall to the combustion event, with the point of peak heat flux closely matching the calculated location of 90 percent mass-fraction burned (CA90) which are marked by the vertical solid lines. The CA90 at 500 rpm was 373 CA and slightly later at 1300 rpm at 379 CA. Figure 4-14(a) shows that the peak surface temperature is reached a few degrees after the location of peak heat-flux. The negative heat flux computed during the intake and early compression strokes is due to the wall being cooled by the fresh charge. These heat flux and surface temperature measurements were recorded for all tests in the PIV database set forth in Table 3-2 and Table 3-3 except for the 500 rpm motored tests at the cylinder head location.

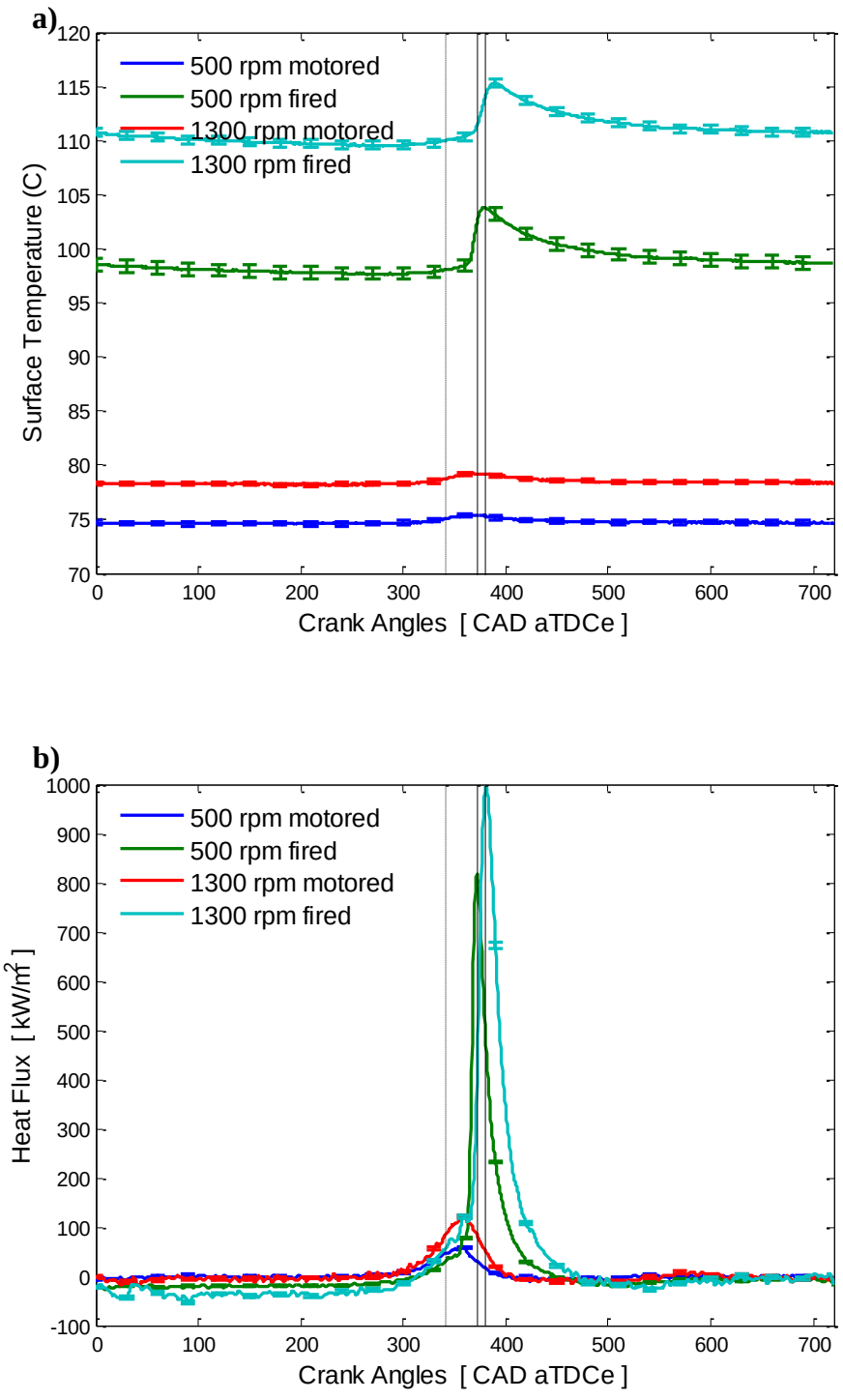

Figure 4-14 Surface temperature measurements and calculated heat flux as measured at location identified in Fig. 3-15. Uncertainty bands represent statistical uncertainty and every 60th band is shown. Dashed vertical line indicates spark timing. Solid vertical lines indicate location of 90% mass-fraction burned (CA90). The CA90 for 1300 rpm is later in the cycle.

Chapter 5
Discussion

5.1 Comparison to impinging jets

As discussed in Chapter 4 there are elements of in-cylinder near-wall region flows that resemble impinging jet flows. Recall Fig. 4-1(c) presented an individual vector field depicting direct wall-normal flow against the engine head, which would appear to have similarities with impinging jets and is not uncommonly seen in individual vector fields. A sample flow-field representing an impinging-jet-like flow on the piston surface is presented in Fig. 5-1 where every other vector is shown. Six columns of vectors (only three of which are shown because every-other vector is hidden to improve visibility) located at what appears to be the center of the 'jet' were averaged in the wall-parallel x direction and compared to the plane impinging jet correlation presented in Equation 2-10 in Section 2.4.

The coefficient formed after solving Equation 2-10 for U_C (i.e. $C = 5.5\ U_0\sqrt{e}$) was taken as 227 m/s to match the magnitude of the correlation profile to that of the experimental data to facilitate comparison of profile shapes. H was taken as 1/3 of the instantaneous cylinder height. As can be seen in Fig. 5-2 below the correlation model might adequately match the experimental profile for this instantaneous flow field. However, the fact that this flow field was selected due to the presence of wall-normal flow towards the wall it is not particularly surprising that the profile shape approaches that of the axial velocity of the impinging jet. The fact that these flows do not occur with sufficient frequency to be present in the ensemble average limits the utility of further analysis between heat transfer correlations at the impingement zone of impinging jets and in-cylinder surfaces.

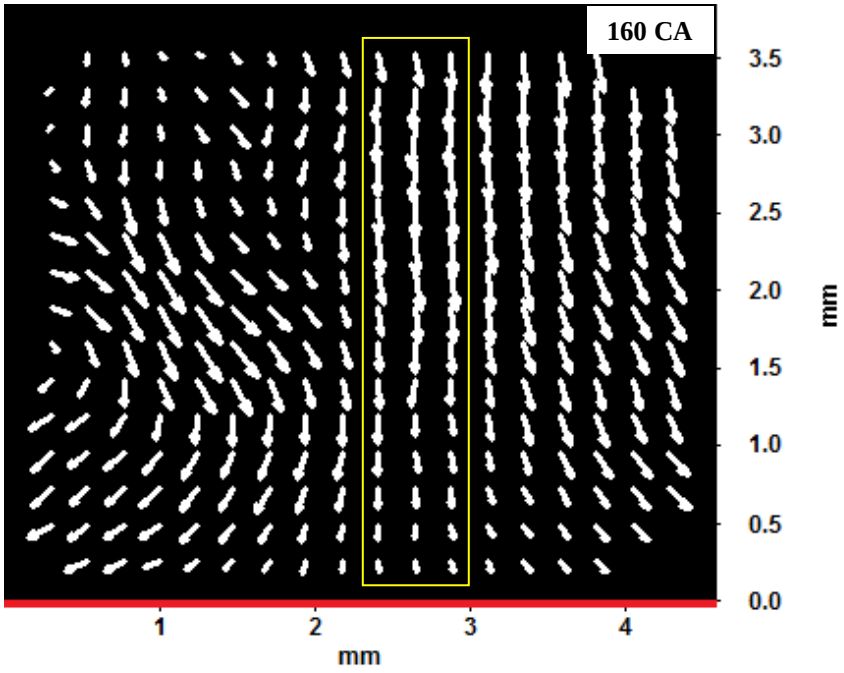

Figure 5-1 Sample flow field on the piston surface showing impinging-jet-like wall-normal flow towards the end of the intake stroke. Every other vector is shown.

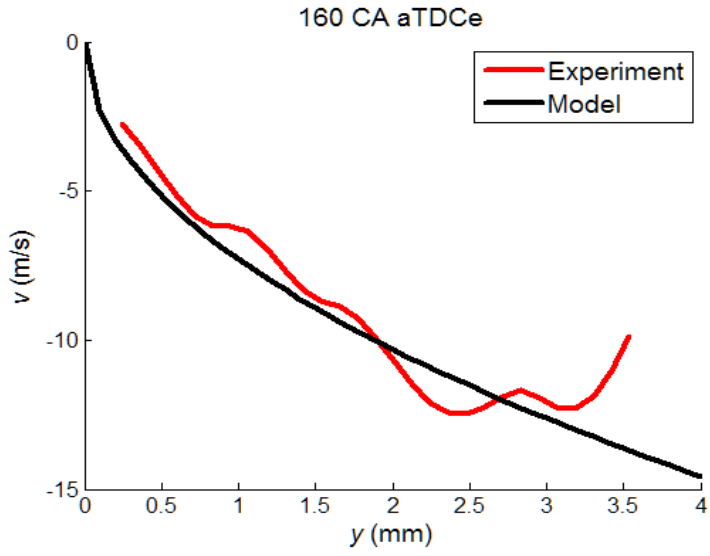

Figure 5-2 Comparison between experiment and numerical model of (Beltaos and Rajaratnam 1973) of Equation 2-10. Experimental data is 1300 rpm on piston surface averaged in the wall-parallel *x* direction as shown in Fig. 5-1.

5.2 Convergence of statistics

Much of the results presented in this work have been in the form of the mean and standard deviation quantity of the measured flow fields. The quality of any statistical analysis is largely dependent upon the sample size in light of the shape and spread of the sample data. This section will investigate the statistical convergence of the 1st and 2nd moments of the measurement fields presented in this work. The dataset collected at the cylinder head surface with the engine motored at 500 rpm will be used as the exemplary data for this discussion. This test condition has been chosen for this discussion as it contains the fewest measured cycles.

Figure 5-3 presents the development of the mean of each velocity component as additional cycles are added to the sample pool over which the averaging process is computed. As can be seen in Fig. 5-3 the mean for the representative crank angles shown after 90 CA converge (reach a steady state) by the time the entire sample pool is included in the averaging process. 90 CA was included as an exemplary crank angle as the intake stroke is characterized by large variations of highly-energetic flow, and as can be seen convergence of u does not appear to be obtained within the full dataset especially for closer wall-normal distances.

Figure 5-4 introduces the development of the standard deviation of the ensemble velocity components as additional cycles are included in the pool over which the statistic is computed. Similarly to Fig. 5-3, the standard deviation converges for the crank angles presented after 90 CA by the time all measured cycles are included in the computation pool. The standard deviation of the velocity components at 90 CA do not appear to converge within the number of cycles measured in the dataset.

The attainable statistical precision uncertainty ($\sigma/\sqrt{n}$) for a given sample pool size can be read from Fig. 5-5, which shows that for all crank angles after 90 CA low uncertainties on the mean are computed with a sample size larger than 200 cycles.

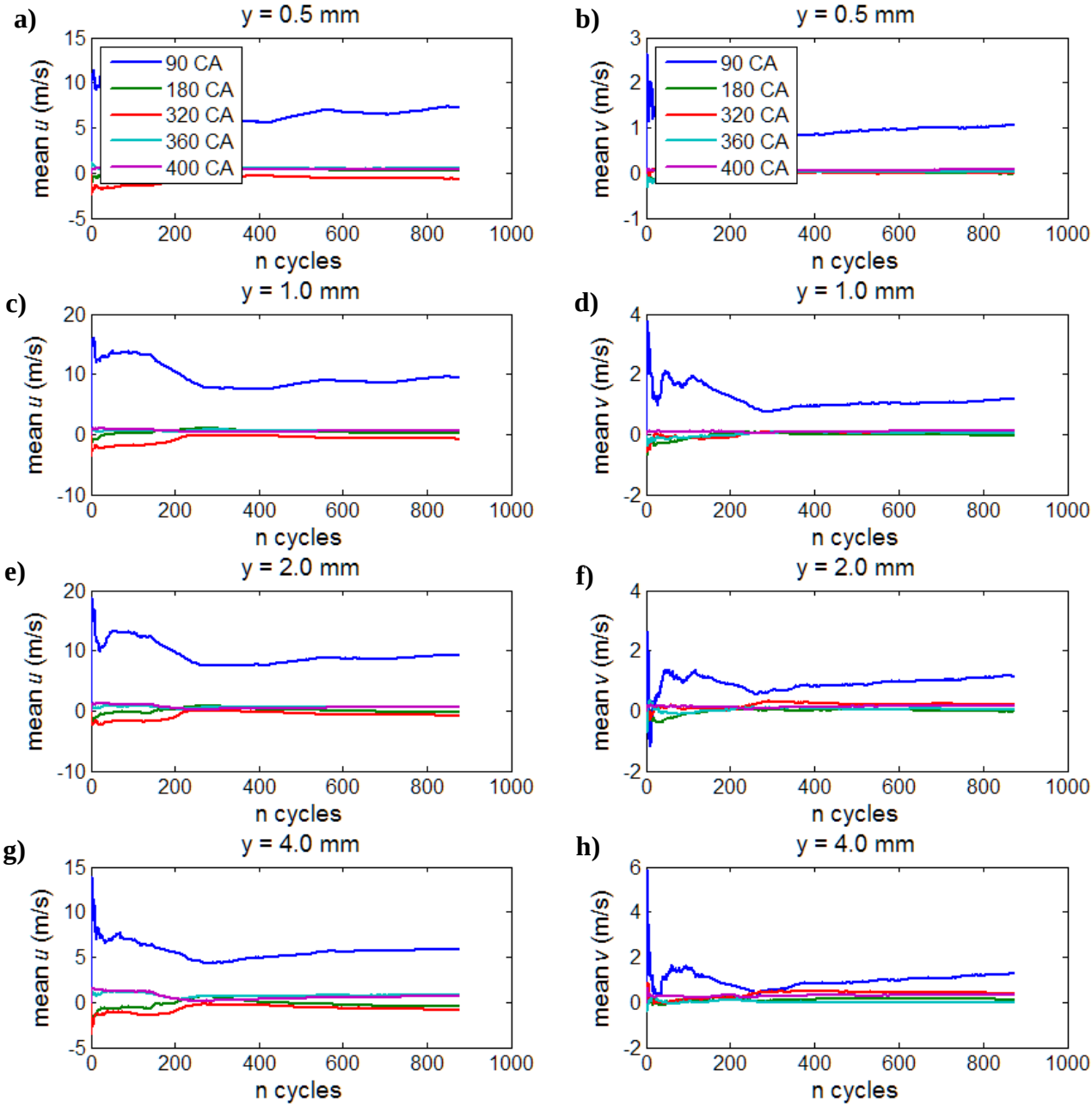

Figure 5-3 Velocity component mean as a function of sample size (cycles) for four wall-normal distances. Samples are taken at x = 2.0 mm from each flow field without any averaging process in the wall-parallel direction.

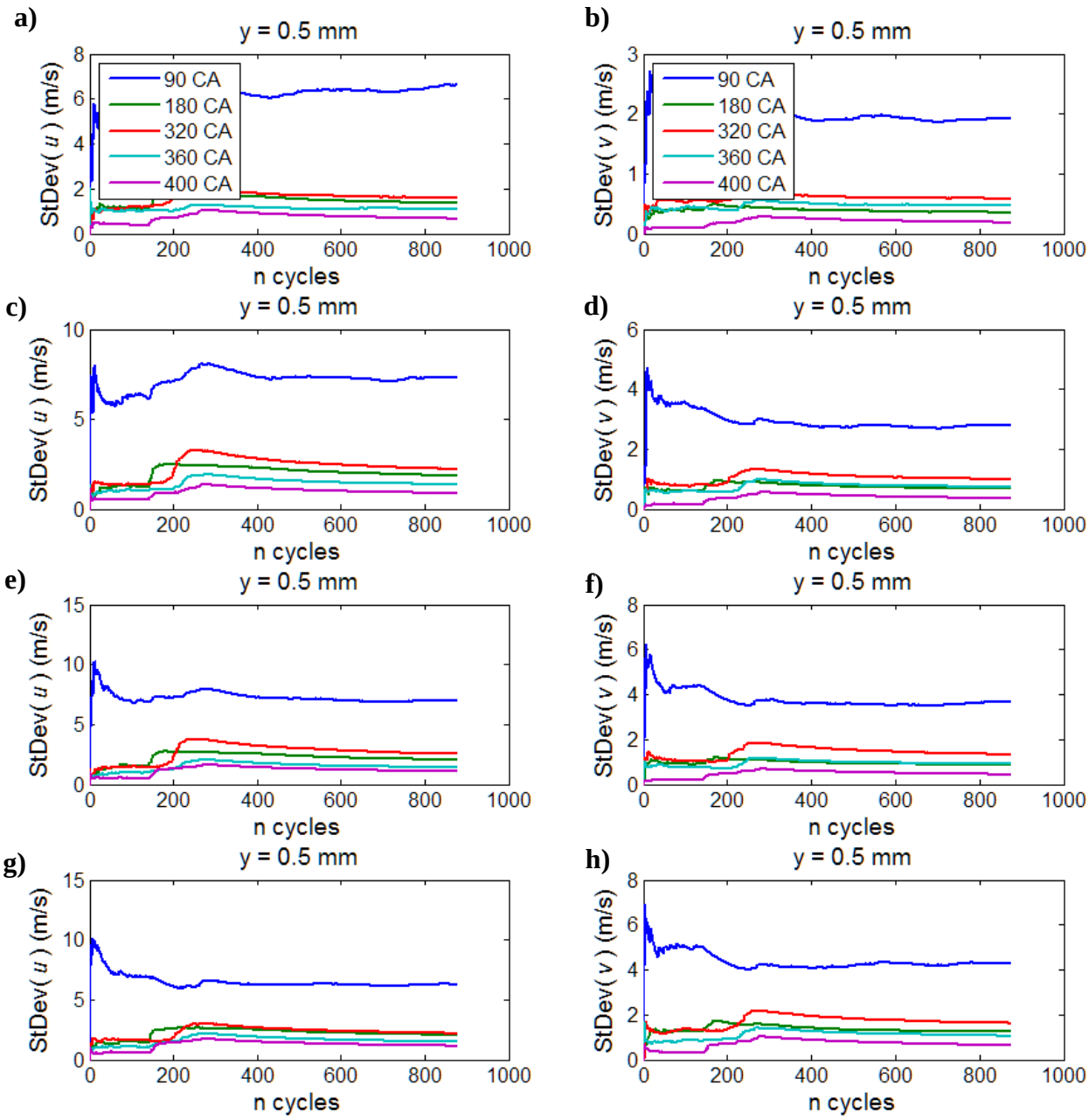

Figure 5-4 Velocity component standard deviation as a function of sample size (cycles) for four wall-normal distances. Samples are taken at x = 2.0 mm from each flow field without any averaging process in the wall-parallel direction.

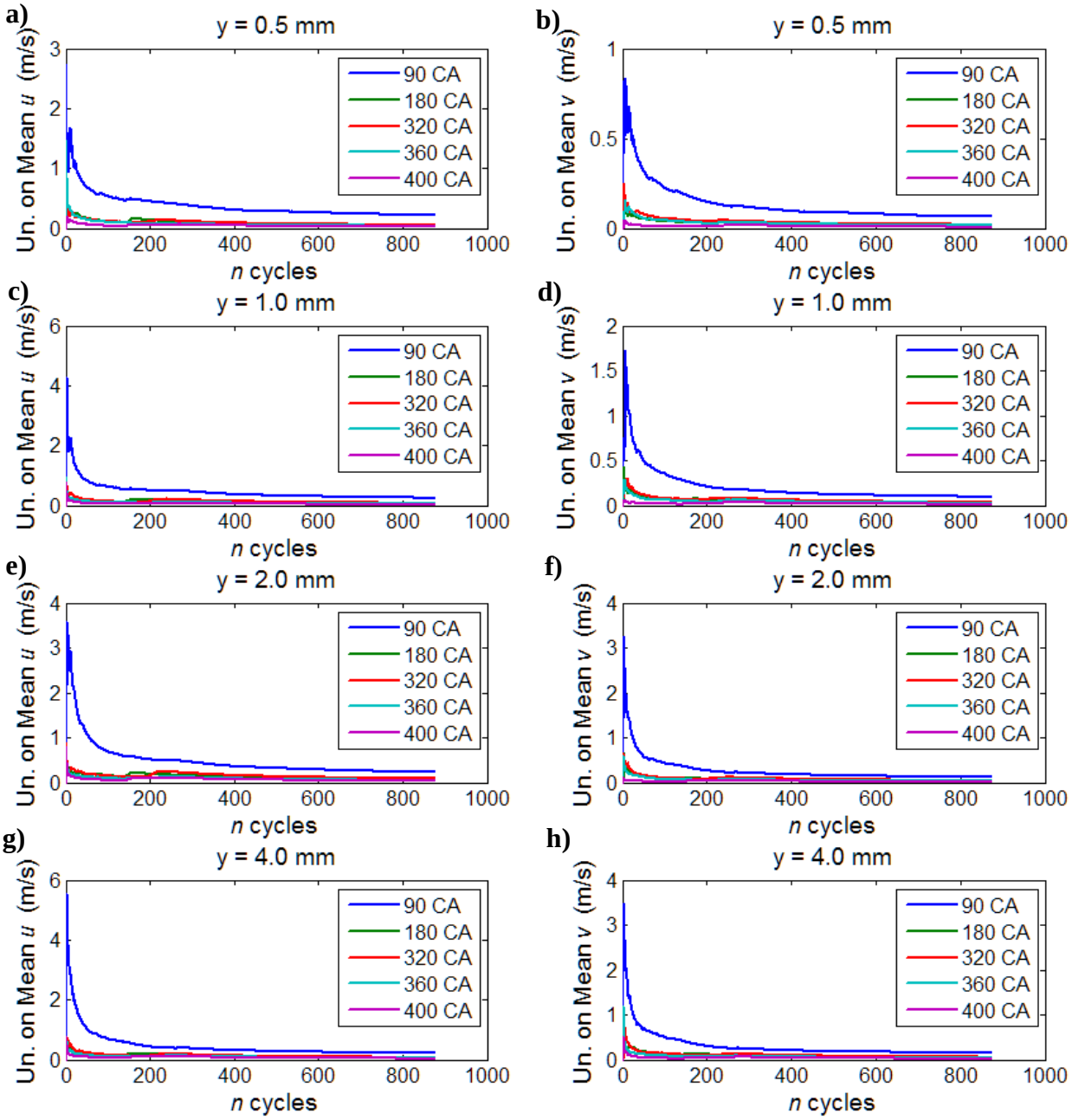

Figure 5-5 Statistical precision uncertainty of velocity component ensemble mean as a function of sample size (cycles) for four wall-normal distances. Samples are taken at x = 2.0 mm from each flow field without any averaging process in the wall-parallel direction.

5.3 Influence of Compression on Wall-normal component

The piston is undoubtedly the dominant forcing function of in-cylinder flows under motored and pre-combustion fired flows. The effect of the piston motion is most extreme on the wall-normal

velocity component *v*, where the piston motion alone is solely responsible for compressing the flow in the vertical direction by a factor of ten. While the flow velocity relative to every in-cylinder surface is responsible for the convective heat transfer characteristics at each location, it is of academic interest to attempt to remove the effect of the piston motion from the wall-normal velocity components *v*.

If a hypothetical inviscid fluid were to undergo compression and expansion from a piston, the wall-normal velocity of the fluid at the piston surface would necessarily match the piston speed to fulfill the no-through-flow boundary condition. Likewise the fluid at the head surface would likewise be stationary for the same reason. If this hypothetical fluid was also stationary prior to movement of the piston, the only flow within the cylinder would be an axial flow towards the head during compression and away from the head during expansion. In the absence of viscous forces no radial or azimuthal flow components could be generated by a forcing function acting solely in the axial direction. Furthermore, the profile of this axial velocity component would be linear along the height of the cylinder, joining the given velocities at the head and piston surfaces required by the boundary conditions as shown in Fig. 5-6.

This linear wall-normal (axial) velocity profile obtained from the theoretical compression and expansion of an inviscid fluid shown in Fig. 5-6 may be subtracted from the PIV flow-field measurements to remove an effect of the piston's motion from the wall-normal velocity component profiles. The relevant mapping from $\langle v \rangle$ to the adjusted velocity $\langle v \rangle^*$ is accomplished by

$$\text{At head surface:} \qquad \langle \boldsymbol{v} \rangle^* = \langle \boldsymbol{v} \rangle - \frac{\boldsymbol{y}}{\boldsymbol{h}} \boldsymbol{V_P} \qquad \text{5-1(a)}$$

$$\text{At piston surface:} \qquad \langle v \rangle^* = \langle v \rangle - \frac{h-y}{h} V_P \qquad \text{5-1(b)}$$

where *y* is the wall-normal distance from the imaged surface, *h* is the instantaneous cylinder height, and V_P is the instantaneous piston speed resolved in the local coordinate system at the imaged surface.

The resulting profiles are shown in the right column of Fig. 5-7. The left column of Fig. 5-9 is identical to the right column of Fig. 4-10 and is included for comparison. Comparing Fig. 5-9 (a) and (b) it can be seen that a significant portion, but not all, of the differences between crank

angles in the velocities of Fig. 5-7(a) have been removed by accounting for the inviscid compression profile in Fig. 5-7(b). A similar result is visible in Fig. 5-7 (c) and (d) where the inviscid compression profile has accounted for about half of the velocity magnitude observed at 315 CA, and for the majority of the magnitude observed at 350 CA. Note the profile at 180 CA is unchanged by the mapping as the piston is stationary at this point of the cycle, although of course the flow is still moving by its

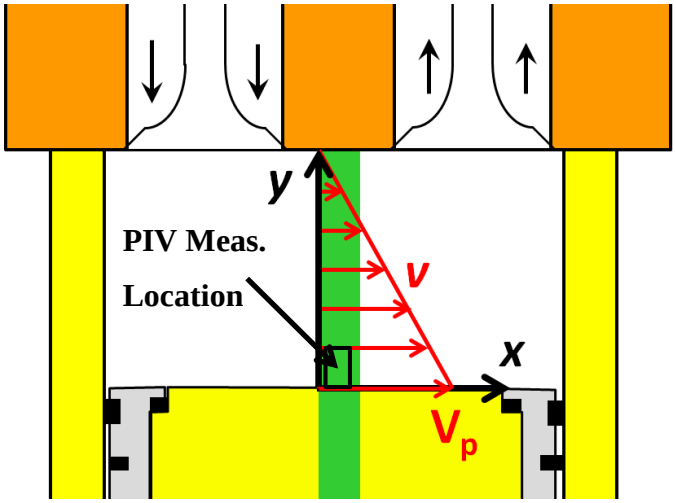

Figure 5-6 Schematic showing PIV measurement location on piston surface, coordinate system attached to piston surface utilized for measurements on the piston surface, and linear wall-normal velocity component *v* expected in a stationary, inviscid flow forced only by the piston motion.

own momentum gained by the prior forcing of the piston. Figures 5-7 (e) and (f) show a similar result for crank angles 350-, 370-, and 400 CA. Again the profile for 180 CA is unaffected. This analysis distinctly points out that at 320 CA the flow at the head surface is in the opposite direction of piston motion (towards the piston), a result highlighted by the marked increase in plotted velocity values for this crank angle. This effect highlights the limitations of this approach as the in-cylinder flow is driven by more than the piston motion alone, yet especially on the piston surface where flow against the piston motion is less likely to occur, this analysis does allow for comparison between crank angles to see where the flow is moving from/towards the surface faster than expected due to inviscid compression alone.

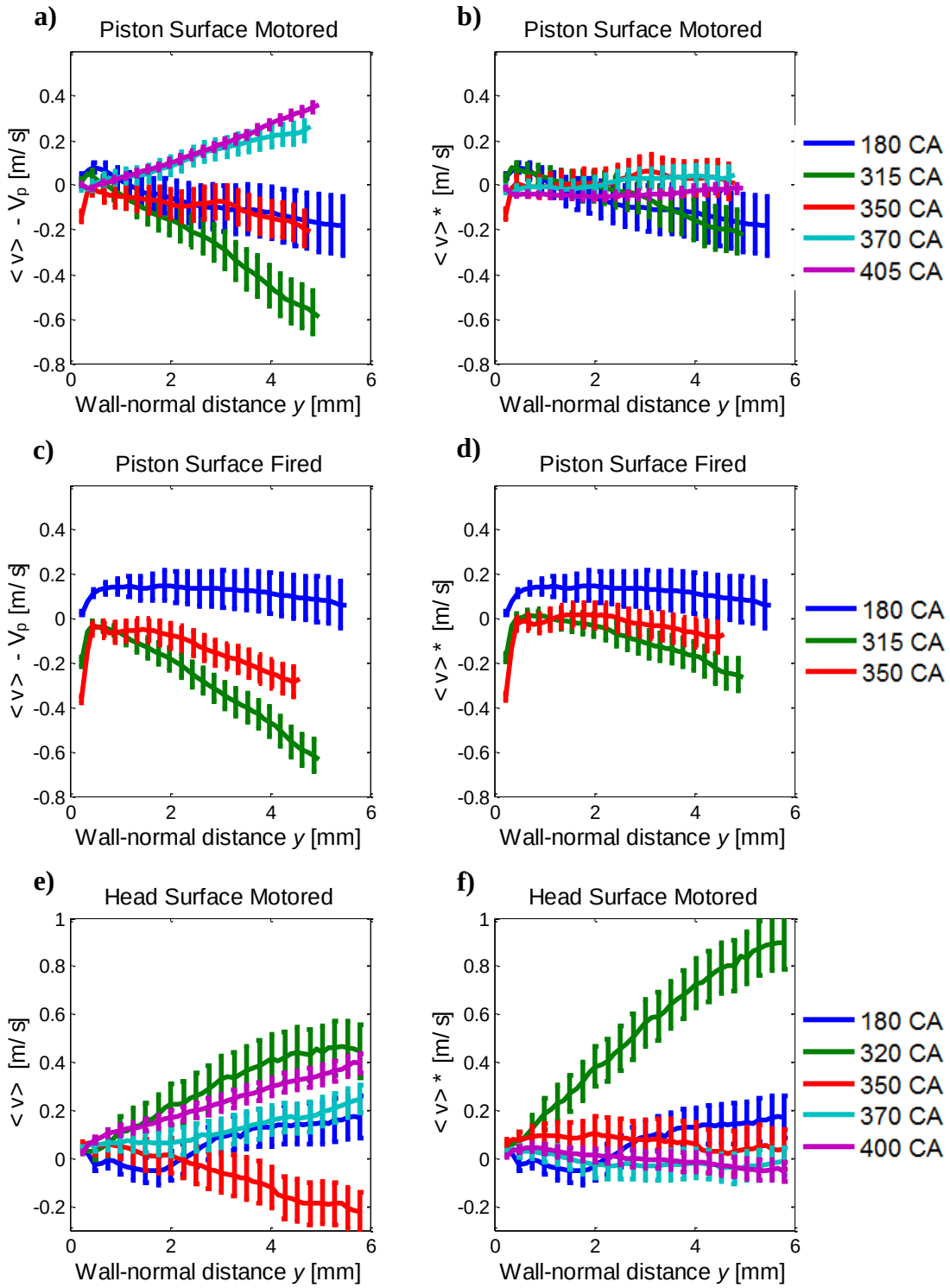

Figure 5-7 Effect of subtracting from the measured flow fields the wall-normal velocity profile of a theoretical inviscid fluid undergoing compression and expansion by a piston. The left column shows the wall-normal velocity component as shown previously in Figure with the measurements at the piston surface in (a) and (c) reported relative to instantaneous piston velocity. The right column presents the same measured data after the linear wall-normal velocity component in *v* has been subtracted from the measured velocity, as indicated by the asterisk.

5.4 Law of the wall

In this section the logarithmic law of the wall is applied to the near-wall velocity measurements reported in this work using the theory set forth in Section 2.2 and Eqs. 2-5 through 2-8. The in-cylinder gas has been taken as air, and the pressure through the cycle taken from experimental in-cylinder pressure measurements. The temperature used to calculate gas properties at the wall was taken from the experimental head-surface temperature measurements as reported in Section 4.4. Due to the near-adiabatic properties of the quartz piston window, it is anticipated the piston surface temperature would actually be higher than that measured on the head surface, particularly for fired tests, however in the absence of experimental measurements of the piston-surface temperature the head-surface temperature was still used for this analysis. The variation in head surface temperature through the cycle was then 10 °C (Fig. 4-14) even for the fired tests, which would result in a less than 1 percent error in the viscosity estimation made through Sutherlands law (White 2006). Instead, the cycle-average surface temperature for motored and fired operation was used for convenience.

To non-dimensionalize the near-wall layer with the wall-shear velocity, the velocity gradient at the wall was computed as a linear fit function ($y = ax$) through the first two data points from the wall. This approach was found to provide for a more appropriate estimation of the wall gradient for the results presented in this section, though the difference was small compared to using only the first measurement location.

Previous researchers (Alharbi and Sick 2010, Jainski, Lu et al. 2013) found poor agreement between their experimental near-wall engine measurements and the logarithmic law of the wall. Figure 5-8 presents a mapping of the measurements previously presented in Fig. 4-10 to log-low units where both distance and velocity are non-dimensionalized by the wall-shear velocity. As can be seen in the right column of the figure, consistent with others' findings, the logarithmic law of the wall does not appear to be particularly relevant to in-cylinder flows in the outer layer. Good agreement is seen between the experimental measurements and expected viscous inner-layer profile. Recall that the size of the measurement domain (5-x6 mm) was chosen with the goal of understanding the influence of the wall on the core flow, without necessarily resolving the full viscous layer. The linearity of the viscous inner-layer is generally considered valid for $y^+ < 5$. As

can be seen in Fig. 5-8 the first data point for each profile lies near $y^+ = 5$ demonstrating the appropriateness of the chosen field of view for the stated experimental goal.

It should be noted that at 180 CA for the fired test (Fig. 5-8(d)) nearly the entire measured profile (out to nearly 6 mm from the piston surface) follows the linear viscous inner-law. Additionally due to the low pressure at this portion of the cycle and the low wall-gradient, the first measurement point maps to a wall unit of $y^+ = 0.8$.

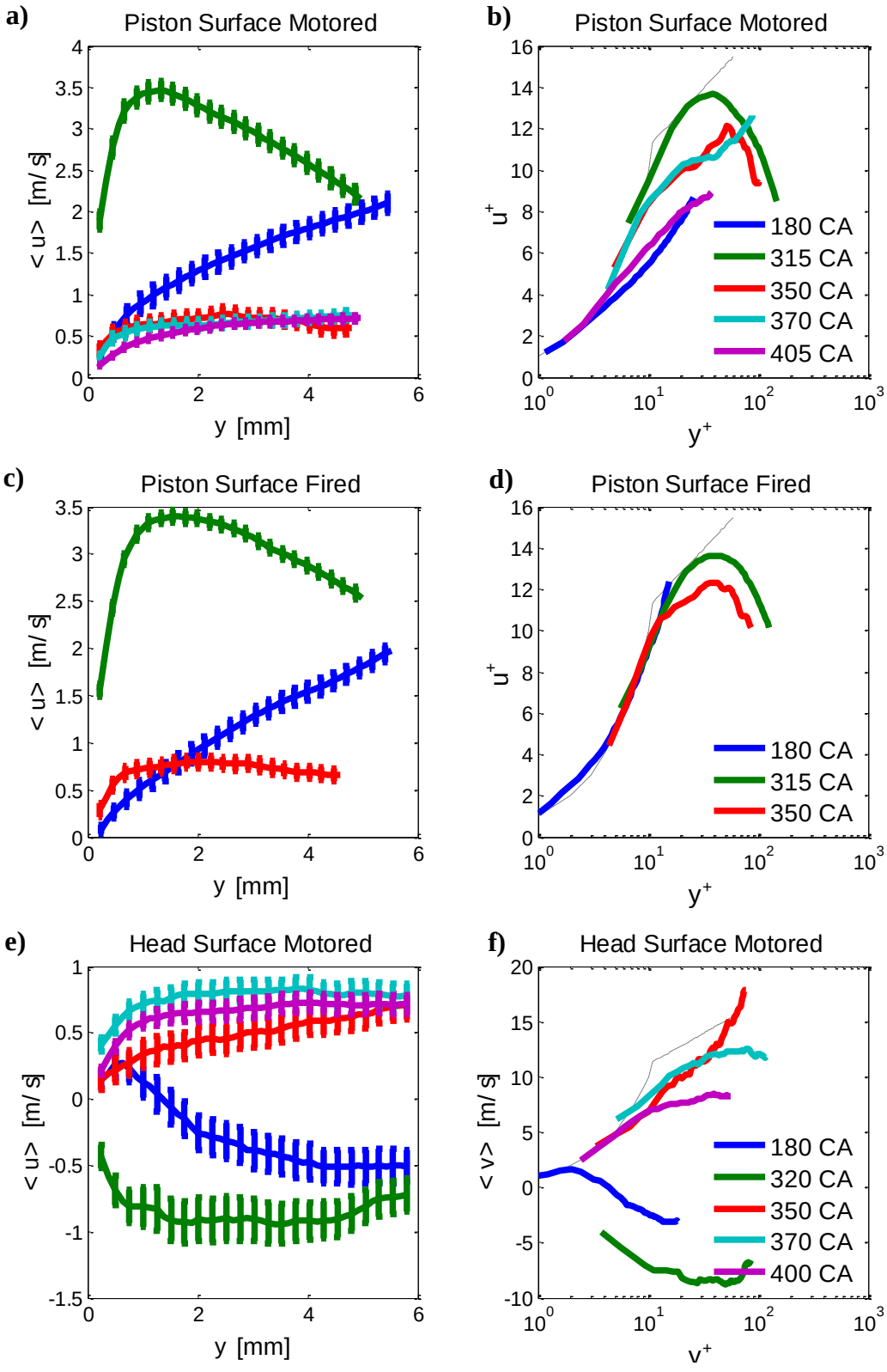

Figure 5-8 Logarithmic law of the wall mapping of the experimental data previously presented in Fig. 4-10.

5.5 Collaborative analysis of near-wall region thickness

The work presented in this section is a result of collaboration between the University of Michigan (UM) and Western Michigan University (WMU) under support from the NSF/DOE Advanced Combustion Engines program for the project "Development of a Dynamic Wall Layer Model for LES of Internal Combustion Engines". The results presented herein were computed at WMU with UM collaboration using the experimental near-wall velocity measurements as presented in Chapter 4 of this document, and are submitted to the SAE World Congress and Exhibition 2017 (MacDonald, Greene et al. 2017).

As discussed in Chapter 2 the thickness of traditional boundary layers is easily determined by a variety of metrics. However, as seen in Chapter 4 the nature and characteristics of the in-cylinder near-wall region varies tremendously throughout the cycle and between surfaces. Therefore it is of great academic interest to develop a robust metric universally applicable to in-cylinder surfaces to discuss the thickness of the near-wall region. Given the wide variety of near-wall flows observed in Section 4.1 that would preclude a robust means for determining the thickness of the near-wall layer of an individual flow field, a statistical approach was adopted.

In Section 4.3 regarding Fig. 4-5 the concept of how far from the wall the presence of the wall impacts the flow was introduced. The same concept guided the development of the metric for determining the near-wall layer thickness here. To achieve this goal a one-sided two-point correlation procedure was adopted

$$\boldsymbol{\rho_{vy}(y_i, \pm r)} = \frac{\langle \boldsymbol{v}(\mathbf{y}=\mathbf{y_i}) * \boldsymbol{v}(\mathbf{y}=\mathbf{y_i}\pm\boldsymbol{r})\rangle}{\sqrt{\langle \boldsymbol{v^2}(\mathbf{y}=\mathbf{y_i})\rangle * \langle \boldsymbol{v^2}(\mathbf{y}=\mathbf{y_i}\pm\boldsymbol{r})\rangle}} \qquad 5\text{-}2$$

where ρ_{vy} is the two-point correlation of the *v* velocity component in the wall-normal *y* direction, y_i is the distance from the wall from which the correlation originates, *r* is the correlation length, and angled brackets indicate an ensemble average. A horizontal average in the wall-parallel direction was performed to increase the sample pool for computation of statistics. $\pm r$ is shown because the correlation was taken both towards and away from the head surface. This enables comparison of the correlation values from a given wall-normal distance when looking towards the head wall (-*r*) versus away from the head wall (+*r*), i.e. towards the piston as shown in Fig. 5-11. For wall-normal *y* distances close to the wall, such as in Figs. 5-9 (a) and (d), lower correlation

values were obtained when looking towards the head surface (-*r*) indicating shorter integral length scales and smaller flow structures than when looking away from the surface (+*r*). However, as the origin point of the correlation is moved away from the wall, for some wall-normal distance y_i the correlation values computed towards the head surface and towards the piston will match, as seen in Figs. 5-9 (c) and (e). This indicates that at this distance from the wall, the correlations in the flow are independent of the presence of the wall, thereby presenting a robust metric for determining the depth into the flow at which the presence of the wall is felt. As can be seen in Figs. 5-9 (c) and (e) the wall-normal distance at which the correlations become independent of the wall is approximately 2.77 mm for the wall-parallel velocity component *u* and 4.85 mm for the wall-normal velocity component *v*. This result, that the wall influences the wall-normal component *v* further from the wall than the wall-parallel component *u* is consistent with the observations presented in Section 4.2.

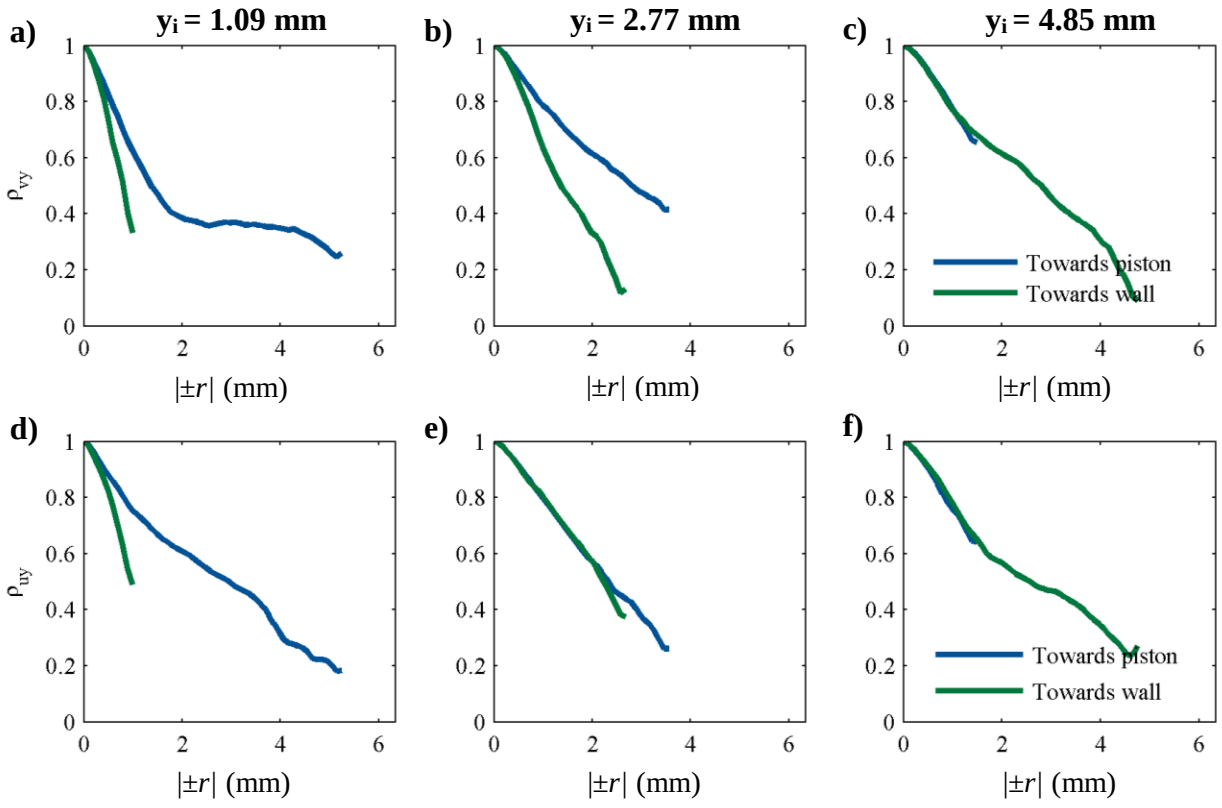

Figure 5-9 Directional correlations for the wall-normal velocity component (a) and wall-parallel velocity component (b) in the wall normal direction at 330 CA. In each case, the point at which the correlations overlap indicates the spatial extent of the wall-influence on the core flow. Adapted from (MacDonald, Greene et al. 2017)

Currently this analysis has only been applied to velocity data at 500 rpm motored taken at the head surface. Future computations on the remaining test conditions presented in Chapter 4 promise a fascinating comparison of the wall-layer thickness between in-cylinder surfaces, across engine speeds, and motored and fired operation. The method presented above of comparing single-sided two-point correlations towards and away from a surface as a metric to determine the "wall-influence" penetration depth on the flow holds great promise as a universal and robust metric to determine wall-layer thicknesses.

5.6 Collaborative development of wall heat transfer model

The work presented in this section is a result of collaboration between the University of Michigan (UM) and Stanford University under support from the NSF/DOE Advanced Combustion Engines program for the project "Development of a Dynamic Wall Layer Model for LES of Internal Combustion Engines". The results presented herein were developed and computed at Stanford with UM collaboration using the experimental near-wall velocity and head heat-flux measurements as presented in Chapter 4 of this document, and have been accepted to be published by the International Journal of Engine Research (Ma, Greene et al. 2016).

The law-of-the-wall presented in Section 2.2 presents a closed-form analytic expression that results from a number of assumptions that allow the non-equilibrium terms of the variable density low-Mach Navier-Stokes equations to be neglected (Ihme, Ma et al. 2016). These assumptions are 1) wall-parallel flow, 2) quasi-steady flow, 3) constant density and transport properties in the boundary layer, 4) high Reynolds number flow regime, 5) zero-pressure gradients, and 6) chemically inert mixture. As such the formulization of the law-of-the-wall can be termed an "equilibrium wall model" as the assumptions made in its derivation have eliminated the non-equilibrium terms of the Navier-Stokes equations.

The invalidity of the wall-parallel and quasi-steady flow assumptions has been discussed at length in Chapter 4 and elsewhere given the substantial wall-normal velocity contribution and rapid changes to the core flow seen throughout much of the cycle. Given the large thermal gradients between the hot core flow (due to compression) and the comparatively cold wall the

validity of the constant density and transport assumption is easily rebutted. An analysis of the critical transition Reynolds number presented in Section 2.3 showed in-cylinder flows to be far short of a typical high-Reynolds number flow. Of course engines violate the chemically inert assumption on the most obvious level.

Regarding the zero-pressure gradient assumption, (Ihme, Ma et al. 2016) computed the wall-parallel pressure gradient from the pressure Poisson equation 2 mm from the cylinder head wall from the experimental data of (Jainski, Lu et al. 2013). As can be seen in Fig. 5-10 where the computed wall-parallel pressure gradient is presented during a portion of the compression stroke, a significant adverse pressure gradient exists as TDC is approached.

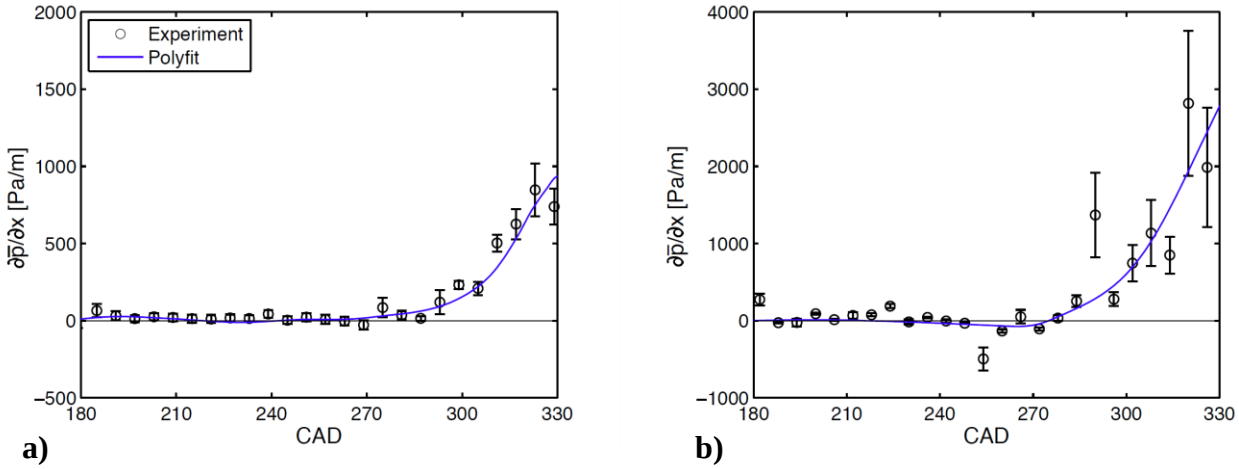

Figure 5-10 Pressure gradient extracted from experimental data as solution to the Poisson equation for (a) 400- and (b) 800 rpm. Experimental data are shown at every six CAs for clarity with the uncertainty bands representing one standard deviation of the data distribution for y values for $1.65 \leq y \leq 2.25$ mm. (Ihme, Ma et al. 2016)

To develop an improved wall-model for internal-combustion engine simulations (RANS or LES) that relaxes the false assumptions 1-5 listed above, (Ihme, Ma et al. 2016) proposed a "non-equilibrium" wall-model that retained the non-equilibrium terms of the variable density low-Mach Navier-Stokes equations neglected by the law-of-the-wall. Specifically all of the transient, convective, pressure gradient and pressure work terms in the momentum and temperature equations, and temperature-dependent variations in density and transport properties are retained in this formulation. The two-equation low-Reynolds number k-ω turbulence closure model was used. The pressure gradient was calculated from experimental measurements by the technique discussed

above. Unfortunately the analysis of (Ihme, Ma et al. 2016) was limited to the 150 CA range measured by (Jainski, Lu et al. 2013) as shown in Figure .

(Ma, Greene et al. 2016) built upon the limited analysis of the non-equilibrium wall-model to a much larger CA range extending from the mid-compression stroke to mid-expansion stroke made possible by the experimental measurements at the cylinder head presented in Chapter 4 of this document. The analysis was also extended to fired operation by including the heat-release term simulated by a one-dimensional GT-POWER model.

As can be seen in Fig. 5-11 which compares the equilibrium law-of-the-wall model, the non-equilibrium model just discussed, with experimental measurements as presented in Chapter 4, the non-equilibrium model is far superior in matching the shape of the near-wall profile of the experimental measurements. The vertical dashed line in Fig. 5-11 indicates the matching location which joins the experimental flow-field with the wall-model. In practical applications where the non-equilibrium model would be utilized as the wall-model in a RANS or LES simulation, the matching location would be the junction of the simulation domain and the modelled near-wall region.

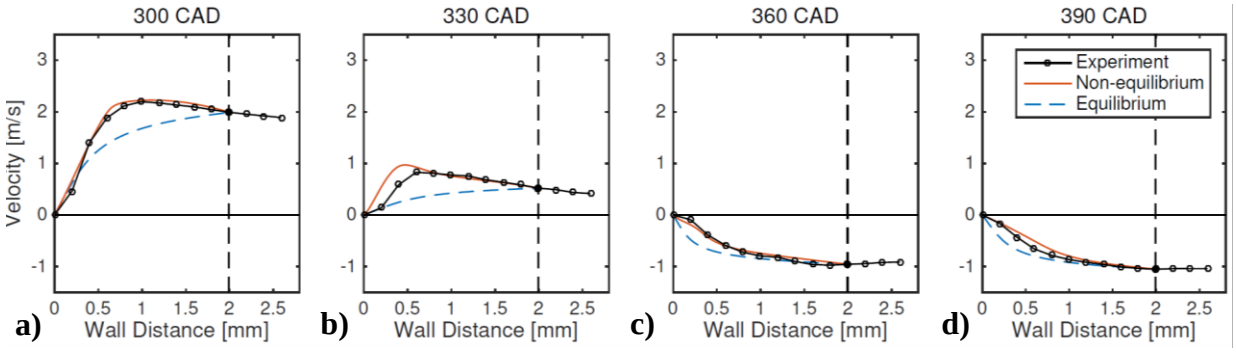

Figure 5-11 Velocity profiles predicted by non-equilibrium and equilibrium models in comparison with experimental measurements at the cylinder head under motored conditions at 500 rpm. (Ihme, Ma et al. 2016)

Figure 5-12 shows the relative error between the modelled shear velocity and that calculated from experimental results for both the equilibrium law-of-the-wall model and the non-equilibrium model presented by this work when calculated using various matching location distances, y_p. As can be seen the equilibrium model has errors exceeding 80 percent in the late compression stroke, while for all practical matching location distances the non-equilibrium model is associated with drastically lower error values.

In addition to the comparisons of the non-equilibrium models momentum boundary-layer predictions, as the non-equilibrium model requires simulating all four of the Navier-Stokes equations, the model's predictions for wall heat transfer were compared to the measured results presented in Section 4.4. Figs. 5-13 and 5-14 compare the experimental heat flux at the cylinder head under motored and fired conditions at 500 rpm to that as calculated by the non-equilibrium wall-model, the equilibrium model, and the three most common heat-transfer correlations utilized in the IC engine community, all of which were discussed in Chapter 1 (Annand 1963, Woschni 1967, Rakopoulos, Kosmadakis et al. 2010).

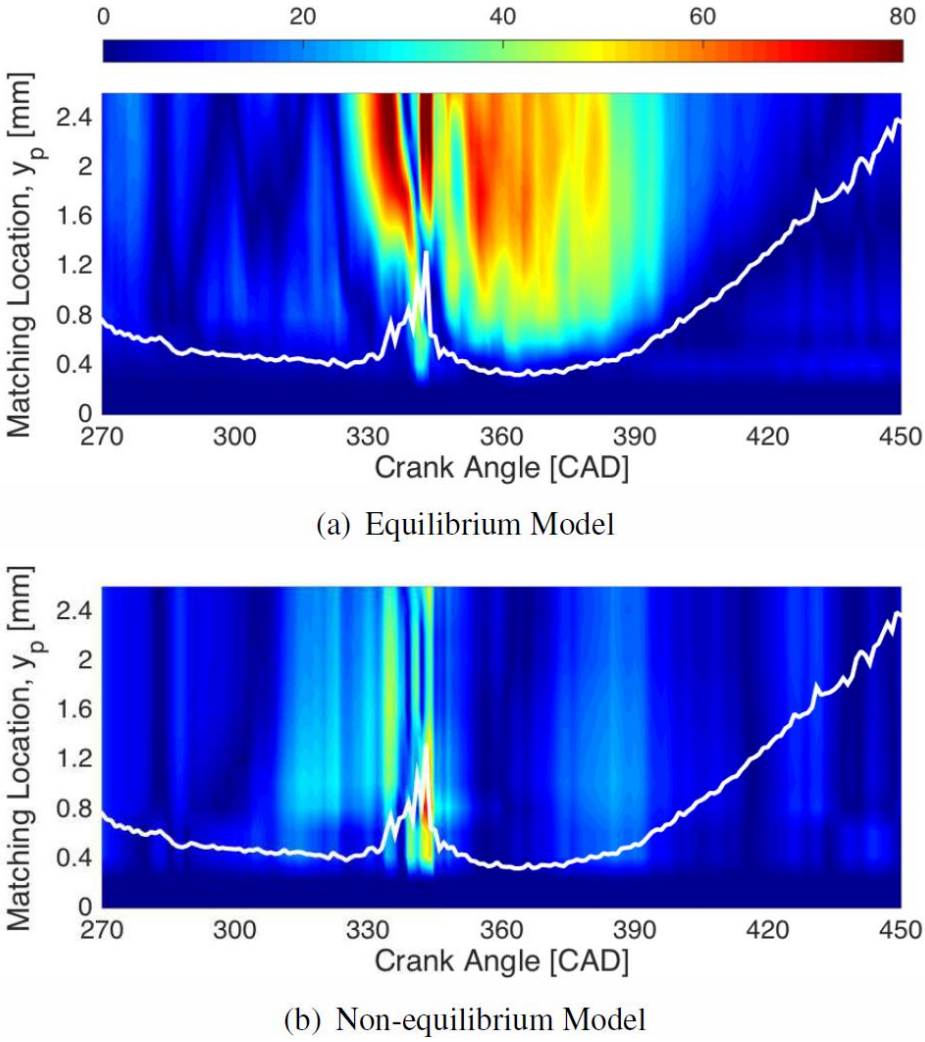

Figure 5-12 Relative error (in percentage) in shear velocity between (a) equilibrium and (b) non-equilibrium models and the experimental measurements at the cylinder head at motored conditions and 500 rpm. The white line marks the buffer layer location at y^+ = 11 (Ma, Greene et al. 2016)

As shown in Fig. 5-13 only the non-equilibrium model and the model of Rakopoulos accurately predict the CA timing of peak heat flux, while the non-equilibrium model comes most closely to predicting the measured peak heat flux though it overpredicts the heat flux from mid compression stroke to early in the expansion stroke, and underpredicts the heat flux during the majority of the expansion stroke.

Figure 5-14 shows the same comparison between the measured heat flux and models as just discussed regarding Fig. 5-13, but under fired conditions at 500 rpm. As can be seen the measured heat flux increases by over an order of magnitude, and only the non-equilibrium model comes close to predicting the measured peak heat flux, though still significantly underpredicting the value. Apart from Rakopoulos, the models all accurately predict the CA timing of the measured peak heat flux.

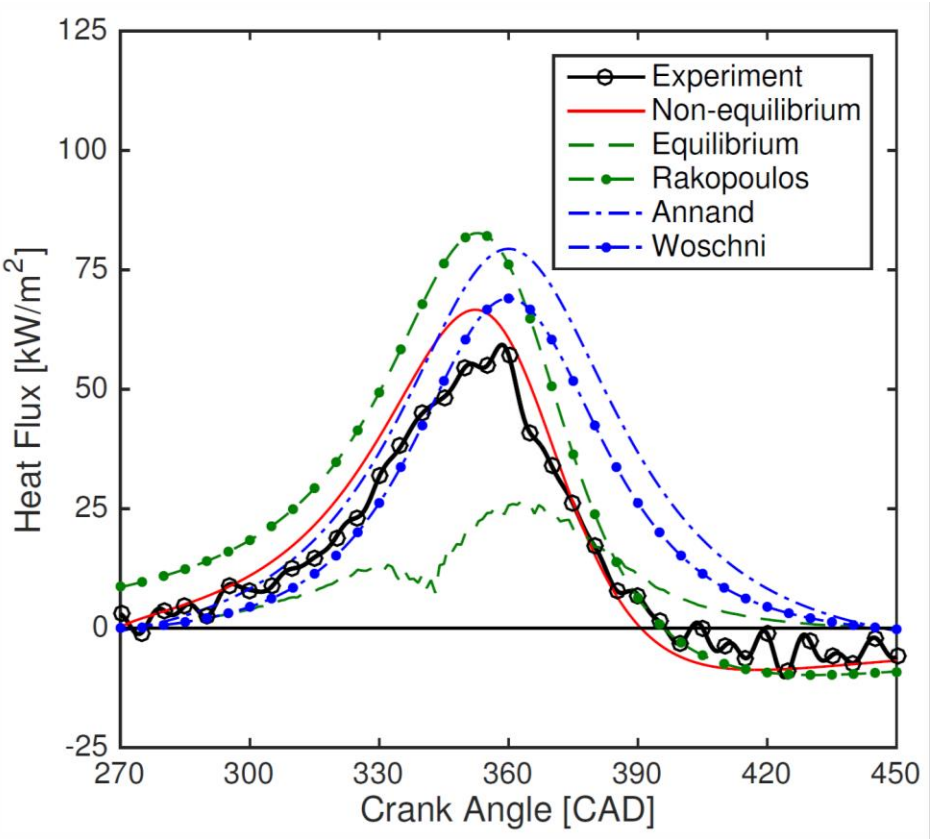

Figure 5-13 Heat flux predicted by different models in comparison with measurements at the cylinder head for motored conditions at 500 rpm. (Ma, Greene et al. 2016)

As shown in the figures and discussion here, the development of the non-equilibrium model is not an incremental improvement in wall-models for use in IC engine simulations, rather it marks a fundamental shift towards physics-based models guided by fundamental insights derived from high-resolution measurements like those presented in this dissertation, such as the presence of an adverse pressure gradient at the wall. Additionally the experimental work presented in this document includes the first velocimetry measurements to be conducted with a focus on the near-wall flows at the piston surface. These experiments enable the extension of model development and validation to additional in-cylinder surfaces for which experimental measurements were previously unavailable.

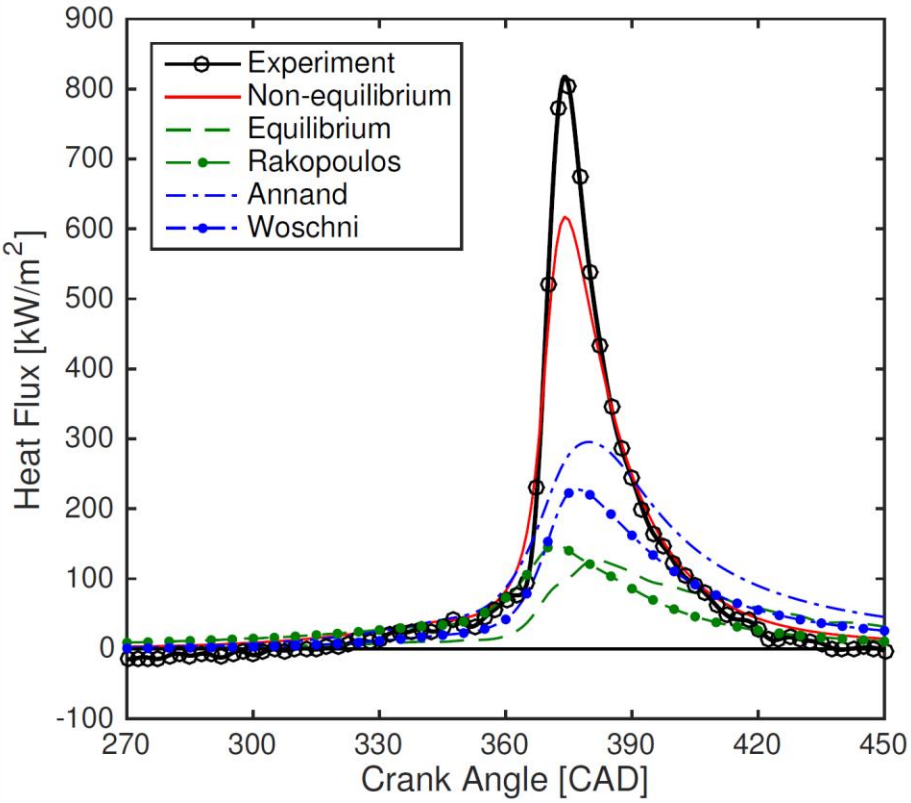

Figure 5-14 Heat flux predicted by different models in comparison with measurements at the cylinder head for fired conditions at 500 rpm. (Ma, Greene et al. 2016)

5.7 Sources of experimental error

No experimental work would be complete without a discussion of the numerous sources of error inherent in experimental measurements. Some sources of measurement error have already been previously discussed at length (e.g. determination of wall location in Section 3.3) or mentioned in passing (e.g. laser sheet thickness also in Section 3.3), but the hope is to present a discussion of the most important error source, far short of a comprehensive list, of the most important sources of error in the measurements presented in this work.

To begin the discussion, likely the largest source of error in these measurements originates from the laser sheet thickness and strong out-of-plane motion which characterizes the measurement locations in this engine. In PIV measurements out-of-plane motion appears as in-plane motion for particles away from the center of the imaging system axis (center of image). This effect is compounded by the laser sheet thickness of 0.5±0.1 mm which is approximately twice the 'ideal' thickness of laser sheet used in PIV. In an ideal circumstance the sheet thickness used in PIV should be no greater than the dimension of the interrogation window used in PIV processing (0.25 mm in these experiments) such that the interrogation volume becomes a cube. A thicker sheet allows for greater out-of-plane motion of the particles within the sheet, which means a larger error in the in-plane measurement. However as stated in Section 3.3, these experiments would not have been possible without the thickened laser sheet as an insufficient number of particle image pairs would have been captured in the images. A camera with a shorter minimum pulse delay between frames, or use of double-pulsed frames, could have offset some of this difficulty but a balance exists between reducing out-of-plane motion with sufficient in-plane motion for accurate detection of particle shifts.

Along the same line, the targeted particle pixel shift between images of 3 pixels is an additional source of error in these measurements. Under ideal circumstances, a pixel shift of ¼ the interrogation window size (8 pixels for this work) is used. Even with subpixel accuracy PIV algorithms, the precision of the PIV system is improved for greater particle displacements, *ceteris paribus*. This is due to the subpixel accuracy contributing to a smaller proportion of the overall particle displacement.

Particle seeding density is an additional source of error in these measurements. Ideally the flow should be seeded such that 8-10 particles are found in each interrogation window. In these experiments seed density was iteratively adjusted between preliminary experiments to achieve as close to this seed density is possible. However, in low density phases of the cycle and near the wall this seeding density was not able to be obtained.

It should also be noted that the seeding near the wall is dependent upon sweep events bringing particles to the wall. As these sweep events originate from the higher-energy core-flow it is possible the stochastic seeding of the wall is biased towards higher velocities. The degree to which this effect affects the measurement results cannot be determined.

The determination of the location of the wall in the images is another source of error for results dependent upon the wall gradient. As discussed in Section 3.3, the process used to identify the location of the wall is believed to be accurate to within 1 pixel, which equates approximately 8 μm for these measurements and a 3 percent uncertainty in the wall-normal distance reported for the measurement location closest to the wall.

Another source of error in these measurements is the spatial calibration procedure of the imaging system. Due to difficulties holding and illuminating the calibration target within the cylinder at the precise measurement location, the effort required to achieve this typically trivial task was not expected. The target was backlit by room lights with a mirror and fixed in place by a custom mount that restrained the target in the radial direction.

With a narrow laser sheet an additional source of error in these measurements is aligning the sheet to the desired measurement location. A printed target was first aligned to scours on the piston surface, and then the laser sheet aligned to the target. It is believed the uncertainty of placement of the sheet is no greater than 1 mm.

Lastly, all electronics contain some jitter in their signal and in their operation, however for the electronics and lasers used in these experiments this would be quite small. A discussion of this source of uncertainty, most prevalent to the time delay between laser pulses, seems unnecessary in light of the far larger sources of error enumerated above.

Conclusions

Past researchers have shown that near-wall regions in engines are characterized by unsteady, transient boundary layers that do not compare to the teachings of canonical flows (Alharbi and Sick 2009, Alharbi and Sick 2010, Jainski, Lu et al. 2013). However, accurately modeling the transfer of mass, momentum, and particularly energy through engine near-wall regions is critical to achieving the long-standing goal of predictive engine simulations that would enable engine designers to harness the full potential of computational design. The principle motivation of this work is to develop physical insights and physics-based concepts to effect improved engine simulations.

This dissertation presents the development of a unique particle image velocimetry system that both overcomes inherent challenges in conducting near-wall measurements in the current engine but also teaches general techniques broadly applicable to near-wall imaging in internal combustion engines. The importance of an inclined imaging-axis to reduce aberrations and improve imaging quality, and the specific selection of PIV processing parameters including the significance of carefully aligning the wall surface to the PIV vector grid are both aspects of the current experimental setup highly recommended to one planning in-cylinder near-wall experiments in the future.

The experimental database assembled in this work complements existing comprehensive large-scale flow measurements to give the TCC engine the most complete public documentation of in-cylinder flow of any engine. Furthermore, the near-wall velocimetry database gathered here at the head and piston surfaces at both 500- and 1300 rpm under motored and fired engine conditions extends the boundaries of engine near-wall region measurements in very significant ways, in that it:

- provides the first nearly full-cycle resolved near-wall velocimetry measurements, and the first velocimetry measurements resolved every crank angle degree from the before intake valve opening to well after top-dead-center compression,
- provides the first near-wall planar velocimetry measurements in a fired engine,
- provides the first near-wall velocimetry measurements on the piston surface,
- expands the engine-speed envelope for near-wall planar velocimetry measurements to higher engine speeds,
- and, is accompanied by high-speed head-surface temperature and heat-flux measurements.

Conclusions drawn from the presented work include:

- In-cylinder surfaces are exposed to a wide variety of flow types throughout the cycle including wall-parallel flow, impinging jet flows, wall jet flows, and shear flows.
- The wall influences the wall-normal component of velocity farther from the wall than the wall-parallel component, in agreement with the same conclusion reached via a recent DNS investigation (Schmitt 2014).
- The wall-normal velocity component appears to scale superlinearly with engine speed within the near-wall region, both at the head and piston surfaces.
- Velocity magnitudes are similar at the head and piston surfaces when the piston is stationary, but can vary significantly during parts of the cycle characterized by high piston speed, even when normalized for piston speed.

Furthermore, the experimental measurements presented here have directly supported collaborative efforts that yielded significant contributions to the field:

- Through the appropriate selection of the field-of-view of these measurements, by reaching a balance between resolution of the near-wall layer while still measuring the edge of the core flow, a robust metric for determining the near-wall layer thickness through a single-sided two-point correlation approach has been presented (MacDonald, Greene et al. 2017).
- A non-equilibrium wall model for LES and RANS engine simulations has been developed that significantly improves the prediction of both the near-wall velocity profile and heat

flux over all existing models (Ma, Greene et al. 2016). The non-equilibrium model reduces error the error in peak heat-flux prediction by nearly 40 percent over the next most accurate model.

Despite the significant advances made by the present work more experimental effort regarding in-cylinder near-wall measurements is critical in rounding out understanding of near-wall processes. High-spatial-resolution gas-temperature measurements ought to be conducted at both the cylinder head and piston surface in the TCC engine to provide and validate thermal boundary conditions for the meshed domain for LES and RANS simulations. Furthermore these measurements may confirm the observations of (Schmitt 2014) regarding the spatial-scale and frequency of thermal structures near the wall.

Additional measurements ought to be conducted in engines of more conventional geometries, including four-valve pent-roof engines, and engines equipped with more realistic piston geometries including a piston bowl, to both compare and comment on the universality of conclusions achieved in the current work across engine geometries.

A need also exists for near-wall measurements taken at more realistic engine speeds, and under load, as currently the effects of these parameters on the near-wall behavior are unexplored, and the extrapolation of trends observed in relatively small changes in speed at low engine speeds is unverified. Exploring either of these parameters would require an engineering feat in and of itself in terms of engine design, as optical engines are inherently limited to slow speeds by the massive weight of the extended Bowditch piston, and typically run at low load to reduce stress on the optical cylinder liner.

These investigations are an essential effort towards the development of improved models for wall heat transfer in reciprocating internal-combustion engines. The TCC-III engine used in this study can be considered a canonical engine and experimental data from this engine are used widely for benchmarking, model development and validation of CFD simulations (Kuo, Yang et al. 2013, Schiffmann, Gupta et al. Article in Press, 2015). The near-wall flow database is publically available on an archival server for download.

References

"TCC-III Benchmark Data." from http://deepblue.lib.umich.edu/handle/2027.42/108382.

Abraham, P., D. Reuss and V. Sick (2013). High-speed particle image velocimetry study of in-cylinder flows with improved dynamic range, SAE Technical Paper.

Abraham, P. S., X. Yang, S. Gupta, T.-W. Kuo, D. L. Reuss and V. Sick (2015). "Flow-pattern switching in a motored spark ignition engine." International Journal of Engine Research: 1468087414565400.

Adrian, R. J. (2007). "Hairpin vortex organization in wall turbulence." Physics of Fluids (1994-present) **19**(4): -.

Alharbi, A. and V. Sick (2009). "Investigation of Boundary Layer in Internal Combustion Engines using High-Speed Micro-PIV." 6th U.S. National Combustion Meeting.

Alharbi, A. and V. Sick (2010). "Investigation of boundary layers in internal combustion engines using a hybrid algorithm of high speed micro-PIV and PTV." Experiments in Fluids **49**(4): 949-959.

Alkidas, A., P. Puzinauskas and R. Peterson (1990). "Combustion and heat transfer studies in a spark-ignited multivalve optical engine." Training **2013**: 11-11.

Alkidas, A. C. (1980). "Heat Transfer Characteristics of a Spark-Ignition Engine." Journal of Heat Transfer **102**: 189-193.

Angelberger, C., T. Poinsot and B. Delhay (1997). Improving near-wall combustion and wall heat transfer modeling in SI engine computations, SAE Technical Paper.

Angioletti, M., R. M. Di Tommaso, E. Nino and G. Ruocco (2003). "Simultaneous visualization of flow field and evaluation of local heat transfer by transitional impinging jets." International Journal of Heat and Mass Transfer **46**(10): 1703-1713.

Annand and T. H. Ma (1971). "Instantaneous heat transfer rates to the cylinder head surface of a small compression-ignition engine." Proc. IMechE, Part D: J. Autom. Eng **185**: 976–987.

Annand, W. J. (1963). "Heat transfer in the cylinder of reciprocating internal engines." Proc. Instn Mech. Engrs. **173**(36): 973-990.

Asanuma, T. and T. Obokata (1979). "Gas velocity measurements of a motored and firing engine by laser anemometry." SAE Technical Paper 790096.

Baughn, J. W. and S. Shimizu (1989). "Heat Transfer Measurements From a Surface With Uniform Heat Flux and an Impinging Jet." Journal of Heat Transfer **111**(4): 1096-1098.

Beltaos, S. and N. Rajaratnam (1973). "Plane turbulent impinging jets." Journal of Hydraulic Research **11**(1): 29-59.

Bernard, P. S. and J. M. Wallace (2002). Turbulent flow: analysis, measurement, and prediction, John Wiley & Sons.

Blasius, H. (1908). "Grenzschichten in Flüssikeiten mit kleiner Reibung." Zeitschrift fiirMthematik und Physik **56**(1): 1-37.

Borgnakke, C., V. S. Arpaci and R. J. Tabaczynski (1980). "A model for the instantaneous heat transfer and turbulence in a spark ignition engine." Combustion **2012**: 06-06.

Borman, G. and K. Nishiwaki (1987). "Internal-combustion engine heat transfer." Progress in Energy and Combustion Science **13**(1): 1-46.

Bovo, M. and L. Davidson (2013). "On the Numerical Modeling of Impinging Jets Heat Transfer—A Practical Approach." Numerical Heat Transfer, Part A: Applications **64**(4): 290-316.

Chang, O. Guralp, Z. Filipi, D. N. Assanis, T. W. Kuo and P. Najt (2004). "New heat transfer correlation for an HCCI engine derived from measurements of instantaneous surface heat flux." SAE Paper 2004-01-2996.

Chen, C. and A. Veshagh (1992). "A one-dimensional model for in-cylinder heat convection based on the boundary layer theory." SAE International **921733**.

Chen, K. and G. A. Karim (1998). "Evaluation of the instantaneous unsteady heat transfer in a rapid compression – expansion machine." J. Power Energy **212**(5): 351-362.

Chirkov, A. A. and B. S. Stefanovski (1958). "О доминирующем способе передачи тепла в цилиндрах двигателей внутреннего сгорания." Trudy Rostovskova Instituta Injyenyerov Fyelyeznodorovnova Transporta **21**.

Cho, K., D. Assanis, Z. Filipi, G. Szekely, P. Najt and R. Rask (2008). "Experimental investigation of combustion and heat transfer in a direct-injection spark ignition engine via instantaneous combustion chamber surface temperature measurements." Proceedings of the Institution of Mechanical Engineers, Part D: Journal of Automobile Engineering **222**(11): 2219-2233.

Chung, Y. M., K. H. Luo and N. D. Sandham (2002). "Numerical study of momentum and heat transfer in unsteady impinging jets." International Journal of Heat and Fluid Flow **23**(5): 592-600.

Cierpka, C., S. Scharnowski and C. J. Kähler (2013). "Parallax correction for precise near-wall flow investigations using particle imaging." Applied Optics **52**(12): 2923-2931.

Cole, J. and M. Swords (1980). "An investigation of the ignition process in a lean-burning engine using conditionally sampled laser-doppler anemometry." SAE Paper 800043.

Dao, K., O. Uyehara and P. Myers (1973). Heat transfer rates at gas-wall interfaces in motored piston engine, SAE Technical Paper.

Dec, J. E. (2009). "Advanced compression-ignition engines—understanding the in-cylinder processes." Proceedings of the Combustion Institute **32**(2): 2727-2742.

Eichelberg, G. (1939). "Some new investigations on old combustion engine problems." Engineering **148**(27): 463-466.

Eichelberg, G. and W. Pflaum (1951). "Untersuchung eines hochaufgeladenen Dieselmotors." Z. Ver. dtsch. Ing. **93**: 1113.

Elser, K. (1954). "Der instationäre Wämeübergang in Diesel-motoren." Mitt. Inst. Thermodyn. Zürich **15**.

Fansler, T. D. (1985). "Laser velocimetry measurements of swirl and squish flows in an engine with a cylindrical piston bowl." SAE Technical Paper 850124.

Fiveland, S. B. and D. N. Assanis (2001). Development of a Two-Zone HCCI Combustion Model Accounting for Boundary Layer Effects, SAE International.

Foster, D. and P. O. Witze (1987). "Velocity Measurements in the Wall Boundary Layer of a Spark-Ignited Research Engine." SAE Paper 872105.

Franco, A. and L. Martorano (1998). Evaluations on the Heat Transfer in the Small Two-stroke Engines, SAE International.

Gamma Technologies, I. (2013). Engine (GT-Power) Reference Templates. EngCylHeatTr - Cylinder Heat Transfer Model**:** 3.

Gardon, R. and J. C. Akfirat (1965). "The role of turbulence in determining the heat-transfer characteristics of impinging jets." International Journal of Heat and Mass Transfer **8**(10): 1261-1272.

Grief, T. Namba and M. Nikanham (1979). "Heat transfer during piston compression including side wall and convection effects." Int. J. Heat and Mass Transfer **22**: 901-907.

Hadziabdic, M. and K. Hanjalic (2008). "Vortical structures and heat transfer in a round impinging jet." Journal of Fluid Mechanics **596**: 221-260.

Hall, M. and F. V. Bracco (1986). "Cycle-Resolved Velocity and Turbulence Measurements Near the Cylinder of a Firing S. I. Engine." SAE Paper 861530.

Han, Z. and R. D. Reitz (1997). "A temperature wall function formulation for variable-density turbulent flows with application to engine convective heat transfer modeling." Int. J. Heat and Mass Transfer, 40(3), 613-625, 1997. **40**(3): 613-625.

Hattori, H. and Y. Nagano (2004). "Direct numerical simulation of turbulent heat transfer in plane impinging jet." International Journal of Heat and Fluid Flow **25**(5): 749-758.

Heywood, J. B. (1988). Internal combustion engine fundamentals, Mcgraw-hill New York.

Hohenberg, G. F. (1979). "Advanced Approaches for Heat Transfer Calculations." SAE Paper 790825.

Huh, K. Y., I.-P. Chang and J. K. Martin (1990). A comparison of boundary layer treatments for heat transfer in IC engines, SAE Technical Paper.

Ihme, M., P. C. Ma, M. Greene, V. Sick, C. Jainski and A. Dreizler (2016). Non-equilibrium Wall-Modeling for Simulations of Internal Combustion Engines. THIESEL 2016 Conference on Thermo- and FLuid Dynamic Processes in Direct Injection Engines. Valencia, Spain.

Jainski, C. (2011). Measurements of Wall Boundary Layers in Internal Combustion Engines Using Particle Image Velocimetry (PIV) at High Reptition Rates. Masters of Science Masters, Technische Universitat Darmstadt.

Jainski, C., L. Lu, A. Dreizler and V. Sick (2013). "High-speed micro particle image velocimetry studies of boundary-layer flows in a direct-injection engine." International Journal of Engine Research **14**(3): 247-259.

Jainski, C., L. Lu, V. Sick and A. Dreizler (2014). "Laser imaging investigation of transient heat transfer processes in turbulent nitrogen jets impinging on a heated wall." International Journal of Heat and Mass Transfer **74**: 101-112.

Janeway, R. (1929). "Interpretation of the Indicator Card." SAE International **24**: 92-101.

Janeway, R. (1938). "Quantitative Analysis of Heat Transfer in Engines." SAE International 380163 **2008**: 04-15.

Kähler, C. J., U. Scholz and J. Ortmanns (2006). "Wall-shear-stress and near-wall turbulence measurements up to single pixel resolution by means of long-distance micro-PIV." Experiments in Fluids **41**(2): 327-341.

Ku, P. M. (1940). Factors Affecting Heat Transfer in the Internal-Combustion Engine, DTIC Document.

Kundu, P., I. Cohen and D. Dowling (2012). Fluid Mechanics. New York, NY, Academic Press.

Kuo, T.-W., X. Yang, V. Gopalakrishnan and Z. Chen (2013). "Large Eddy Simulation (LES) for IC Engine Flows." Oil & gas science and technology **Online Open Access 10.2516/ogst/2013127**.

Lancaster, D. R. (1976). Effects of engine variables on turbulence in a spark-ignition engine.

Lanchester, F. (1939). "The Energy Balance Sheet of the Internal Combustion Engine." Proceedings of the Institution of Mechanical Engineers **141**(1): 289-338.

Landreth, C. C. and R. J. Adrian (1990). "Impingement of a low Reynolds number turbulent circular jet onto a flat plate at normal incidence." Experiments in Fluids **9**(1-2): 74-84.

Laramee, R. S., D. Weiskopf, J. Schneider and H. Hauser (2004). Investigating swirl and tumble flow with a comparison of visualization techniques. Visualization, 2004. IEEE.

Launder, B. E. and W. Rodi (1979). "The turbulent wall jet." Progress in Aerospace Sciences **19**(0): 81-128.

Launder, B. E. and D. Spalding (1974). "The numerical computation of turbulent flows." Computer methods in applied mechanics and engineering **3**(2): 269-289.

Lawton, B. (1987). "Effect of compression and expansion on instantaneous heat transfer in reciprocating internal combustion engines." Proceedings of the Institution of Mechanical Engineers, Part A: Journal of Power and Energy **201**(3): 175-186.

LeFeuvre, P. S. Myers and O. A. Uyehara (1970). "Experimental instantaneous heat fluxes in a Diesel engine and their correlations." SAE-Paper 690464.

Liou, T.-m., M. Hall, D. Santavicca and F. Bracco (1984). "Laser doppler velocimetry measurements in valved and ported engines." Training **2014**: 04-07.

Lucht, D. Dunn-Rankin, T. Walter, T. Dreier and S. C. Bopp (1991). "Heat Transfer in Engines: Comparison of CARS Thermal Boundary Layer Measurements and Heat Flux Measurements." SAE Paper 910722.

Lucht, R. P. and M. A. Maris (1987). "CARS measurements of temperature profiles near a wall in an internal combustion engine." SAE paper 870459: Medium: X; Size: Pages: 7.

Lyford-Pike, E. J. and J. B. Heywood (1984). "Thermal boundary layer thickness in the cylinder of a spark-ignition engine." International Journal of Heat and Mass Transfer **27**(10): 1873-1878.

Ma, P. C., M. Greene, V. Sick and M. Ihme (2016). "Non-equilibrium wall-modeling for internal combustion engine simulations with wall heat transfer." Accepted to International Journal of Engine Research.

MacDonald, J., M. L. Greene, D. L. Reuss, V. Sick and C. Fajardo-Hansford (2017). Two-Point Spatial Velocity Correlations in the Near-Wall Region of a Reciprocating Internal Combustion Engine. submitted to SAE 2017 World Congress and Exhibition, Detroit, MI.

Maurel, S. and C. Solliec (2001). "A turbulent plane jet impinging nearby and far from a flat plate." Experiments in Fluids **31**(6): 687-696.

McAulay, K., T. Wu, S. Chen, G. Borman, P. S. Myers and O. A. Uyehara (1965). "Development and evaluation of the simulation of the compression-ignition engine." SAE Paper 650451.

Neal, D. R., A. Sciacchitano, B. L. Smith and F. Scarano (2015). "Collaborative framework for piv uncertainty quantification: the experimental database." Meas Sci Technol **26**: 074003.

Nijeweme, D. O., J. Kok, C. Stone and L. Wyszynski (2001). "Unsteady in-cylinder heat transfer in a spark ignition engine: experiments and modelling." Proceedings of the Institution of Mechanical Engineers, Part D: Journal of Automobile Engineering **215**(6): 747-760.

Oguri, T. (1960). "On the coefficient of heat transfer between gases and cylinder walls of the spark-ignition engine." Bulletin of JSME **3**(11): 363-369.

Overbye, V., J. Bennethum, O. Uyehara and P. Myers (1961). "Unsteady heat transfer in engines." SAE Trans **69**(461).

Pflaum, W. (1961). "Wärmeübergang bei Dieselmaschinen mit und ohne Aufladung." M.T.Z. **22**: 70.

Pierce, P. H., J. B. Ghandhi and J. K. Martin (1992). "Near-Wall Velocity Characteristics in Valved and Ported Motored Engines." SAE Paper 920152.

Pope, S. B. (2000). Turbulent flows, Cambridge university press.

Poulos, S. G. and J. B. Heywood (1983). "The effect of chamber geometry on spark-ignition engine combustion." SAE Paper 830334.

Puzinauskas, P. and C. Borgnakke (1991). "Evaluation and improvement of an unsteady heat transfer model for spark ignition engines." Training **2013**: 12-05.

Raffel, M., C. E. Willert and J. Kompenhans (1998). "Particle Image Velocimetry: a practical guide." Experimental Fluid Mechanics: 253.

Rakopoulos, C., G. Kosmadakis and E. Pariotis (2010). "Critical evaluation of current heat transfer models used in CFD in-cylinder engine simulations and establishment of a comprehensive wall-function formulation." Applied Energy **87**(5): 1612-1630.

Rask, R. B. (1979). "Laser Doppler anemometer measurements in an internal combustion engine." SAE Paper 790094.

Reeves, M. (1995). Particle image velocimetry applied to internal combustion engine in-cylinder flows. Doctor of Philosophy, Loughborough University of Technology.

Reuss, D. L. (2000). "Cyclic Variability of Large-Scale Turbulent Structures in Directed and Undirected IC Engine Flows." SAE Paper 2000-01-0246.

Reuss, D. L., R. J. Adrian, C. C. Landreth, D. T. French and T. D. Fansler (1989). "Instantaneous Planar Measurements of Velocity and Large-Scale Vorticity and Strain Rate in an Engine Using Particle-Image Velocimetry." SAE Paper 890616.

Robinson, S. K. (1991). "Coherent Motions in the Turbulent Boundary Layer." Annual Review in Fluid Mechanics **23**(1): 601-639.

Rohlfs, W., H. D. Haustein, O. Garbrecht and R. Kneer (2012). "Insights into the local heat transfer of a submerged impinging jet: Influence of local flow acceleration and vortex-wall interaction." International Journal of Heat and Mass Transfer **55**(25–26): 7728-7736.

Sakakibara, J., K. Hishida and M. Maeda (1997). "Vortex structure and heat transfer in the stagnation region of an impinging plane jet (simultaneous measurements of velocity and temperature fields by digital particle image velocimetry and laser-induced fluorescence)." International Journal of Heat and Mass Transfer **40**(13): 3163-3176.

Schiffmann, P., S. Gupta, D. Reuss, V. Sick, X. Yang and T.-W. Kuo (2016). "TCC-III Engine Benchmark for Large-Eddy Simulation of IC Engine Flows." Oil & Gas Science and Technology **71**(1).

Schmitt, M. (2014). Direct Numerical Simulations in Engine-like Geometries. Doctor of Science, ETH Zurich.

Schmitt, M., C. E. Frouzakis, Y. M. Wright, A. Tomboulides and K. Boulouchos (2016). "Direct numerical simulation of the compression stroke under engine relevant conditions: Local wall heat flux distribution." International Journal of Heat and Mass Transfer **92**: 718-731.

Schmitt, M., C. E. Frouzakis, Y. M. Wright, A. G. Tomboulides and K. Boulouchos (2015). "Direct numerical simulation of the compression stroke under engine-relevant conditions: Evolution of the velocity and thermal boundary layers." International Journal of Heat and Mass Transfer **91**: 948-960.

Schmitt, M., C. E. Frouzakis, Y. M. Wright, A. G. Tomboulides and K. Boulouchos (2015). "Investigation of wall heat transfer and thermal stratification under engine-relevant conditions using DNS." International Journal of Engine Research **17**(1): 63-75.

Sciacchitano, A., D. R. Neal, B. L. Smith, S. O. Warner, P. P. Vlachos, B. Wieneke and F. Scarano (2015). "Collaborative framework for PIV uncertainty quantification: comparative assessment of methods." Measurement Science and Technology **26**(7): 074004.

Soyhan, H., H. Yasar, H. Walmsley, B. Head, G. Kalghatgi and C. Sorusbay (2009). "Evaluation of heat transfer correlations for HCCI engine modeling." Applied Thermal Engineering **29**(2): 541-549.

Steeper, R. R. and E. J. Stevens (2000). Characterization of combustion, piston temperatures, fuel sprays, and fuel-air mixing in a DISI optical engine, SAE Technical Paper.

Stitou, A. and M. Riethmuller (2001). "Extension of PIV to super resolution using PTV." Measurement Science and Technology **12**(9): 1398.

Sutera, S. P. (1965). "Vorticity amplification in stagnation-point flow and its effect on heat transfer." Journal of Fluid Mechanics **21**(03): 513-534.

Sutera, S. P., P. F. Maeder and J. Kestin (1963). "On the sensitivity of heat transfer in the stagnation-point boundary layer to free-stream vorticity." Journal of Fluid Mechanics **16**(04): 497-520.

Suzuki, T., Y. Oguri and M. Yoshida (2000). Heat Transfer in the Internal Combustion Engines, SAE International.

Taylor, C. (1951). "Heat Transmission in Internal-Combustion Engines." Proc., General Discussion on Heat Transfer, Inst. Mech. Engrs., London: 397.

Taylor, C. F. and T. Y. Toong (1957). "Heat transfer in Internal combustion engines." ASME paper 57-HT-17.

Torregrosa, A. J., P. C. Olmeda and C. A. Romero (2008). "Revising engine heat transfer." Journal of Engineering Annals of Faculty of Engineering Hunedoara **6**(3): 245-265.

Tsubokura, M., T. Kobayashi, N. Taniguchi and W. P. Jones (2003). "A numerical study on the eddy structures of impinging jets excited at the inlet." International Journal of Heat and Fluid Flow **24**(4): 500-511.

Westerweel, J. (1997). "Fundamentals of digital particle image velocimetry." Measurement Science and Technology **8**(12): 1379.

Westerweel, J., G. E. Elsinga and R. J. Adrian (2013). "Particle image velocimetry for complex and turbulent flows." Annual Review of Fluid Mechanics **45**: 409-436.

White, F. M. (2006). Viscous fluid flow. New York, McGraw-Hill.

Whitehouse, N., A. Stotter, G. Goudie and B. Prentice (1962). "Method of predicting some aspects of performance of a diesel engine using a digital computer." Proceedings of the Institution of Mechanical Engineers **176**(1): 195-217.

Whitehouse, N. D. (1970). "Heat Transfer in Compression-Ignition Engines: First Paper: Heat Transfer in a Quiescent Chamber Diesel Engine." Proceedings of the Institution of Mechanical Engineers **185**(1): 963-975.

Wieneke, B. (2015). "PIV uncertainty quantification from correlation statistics." Measurement Science and Technology **26**(7): 074002.

Williams, T. (1960). "Some applications of DEUCE to Diesel Engine Design." The Engineer **27**: 60.

Wilson, B. M. and B. L. Smith (2013). "Taylor-series and Monte-Carlo-method uncertainty estimation of the width of a probability distribution based on varying bias and random error." Measurement Science and Technology **24**(3): 035301.

Witze, P. and T. Baritaud (1985). Influence of combustion on laser Doppler velocimeter signal quality in a spark ignition engine. 2nd International Symposium on Laser Anemometry.

Witze, P. O. (1977). "Measurements of the spatial distribution and engine speed dependence of turbulent air motion in an ic engine."

Woschni, G. (1967). "A universally applicable equation for the instantaneous heat transfer coefficient in the internal combustion engine." Significance **2012**: 12-11.

Woschni, G. J. (1970). "Die Berechnung der Wandverluste und der Thermischen Belastung der Bauteile von Dieselmotoren." Motortechnishe Zeitschrift **30**(12): 491-499.

Yang, J., P. Pierce, J. K. Martin and D. E. Foster (1988). Heat transfer predictions and experiments in a motored engine, SAE Technical Paper.

Zhou, J., R. Adrian, S. Balachandar and T. Kendall (1999). "Mechanisms for generating coherent packets of hairpin vortices in channel flow." Journal of Fluid Mechanics **387**: 353-396.

Zhou, J., R. J. Adrian and S. Balachandar (1996). "Autogeneration of near-wall vortical structures in channel flow." Physics of Fluids (1994-present) **8**(1): 288-290.

Zipkin, M. A. and J. Sanders (1945). Correlation of Exhaust-Valve Temperatures with Engine Operating Conditions and Valve Design, DTIC Document.